ROBINSON 4473

TP.1072

CONNECTIVITY, FLOW AND TRANSPORT IN NETWORK MODELS OF FRACTURED MEDIA

Peter Clive Robinson

St. Catherine's College

Thesis submitted for the Degree of Doctor of Philosophy at Oxford University

Trinity Term, 1984

ABSTRACT

In order to evaluate the safety of radioactive waste disposal underground it is important to understand the way in which radioactive material is transported through the rock to the surface. If the rock is fractured the usual models may not be applicable.

In this work we look at three aspects of fracture networks: connectivity, flow and transport. These are studied numerically by generating fracture networks in a computer and modelling the processes which occur.

Connectivity relates to percolation theory, and critical densities for fracture systems are found in two and three dimensions.

The permeability of two-dimensional networks is studied. The way that permeability depends on fracture density, network size and spread of fracture length can be predicted using a cut lattice model.

Transport through the fracture network by convection through the fractures and mixing at the intersections is studied. The Fickian dispersion equation does not describe the resulting hydrodynamic dispersion.

Extensions to the techniques to three dimensions and to include other processes are discussed.

Theoretical Physics Division,
A.E.R.E. Harwell

October 1984

HL.84.3978

73 245.

9311040372 931101
PDR WASTE
WM-11 PDR

Acknowledgment

I would like to thank my supervisor, Dr. John Rae, for his advice and encouragement and for making sure that funding for this work was available.

Dr. Stinchcombe and Professor Elliott also provided useful guidance, especially in the work on connectivity.

Also thank-you to the rest of my colleagues in Theoretical Physics Division, Harwell for helpful suggestions and ideas.

The United Kingdom Atomic Energy Authority provided financial support by paying my fees as well as giving me the time and the opportunity to undertake the work. Funding was provided by the Department of the Environment, the European Economic Community and NIREX.

I would also like to thank my wife for helping with the proof-reading of this thesis and for putting up with me while I was working on it.

This thesis was typeset using the TSSD typesetting system driving a Linotron 202 at AERE Harwell.

Contents

Abstract
Acknowledgment
1. Introduction 1.1
2. Statistical Fracture Networks 2.1
3. Connectivity 3.1
   3.1 Introduction 3.1
   3.2 Relation to percolation theory 3.1
   3.3 The calculation of critical densities 3.2
   3.4 Computational technique 3.3
   3.5 Number of intersections 3.7
   3.6 Estimation of critical densities 3.10
   3.7 Relationships between critical densities 3.13
   3.8 Results of numerical experiments 3.14
   3.9 Summary and conclusions 3.22
4. Flow 4.1
   4.1 Introduction 4.1
   4.2 The physical problem 4.2
   4.3 Computational technique 4.3
   4.4 Theoretical estimates of permeability 4.6
   4.5 Results of numerical experiments 4.13
   4.6 Summary and conclusions 4.20
5. Contaminant Transport 5.1
   5.1 Introduction 5.1
   5.2 The diffusion equation approximation 5.2
   5.3 Transverse dispersion 5.6
6. Mass-Lumping Algorithm 6.1
   6.1 Introduction 6.1
   6.2 Computational details 6.3
   6.3 Results 6.4
7. Particle Following Algorithm 7.1
   7.1 Introduction 7.1
   7.2 Verification 7.2
   7.3 Results 7.3
8. Theories of Dispersion 8.1
   8.1 Introduction 8.2
   8.2 A simple random walk model 8.3
   8.3 Random direction models 8.6
   8.4 Cut lattice model 8.14
9. An Example of a Full Network 9.1
10. Network Models in Three Dimensions 10.1
   10.1 Introduction 10.1
   10.2 Pressure formulation 10.2
   10.3 Flux formulation 10.5
   10.4 An example of a fracture matrix 10.5
11. Including Other Transport Phenomena 11.1
   11.1 Transport phenomena in networks 11.1
   11.2 Extension of current models 11.4
   11.3 Modelling network transport using Laplace transforms 11.5
12. Summary and Conclusions 12.1
References
Figures

Chapter 1 Introduction

Radioactive waste arises from a number of sources. These include the reprocessing of fuel from nuclear power stations, equipment used to handle radioactive materials, contaminated clothing, medical equipment, etc. If reprocessing is not done, it may also include unreprocessed fuel elements.

This waste must be dealt with in a safe and reliable fashion. Because some of the radioactive constituents of the waste are long-lived the disposal option chosen should ensure long term isolation of the waste. Many options have been put forward. These range from exotic schemes such as disposal in outer space or at a subduction zone between tectonic plates to more practical schemes such as disposal into or under the sea or burial on land (Koplik et al.1982). In the United Kingdom the main focus of attention has been burial on land although some very low-level waste has been dumped at sea.

Radioactive waste is categorised according to its activity, and the disposal option chosen will vary from category to category.

High-level waste (HLW) is that which contains short-lived radioactive material. It arises from the reprocessing of fuel elements if this is done, or consists of the unreprocessed spent fuel elements themselves. In the U.K. above ground storage is used for the small amount of HLW produced. HLW emits large amounts of heat for the first 50–100 years, after this it can be dealt with more permanently. Once the short lived material has decayed the waste contains much longer lived materials, some with half-lives of over a million years, and so the final disposal must involve long term isolation.

Intermediate level waste (ILW) arises from reprocessing. The main difference between ILW and HLW is in the initial heat emitting stage. ILW emits only small amounts of heat and much earlier disposal is envisaged. For ILW and HLW long term isolation is required and so burial deep underground is indicated.

The final category is low level waste. This consists of slightly contaminated clothing and other materials which have come into contact with radioactive materials. It has low activity for its volume and can be buried in shallow sites on land or at sea.

Whatever the type of waste we must ensure that the chosen disposal option is safe. At a technical level this involves modelling the repository and its surroundings from the time of disposal

far into the future. One important component of any such model is the groundwater flow, which may carry radionuclides from the repository back to the surface and hence back to Man.

The type of rock in the vicinity of a repository has not yet been decided, so we must be able to model the groundwater flow and transport of radionuclides through any rock type. This work looks at the problems that arise if we must model groundwater flow and transport through fractured rocks.

Historically the modelling of groundwater flow has been based on the Darcy Law (Darcy, 1856). This treats the rock as a continuum, taking the average flow rate in some representative elementary volume (REV). The REV must necessarily be larger than the length scale of the pores through which water flows. In small grained rock this presents no problems because the scale on which information on flow rates is needed is many orders of magnitude larger than the scale on which the flow occurs. In fractured rock however it is far from clear that Darcy's Law can be used, because the fracture spacing can be of the order of metres.

The main advantage of using continuum models is that they can be solved fairly straightforwardly. For constant permeabilities and simple boundaries analytic solutions can be found, while for more complex problems numerical methods can be used. The finite element method is well suited to this type of problem. The author has developed finite element codes for flow and transport. The computer program NAMMU was written to solve the coupled heat and groundwater flow equations (Rae and Robinson,1979, Rae et al,1981,1983, Wickens,1981, Wickens and Robinson,1984). It has also been used to calculate the flow of groundwater in three-dimensional problems (Atkinson et al, 1984). Figure 1.1 shows the grid used for one of these three-dimensional problems. A related program, NAMSOL (Dolman and Robinson, 1983) was written to solve transport equations for contaminant in groundwater flow. The contaminant can be convected, dispersed and sorbed, and can decay radioactively. Decay chains can be handled. The dispersion term in this program is intended to model hydrodynamic dispersion. For fractured rock the size of this coefficient is not well known and some best estimate must be used. It is hoped that the work reported here may shed a little light on the validity of the continuum model and on the value of the dispersion coefficient.

Even if Darcy's Law is valid as far as average flow rates are concerned the fracture geometry is crucial to the particle transport. Particles travel with the local flow, not with the averaged Darcy flow. They will be dispersed by the different paths that they take. Moreover phenomena such as sorption and diffusion into the rock matrix clearly depend on the rock structure.

The aim of this work was to gain more information on the way in which the fractured nature of the rock might affect the modelling of the system. Results from models which keep the essential fractured nature of the rock are compared with the results from the usual continuum models.

The approach that has been used is to develop computer models of fracture systems and to perform experiments on these systems, to see how they can best be modelled. At the same time theoretical prediction of the experimental results have been made, to help gain some insight into the behaviour of fracture systems.

The study can be split into three areas. The first of these is connectivity, that is, do the fractures interconnect sufficiently to form large scale paths? This question is related to percolation problems in solid state physics.

The second area is bulk flow, that is the average flow of Darcy's Law. We look at the validity of the continuum approximation, and the relationship between the statistical properties of a fracture system and its permeability.

The final area is contaminant transport. How do dissolved or suspended particles move through the fracture system? Can their spread be adequately modelled by a diffusion-like law?

A real fractured rock consists of fractures of various sizes intersecting one another in a complicated three dimensional network. Each fracture has variable aperture, may or may not be planar, may be filled with minerals etc. Modelling such a system fully is clearly impossible.

The continuum approach ignores the fractures completely, reducing the system to a number of parameters, permeability, porosity, retardation coefficient, dispersion coefficient and so on. These parameters are assumed to be experimentally measurable. This approach is not adequate by itself. The continuum model must be consistent with the fundamental processes which occur at the fracture level. The equations and parameters used in the continuum model must have their basis in the fracture system. The parameters may not be measurable in practice, either because it would be too expensive, or take too long, or because it would destroy the rock being investigated. An understanding of the physics at the fracture level may suggest small scale experiments from which the parameters can be deduced.

In the end we would wish to use a continuum model, because of its computational simplicity, but we must be sure that it is appropriate, and that the parameters used are sensible. To do this we must look at the fracture level.

The data available about fracture systems is very limited. This does not prevent us from studying idealised fracture systems. This is what we have done here. As data becomes available it may be possible to use more realistic fracture systems. In this work we are more concerned with the type of model that should be used than with making actual predictions. If a continuum model can describe the behaviour of an idealised fracture system it must be a good candidate for modelling a real system. If, on the other hand, it cannot model the idealised system there is little hope of it modelling the real one.

We have studied idealised fracture systems in two ways. A computer program has been developed to look at connectivity, flow and transport in fracture systems and some simple analytical models have been used to predict the results of this program. Most of the work reported here is for two dimensional systems, although connectivity has been looked at in three dimensions. The extension of other techniques to three dimensions is discussed.

The layout of this report is as follows. After this introductory chapter, chapter 2 describes the generation of the idealised fracture systems used throughout.

Chapter 3 describes the work on connectivity, how it relates to percolation theory, how the computer program works and the results it produced. Some theoretical predictions are made and checked against the program.

Chapter 4 looks at bulk flow, the assumptions made, the computational details and the results. Some of the results are compared with theoretical predictions made using a cut lattice model.

Chapter 5 discusses some general aspects of contaminant transport, while chapters 6 and 7 describe two different computational techniques for modelling it, and the results obtained. Chapter 8 describes some theoretical approaches to transport and compares these with the results from the computer runs.

In chapter 9 we use a more general fracture system and look at contaminant transport in it.

Chapter 10 presents some ideas on extending the techniques to three dimensions, and chapter 11 looks at how other transport mechanisms could be included.

Finally chapter 12 presents a summary and conclusions.

Chapter 2 Statistical Fracture Networks

In a real fracture system each of the fractures can be described by a list of properties. These include the size, shape, position, orientation in space, aperture, etc. Over all the fractures in a region these parameters have some sort of distribution. In order to generate an idealised, but fairly realistic, fracture system we specify the distributions and generate realisations from these. In a real system there may be correlations between some of the properties. One way in which this occurs is through fracture sets. Typically fractures in a single set have similar orientations, and were probably formed in a single geological event. The properties of one set may differ from those of another set. We allow the distributions to be given in terms of fracture sets. Within a set there may well be further correlations, between size and aperture for example. In our idealisation these cannot be included explicitly, however the idealised sets can be smaller than the real sets which allows the correlations to be included. For this reason it is useful to extend the definition of a fracture set and define it to be a collection of fractures whose properties come from a single set of probability distribution functions. The properties which we currently use to define the fractures and which can vary are orientation, length and aperture. This list could be extended to include other properties (e.g. roughness or sorption characteristics) should this become necessary.

All the properties can be given distribution functions of the following types defined by two parameters μ and s

constant value	– all fractures have value μ
uniform distribution	– values anywhere between $\mu-s$ and $\mu+s$
normal distribution	– mean μ, standard deviation s
log normal distribution	– logarithm has normal distribution with mean μ standard deviation s
negative exponential	– mean μ, standard deviation s, cutoff at $\mu-s$

Other distributions could easily be included.

The fracture density for each set is specified, as the number of fracture centres per unit area. Because fractures whose centres lie outside the region of interest may enter it, care must be taken to generate fractures in a larger region. This must be chosen so that it contains the centre of any fracture which enters the region of interest. If the length distribution function has an infinite tail then the region must be chosen so as to make it unlikely that any fractures are missed. For most of the work reported here the fracture centres are uniformly distributed but the capability to have a

non-uniform distribution exists. This is specified in terms of a mapping from the unit square to any region of space. Fracture centres are generated uniformly in the unit square, the mapping then produces the non-uniform distribution.

From one set of statistics we can generate any number of networks. Each realisation of the statistics is generated as follows. A region is specified in which all the centres are to lie (either explicitly or in terms of the mapping). Inside this a solution region is placed. Only fractures which enter this solution region are of interest and any others are not recorded. For each realisation a random number seed is set, so that the realisation can be regenerated if required. The actual random number generator used depends on the computer being used. On the CRAY-1S, where most of the work was done, the RANF library routine was used for uniform random numbers. Normally distributed random numbers were obtained by summing twelve of these uniform numbers. On the IBM3081 we used the Harwell Subroutine Library routines FA04AS and FA05A.

Fracture generation proceeds as follows. The total number of fractures to be generated is calculated from the sum of the fracture set densities. Fractures are then generated one by one. For each fracture the set to which it belongs is decided first. This is done, rather than generating fractures set by set, for two reasons. Firstly, when we are looking for paths across regions the order of the fractures must be random and, secondly, the actual number in each set will vary slightly, as it would in a real system. Once the set is decided the centre position is found. The length and orientation are calculated and saved as a displacement from the centre to one end. Finally the fracture aperture is found. If the fracture enters the solution region it is added to the list of fractures, otherwise it is discarded. In this way the list of fractures for the rest of the calculation is generated.

This generation of the fracture system can be bypassed if, for example, a specified fracture network is to be used. This method has been used to compare results with Schwartz's program, see chapter 7. It was also used at an early stage to set up simple test cases to help debug the program.

The collection and analysis of the data, that would be required to apply the techniques used here to real fracture systems, is beginning. For the purposes of this work a lack of data is not important since we are at the stage of developing an general understanding of the processes that are important in fractured rock. However this data will become important if we are to look at specific real systems. A study of Cornish granite (Heath,1983, Bourke et al,1981,1982,1984, Heath and

Durrance.1984) has produced a iarge amount of data which is beginning to be analysed (Hodgkinson.1984) . This data includes fracture orientations from core logs. the results of pumping tests and tracer tests. From this information a picture of a real fracture system is beginning to emerge. Work has also been undertaken in Sweden (KBS.1983) and Scotland (McEwen and Lintern.1980).

Chapter 3 Connectivity

3.1 Introduction

In order that water can flow through a fractured rock mass the fractures must be sufficiently interconnected to form large-scale paths. The existence of such flow paths depends on the geometry of the particular fracture system in question. For a given set of fracture statistics some realisations will exhibit large-scale paths while others show only local connectivity. Clearly as the number of fractures in a given piece of rock increases the chance of large-scale paths gets greater. The purpose of the work described in this chapter was to quantify this increased probability and to find how it depends on the statistics of the fracture system.

3.2 Relation to percolation theory

The problem tackled here is related to percolation problems in solid state physics (Essam, 1980), in fact it is closer to the initial work (Broadbent and Hammersley, 1957) than to the current areas of interest in solid state physics.

In a general percolation theory system we start with an infinite set of sites. Certain pairs of sites are connected by bonds. Two types of percolation model are discussed, site percolation and bond percolation. Site percolation involves a probability $p^{(S)}$ that any site is open, independently of other sites. Paths are then sequences of connected open sites. In bond percolation all the sites are open but there is a probability $p^{(B)}$ that each bond is unblocked, again independently of all other bonds. In this case a path is a sequence of open sites connected by unblocked bonds. In either case a cluster is a set of sites in which any pair is connected by a path. It is found that a critical probability exists in each case. For the site percolation case if $p^{(S)} < p_c^{(S)}$ only finite size clusters exist, but for $p^{(S)} > p_c^{(S)}$ infinite clusters appear. For bond percolation the position is the same, if $p^{(B)} < p_c^{(B)}$ there are only finite size clusters while for $p^{(B)} > p_c^{(B)}$ there are infinite clusters. Generally the systems considered are lattices with bonds connecting neighbouring sites.

Our case is in some sense a continuum limit of the site percolation model. Our sites are the fractures which can be in any position with any length and orientation. Two fractures have a bond between them if they intersect. The probability of a site being open has become the density of

fractures (i.e. the number of fractures per unit area, or volume in three dimensions). A cluster is a set of connected fractures.

Notice that it is more natural to make the association in this way than to associate fracture intersections with sites and fractures with bonds. This is because this latter association gives a correlated percolation model, since two sites being connected implies a fracture which increases the probability of further connections along this fracture. By associating fractures with sites the independence is retained.

Having made this association we are led to expect that there is a critical fracture density above which paths will exist and below which the fractures will only be locally connected. The numerical calculations will show that this is indeed the case.

3.3 The calculation of critical densities

The critical density for an infinite fracture system is that density above which infinite clusters of fractures appear. This definition is of no direct use when the critical density is to be determined numerically. We must have a different definition for finite systems which becomes equivalent to the infinite system definition as the region size increases.

There is no unique way of defining the finite size critical density. The definition we have used in most cases is the following. We take a fixed size square region and generate fractures in and around it until a cluster which makes contact with all the sides has been formed. At this point we say that this system is percolating and record the number of fractures centred in the region. This is done for many realisations of the same statistics and the average density of fractures at percolation is taken to be the critical density. This is equivalent to taking an infinite fracture system and placing a square region randomly on it. We would then take the critical density to be the density at which half the squares had a cluster joining all four sides. In three dimensions the extension is the obvious one of a cube with a cluster connecting all six faces. A typical percolating fracture system is shown in figure 3.1. The percolating cluster from this system is shown in figure 3.2.

One alternative definition is to require the cluster to connect either pair of opposite sides of the square, or any pair of opposite faces in three dimensions. We have made a series of runs using this

alternative definition and compared them with our usual definition. Except for small regions the difference is not very large, although the variation with region size is interesting. These results are described in §3.8.

Another possible definition would involve forming a periodic network with the square region as the basic cell. The intersections for such a system could easily be found but finding the infinite clusters would be computationally quite difficult and so the definition has not been tried here.

3.4 Computational technique

The computational technique used to find critical densities can be outlined as follows. For clarity this description concentrates on the two dimensional problem. The three dimensional case is in most respects the same.

For a given set of statistical distributions of fracture parameters we generate fractures one by one in the vicinity of a square region (so that any fracture which enters the region could be chosen). As the fractures are generated we keep track of all clusters into which they form. Each new fracture that is generated can do one of three things. It can form a new cluster, extend an existing cluster or unite two or more existing clusters. Any cluster which has been altered can then be checked to see if it reaches all four sides. Once a cluster does reach all four sides fracture generation is stopped and the density of fractures (i.e $\frac{\textit{number of fractures centered in region}}{\textit{area of region}}$) is recorded.

In order to find whether each new fracture intersects nought, one or more existing clusters we must find all the previously generated fractures which it intersects. Given a pair of fractures it is a simple matter to determine whether they intersect. However for large fracture systems we cannot check all possible pairs since this would be prohibitively expensive. In order to reduce the number of checks needed to manageable proportions a special algorithm has been devised.

We start by covering the region with a regular grid. The number of grid blocks in each direction is an adjustable parameter which can be used to optimise the algorithm. The grid box corresponding to any point in the region can be found very quickly by dividing the coordinates by the box size. Now as the fractures are generated a list of all the fractures which pass through each grid block is maintained. This is done as follows.

Each new fracture is split into 'sublines', with one subline for each box through which the fracture passes. If the fracture cuts diagonally across the boxes it can be time consuming to find which boxes it actually goes through. In such cases it is better to include all *possible* boxes. For example if one end of a fracture is in box (IX, IY) and the other is in box (IX+1, IY+1) we would include boxes (IX+1, IY) and (IX, IY+1). Now we create one new subline for each box in the list. For each subline we record the original fracture number and for each box crossed we update a linked-list structure which records which sublines belong to each box. Two arrays are used, the two-dimensional array IBXST records the last subline for each box and the one-dimensional array NEXT records the previous subline in the same box as this subline. So to get a full list of all sublines for box (IX, IY) we set ISUBL=IBXST(IX, IY) to get the first and then set ISUBL=NEXT(ISUBL) repeatedly to get all the others, terminating when a zero is reached. In order to add a new subline, NEWSL, to the list we just have to set NEXT(NEWSL)=IBXST(IX, IY) and IBXST(IX, IY)=NEWSL.

Now we need only check each new fracture for intersections with fractures which have sublines in the same grid boxes. To see how much this saves consider an example. With N fractures in a region R by R we would need to check $\frac{1}{2}N(N-1)$ pairs of fractures if all possible pairs were taken. If we split the region into boxes of size h by h so that an average fracture passes through k boxes the number of checks becomes $\frac{N^2h^2k^2}{R^2}$ giving a reduction by a factor $\frac{h^2k^2}{R^2}$. In practice the cost of setting up and maintaining all the box information begins to dominate if too many boxes are used. We have found that choosing the box size so that each fracture passes through two or three boxes gives the best results.

In some special cases we can do even better, in particular in the case of two orthogonal fracture sets we can use the fact that two fractures in the same set cannot intersect. This we have done by keeping separate lists of horizontal sublines in boxes and of vertical sublines in boxes.

Having found all the intersections the cluster information can be updated. If the new fracture has no intersections it forms a new cluster. If it intersects with fractures from a single existing cluster it is added to that cluster. If it intersects with fractures from more than one existing cluster these clusters are all united to form a single larger cluster. This is done by recording the new cluster number against the initial cluster number. The cluster for each fracture is not updated, so that to find which cluster a fracture is currently in it is necessary to loop round starting with the

initial cluster and going to the cluster which this became until the current cluster is found. This is identified by the new cluster number equalling the old cluster number.

In order to check for percolation the sides which each cluster touches are recorded. As new fractures are added and clusters unite this is updated until one cluster reaches all the sides. This is then the percolating cluster and fracture generation stops for this realisation.

It can be seen that this algorithm can easily be modified to deal with other definitions of percolation, for example if a connection between two opposite sides was deemed sufficient. It could also easily handle the percolation of shapes other than straight line fractures. It forms the basis of the method used in later work on flow where the density is fixed and it is required to find all the intersections.

In the three dimensional case with fractures represented as rectangles with any size, position and orientation it is not trivial to find whether two arbitrary fractures intersect. The method used is described below.

In three dimensions the positions and orientations of the fractures are kept internally as the centre **c**, and the displacements to the mid-sides **r** and **s**. The corners of the fractures are thus at $\mathbf{c}\pm\mathbf{r}\pm\mathbf{s}$. Once a pair of fractures has been identified as possibly intersecting the following procedure is used to determine whether they do intersect. The notation used is illustrated in figure 3.3.

We have two fractures defined by $\mathbf{c}_1,\mathbf{r}_1,\mathbf{s}_1$ and $\mathbf{c}_2,\mathbf{r}_2,\mathbf{s}_2$.

The normals to the planes are

$$\mathbf{n}_1 = \mathbf{r}_1\times\mathbf{s}_1 \qquad \text{and} \qquad \mathbf{n}_2 = \mathbf{r}_2\times\mathbf{s}_2. \tag{3.1}$$

The line of intersection of two planes with these normals has direction

$$\mathbf{t} = \mathbf{n}_1\times\mathbf{n}_2. \tag{3.2}$$

One point on this line is at the end of a perpendicular from the origin and therefore has position

$$\mathbf{p} = \alpha\mathbf{n}_1+\beta\mathbf{n}_2. \tag{3.3}$$

Now **p** is in both fracture planes so

$$(\mathbf{p}-\mathbf{c}_1)\cdot\mathbf{n}_1 = 0 \qquad \text{and} \qquad (\mathbf{p}-\mathbf{c}_2)\cdot\mathbf{n}_2 = 0. \tag{3.4}$$

Now using (3.3) and (3.4) we get an equation for α and β

$$\begin{pmatrix} \mathbf{n}_1\cdot\mathbf{n}_1 & \mathbf{n}_1\cdot\mathbf{n}_2 \\ \mathbf{n}_2\cdot\mathbf{n}_1 & \mathbf{n}_2\cdot\mathbf{n}_2 \end{pmatrix}\begin{pmatrix} \alpha \\ \beta \end{pmatrix} = \begin{pmatrix} \mathbf{n}_1\cdot\mathbf{c}_1 \\ \mathbf{n}_2\cdot\mathbf{c}_2 \end{pmatrix} \tag{3.5}$$

This gives α and β and hence $\mathbf{p}$. The intersecting line is then the locus of points $\mathbf{p}+\gamma\mathbf{t}$. We must now find the range of γ for the interior of each fracture. In plane 1 we write

$$\mathbf{t} = u\mathbf{r}_1 + v\mathbf{s}_1 . \tag{3.6}$$

Since $\mathbf{r}_1$ and $\mathbf{s}_1$ are orthogonal this gives

$$u = \frac{\mathbf{t}\cdot\mathbf{r}_1}{\mathbf{r}_1\cdot\mathbf{r}_1} \qquad\qquad v = \frac{\mathbf{t}\cdot\mathbf{s}_1}{\mathbf{s}_1\cdot\mathbf{s}_1} . \tag{3.7}$$

Similarly we write

$$\mathbf{p} = \mathbf{c}_1 + a\mathbf{r}_1 + b\mathbf{s}_1 \tag{3.8}$$

with

$$a = \frac{(\mathbf{p}-\mathbf{c}_1).\mathbf{r}_1}{\mathbf{r}_1\cdot\mathbf{r}_1} \qquad\qquad b = \frac{(\mathbf{p}-\mathbf{c}_1).\mathbf{s}_1}{\mathbf{s}_1\cdot\mathbf{s}_1} \tag{3.9}$$

so

$$\mathbf{p}+\gamma\mathbf{t} = \mathbf{c}_1 + (a+\gamma u)\mathbf{r}_1 + (b+\gamma v)\mathbf{s}_1 . \tag{3.10}$$

Therefore the interior of the fractures is where

$$a+\gamma u \le 1 \qquad \text{and} \qquad |b+\gamma v| \le 1 . \tag{3.11}$$

This gives four conditions on γ (two for each fracture). If all can be satisfied the fractures intersect and the range of γ over which the conditions are satisfied gives the line segment along which the fractures meet. If no γ will satisfy all the conditions then the fractures do not intersect.

It can be seen from this that in three dimensions it is even more important to avoid too many unnecessary checks for intersection.

3.5 Number of intersections

As we shall see later, the number of intersections for each fracture is an important variable. It can be calculated numerically as the algorithm proceeds. It can also be accurately predicted for any fracture statistics from simple geometrical arguments.

Note that the number of fracture intersections at percolation is the continuum equivalent of $zp_c^{(S)}$ where z is the number of bonds connected to each site in a lattice calculation. In lattice calculations it is found that as the coordination number, z, increases $zp_c^{(S)} \rightarrow 4.5$ in two dimensions and $zp_c^{(S)} \rightarrow 2.7$ in three dimensions (Shante and Kirkpatrick,1971).

In this section we show how density and average number of intersections are related in general and give the formulae for some cases. The general argument holds for any system in any number of dimensions.

The sites (fractures) in the system are described by a set of parameters s. Two sites are connected by a bond if their parameters satisfy some conditions, $b(\mathbf{s}_i,\mathbf{s}_j)=1$ say, where $b(\mathbf{s}_i,\mathbf{s}_j)=0$ if there is no bond. The parameters come from some known probability distributions, $f(\mathbf{s})$. The average number of bonds per site (intersections per fracture) is just the number of fractures times the integral over the parameter space of the function b times the probability distribution functions

$$I = N\int d\mathbf{s}_i \int d\mathbf{s}_j\, b(\mathbf{s}_i,\mathbf{s}_j)\cdot f(\mathbf{s}_i)\cdot f(\mathbf{s}_j) \tag{3.12}$$

For some of the systems we are concerned with we can also say that the actual number of intersections on a particular fracture is distributed with a Poisson distribution with mean I, so

$$P_r = \frac{e^{-I}\cdot I^r}{r!}. \tag{3.13}$$

This does not apply to cases with variation in fracture length.

Consider an example. Take the system with fractures all of fixed length $2l$ oriented either horizontally or vertically with equal probability. The density is ρ so in a region of area A there are $N=\rho A$ fractures. Any randomly chosen pair of fractures will intersect if they are orthogonal and if the centre of one lies within a square with side $2l$ around the other's centre. So, ignoring the effect of the boundaries, the probability that the two intersect is $p = \frac{1}{2}\frac{(2l)^2}{A}$. Therefore the probability that a given line intersects r other lines is

$$P_r = \frac{(N-1)(N-2)\ (N-r)}{r!}(1-p)^{N-1}p^r(1-p)^{-r}. \tag{3.14}$$

As A, and hence N, tends to infinity this gives

$$P_r = \frac{(2\rho l^2)^r}{r!}e^{-2\rho l^2}. \tag{3.15}$$

So the distribution of the number of intersections is a Poisson distribution as claimed and has mean $I=2\rho l^2$. The critical number of intersections per fracture for this case is therefore $I_c = 2\rho_c l^2$

Similar results can be derived for other fracture statistics. They are collected in the table 3.1.

Fracture Statistics	Number of Intersections per fracture
Two orthogonal sets. All with length $2l$. Half oriented each way. Total density ρ.	$2\rho l^2$
Two sets with angle α between them. All with length $2l$. Half oriented each way. Total density ρ.	$2\rho l^2 \sin\alpha$
Uniformly distributed orientation. All with length $2l$. Density ρ.	$\frac{8}{\pi}\rho l^2$
Orientation uniformly distributed between $-\alpha$ and α. All with length $2l$. Density ρ.	$\rho l^2 \cdot \frac{2}{\alpha^2}.(2\alpha - \sin 2\alpha)$
Any case with lengths uniformly distributed.	As for case with fixed length equal to average length, not a Poisson distribution

Table 3.1
Relationship between density and number of intersections.

In three dimensions we consider just two cases. The first is the equivalent of the two-dimensional example just described. The fractures are all squares with sides of length $2l$ parallel to the coordinate axes. One third of the planes are in each of the coordinate planes. The total density is ρ. Two planes will intersect if their centres are close enough together and they are not parallel. The volume in which the centre of one plane must lie has dimensions $4l \times 2l \times 2l$ and there is a factor of $\frac{2}{3}$ since the two must not be parallel. Thus the average number of intersections is $I = \frac{32}{3}\rho l^3$.

The second three-dimensional case is more difficult to calculate. In this case the fractures can have any orientation with equal probability and are again squares with sides of length $2l$. The total density is ρ.

When considering the probability that two fractures intersect we can choose our coordinate system so that one fracture is centred at the origin with its sides parallel to the x and y coordinate

axes and its normal along the z−axis. The second fracture lies in a plane which makes an angle γ with the xy−plane. The line of intersection between the planes containing the fractures cuts the x−axis at an angle α and the perpendicular distance of this line from one corner of the first plane is r. Figure 3.4 shows this notation. For fixed values of γ, α and r the area on the second plane in which the fracture centre must lie if there is to be an intersection can be calculated, this is illustrated in figure 3.5. If one side of the fracture makes an angle β with the line of intersection the area is $4l^2+2sl(\sin\beta+\cos\beta)$ if s is non-zero or zero if s is zero. Averaging over β gives $4l^2+\frac{8}{\pi}ls$.

Now we can vary r from 0 to $2l(\sin\alpha+\cos\alpha)$. Three ranges need to be considered. We have

$$\begin{array}{ll} s=r(\cot\alpha+\tan\alpha) & 0\leq r\leq 2l\sin\alpha \\ s=2l\sec\alpha & 2l\sin\alpha\leq r\leq 2l\cos\alpha \\ s=2l(\operatorname{cosec}\alpha+\sec\alpha)-r(\cot\alpha+\tan\alpha) & 2l\cos\alpha\leq r\leq 2l(\cos\alpha+\sin\alpha) \end{array} \tag{3.16}$$

Note that we can always take $\alpha\leq\frac{\pi}{4}$ by choosing the x−axis appropriately.

Using the above formulae for s we can now integrate over r to give the volume in which the second centre must lie for fixed α and γ. There is a factor of $\sin\gamma$ because of the slope of the plane. This integral gives a volume

$$8l^3(\cos\alpha+\sin\alpha+\frac{4}{\pi})\sin\gamma \tag{3.17}$$

We can now average over α which is uniformly distributed to get $\frac{64}{\pi}l^3\sin\gamma$. Finally we average over γ, picking up a weight of $\sin\gamma$ to give a final result of

$$I = 16\rho l^3. \tag{3.18}$$

3.6 Estimation of critical densities

Exact results are known for some simple two-dimensional lattice percolation problems. In particular it is known that the critical probability for bond-percolation on a square lattice is $p_c = \frac{1}{2}$. We can use this result to estimate the critical density for two sets of fractures, oriented horizontally and vertically.

We start by covering the coordinate plane with a regular square grid. The lattice bond problem is defined by sites at the centres of all the grid blocks. We allow bonds between nearest neighbouring sites. Now each fracture in our fracture system is associated with the grid block in which its centre is positioned. If there is a fracture associated with one grid block which intersects with a fracture centred in a neighbouring block we say that the bond between the corresponding sites is open. It is clear that by making this association between the lattice and the fracture network we can calculate a density of fractures at which the lattice percolates. We claim that, as long as the grid spacing is chosen sensibly, this density will be a good approximation to the critical fracture density. In choosing the grid spacing two conflicting requirements must be borne in mind. First, the spacing must not be so small that non-neighbouring grid blocks could be connected. Second, the grid blocks must not be so large as to require us to consider whether a block has connections right across it.

The smallest blocks which do not allow connection between non-nearest neighbours are of size half the fracture length. At this spacing the fractures completely cross the blocks so there should be no worry about the second point. Note here that we are not considering cross-corner connections. This is because the existence of such connections is not independent of the existence of cross-side connections, the existence of a cross-corner connection with no corresponding cross-side connections is unlikely and so is ignored.

The probability that a bond exists across an edge is calculated as follows. Two squares are connected if a fracture centred in one intersects a fracture centred in the other. Consider the case of two squares, A and B, with A to the left of B. There are two types of connection between A and B. First, we could have a horizontal line in A intersecting a vertical line in B, and second we could have a vertical line in A intersecting a horizontal line in B. We will denote the probability of the first case p_{HV} and that of the second p_{VH}. By symmetry we have $p_{HV} = p_{VH}$. There will be a connection of the first type unless

(i) there is no horizontal line in A

or (ii) there is no vertical line in B

or (iii) the rightmost horizontal line in A does not intersect the leftmost vertical line in B.

We denote the probabilities of these three as p_1, p_2 and p_3. By symmetry we have $p_1 = p_2$. Given these probabilities we can calculate p_{HV} using

$$p_{HV} = (1-p_1).(1-p_2).(1-p_3) \tag{3.19}$$

and then the probability of connection P is given by

$$P = 1-(1-p_{HV}).(1-p_{VH}). \tag{3.20}$$

For total density ρ we have an average of $\mu = \frac{1}{2}\rho l^2$ fractures oriented each way in each block, where l is the block size and $2l$ is the fracture length. The actual number is a Poisson distribution so that the probability of r fractures in one direction is

$$q_r = \frac{\mu^r}{r!}e^{-\mu} \tag{3.21}$$

This immediately gives p_1 and p_2 since both are equal to q_0, that is $e^{-\mu}$. In order to find p_3 we need to know how the maximum of r values in the interval (0,1) is distributed. It is easy to see that

$$Prob(\max_{i=1,r} X_i \leq X) = X^r \tag{3.22}$$

so the probability distribution function is

$$f_r(X) = rX^{r-1} \tag{3.23}$$

Now r has a Poisson distribution with mean μ so

$$f_{\max}(X) = \sum_{r=1}^{\infty} \frac{\mu^r}{r!}e^{-\mu}f_r(X) = \sum_{r=1}^{\infty} \frac{\mu^r}{(r-1)!}e^{-\mu}X^{r-1} = \mu e^{-\mu}e^{\mu X}. \tag{3.24}$$

Similarly

$$f_{\min}(X) = \mu e^{-\mu X}. \tag{3.25}$$

So

$$p_3 = \int_0^1 dx\, \mu e^{-\mu}e^{\mu x} \int_x^1 dy\, \mu e^{-\mu y} = \mu e^{-\mu} - e^{-\mu} + e^{-2\mu}. \tag{3.26}$$

We can now use these formulae to find μ when $P = \frac{1}{2}$. We find that μ=0.860 gives $p_1 = p_2$=0.423 and p_3=0.120 giving $p_{HV} = p_{VH}$=0.293 and $P = \frac{1}{2}$. Recall that $\mu = \frac{1}{2}\rho l^2$ and that $I_c = 2\rho_c l^2$ giving a predicted average number of intersections per fracture at percolation of 3.44.

In three dimensions the position is very similar. The two-dimensional square lattice is replaced by the three-dimensional simple cubic lattice (with six nearest neighbours). We take the case of three orthogonal fracture sets, one normal to each of the coordinate axes. The fractures are squares with sides parallel to the coordinate axes. The lattice result is approximately $p_c^{(B)} = 0.247$. Since the exact analysis is somewhat involved we have obtained the result numerically by writing the probability of connection

$$P = \sum_{r=1}^{\infty} \frac{\mu^r}{r!} e^{-\mu} \sum_{s=1}^{\infty} \frac{\mu^s}{s!} e^{-\mu} P_{rs} \tag{3.27}$$

where μ is the average number of fractures centred in a box and P_{rs} is the probability of a connection given that there are r fractures centred in one box and s in the adjacent box. P_{rs} was evaluated numerically by taking 10000 realisations for each r,s pair. The boxes were taken to be equal to the fracture size, since smaller boxes would allow connections between non-neighbouring boxes. The value of μ required to give P=0.247 was found to be 1.57 which corresponds to an average of 2.09 intersections per fracture at percolation.

This is a very low result compared with the two-dimensional prediction. If we take a cross-section through this three-dimensional system the resulting two-dimensional network would have an average of only 1.57 intersections per fracture, less than half the predicted percolation value.

3.7 Relationships between critical densities

We can predict relationships between critical densities for various fracture statistics by using some simple geometrical arguments. Most of these predictions are approximate, however the first is exact.

If we consider a percolating system with two fracture sets, one horizontal and the other oriented at an angle α to the horizontal we can show that the number of intersections at the critical density is independent of α. This is done by transforming the system to the orthogonal system by applying a shearing transformation

$$\begin{pmatrix} x \\ y \end{pmatrix} \rightarrow \begin{pmatrix} 1 & -\cot\alpha \\ 0 & \operatorname{cosec}\alpha \end{pmatrix} \begin{pmatrix} x \\ y \end{pmatrix}. \tag{3.28}$$

This preserves the intersections and the uniformity of distribution of the fracture centres. The fracture length is unchanged because of the $\operatorname{cosec}\alpha$ term on the matrix diagonal. The density is changed by a factor $\sin\alpha$, which is as it must be if the result given in §3.5 is to be satisfied. This has shown that there is a 1–1 correspondence between percolating systems in the angle α case and the orthogonal case with the systems having the same number of intersections, and so the critical average number of intersections I_c is the same for both systems. This result was also pointed out by Balberg and Binenbaum (1983).

Given the previous exact result it seems probable that I_c is approximately constant over all cases with fixed length fractures and various orientation distributions. If this is the case then the results of §3.5 relating density and intersections can be used to estimate critical densities in these cases.

If the fractures are not all the same length how does I_c vary? Consider an extreme example, with fractures that can have lengths $2l$ or $2L$ with $L \gg l$. Let the probabilities of the lengths occurring be p_l and p_L. As long as p_L is not too small it is clear that the small fractures play no part in percolation. Percolation will occur when the longer fractures are sufficiently dense. The required density will be the same as if all the fractures had length $p_L^{\frac{1}{2}} L$. This is the root mean square fracture length in the network. We postulate that this is true for more general distributions of fracture length. It is true for the case just considered and for the constant length case. It implies that I_c is not independent of length distribution but that a weighted average should be used, with the weight attached to each fracture being the length of the fracture. This would lead to a definition of weighted average number of intersections as

$$J = \frac{\sum_{\text{all fractures}} \textit{number of intersections} \times \textit{fracture length}}{\sum_{\text{all fractures}} \textit{fracture length}}. \tag{3.29}$$

For the case of a uniform distribution of lengths with lengths in the interval $(2l_{av}(1-\theta), 2l_{av}(1+\theta))$ this gives the relationship $J = (1+\frac{1}{3}\theta^2).l$, so if J_c is constant we would expect to find l_c proportional to $(1+\frac{1}{3}\theta^2)^{-1}$. The results for this case are given in §3.8.

3.8 Results of numerical experiments

Numerical experiments have been carried out to determine critical densities for a number of different statistical fracture distributions. The results have been compared with the predictions given earlier in this chapter and with some previously published results by Pike and Seager (1974) and Balberg and Binenbaum (1983).

First we look at the way calculated critical densities depend on the size of the region in which the fractures are generated.

The case considered was for two orthogonal fracture sets oriented parallel to the sides of the region. In all cases the fractures were of length 2 units, the region size ranged from 10 units to 400 units. For each region size at least 100 realisations were done, the actual number done in each case is given in table 3.2. The number of fractures in the table refers to the number generated in an extended area around the region, 1 unit larger in each direction. This area was used since fractures centred within it could enter the percolation region. The time per realisation is given and the time per realisation divided by the average number of fractures. This shows that the algorithm used takes a time which increases only linearly with the number of fractures. The sudden increase for the largest two region sizes is due to a change in algorithm to reduce the amount of computer space used so that the code would fit into the CRAY-1S at Harwell.

It can be seen that the calculated ρ_c decreases with increasing region size. We can attempt to predict the form of this decrease by using finite-size scaling arguments (Fisher,1971). The argument runs as follows. Let R be the region size, C be the correlation length (which diverges at the transition) and ρ be the density which has critical value ρ_c in the infinite case. Then C is a function of ρ and R. For ρ near ρ_c and infinite R the correlation length has the form

Region Size	Number of runs	Number of fractures Average	Number of fractures Std. Dev.	Density Average	Density Std. Dev.	Time per run (secs)	Time per run per fracture (μsecs)
10	400	233	33.9	1.616	0.2355	0.0053	22.77
20	400	775	69.5	1.600	0.1436	0.0176	22.71
30	400	1640	119.9	1.602	0.1171	0.0381	23.23
40	400	2799	168.9	1.587	0.0958	0.0658	23.51
50	500	4285	208.3	1.585	0.0770	0.101	23.57
60	100	6102	284.1	1.587	0.0739	0.144	23.60
70	100	8179	326.5	1.578	0.0630	0.194	23.72
80	100	10627	418.0	1.580	0.0622	0.254	23.90
90	100	13422	346.7	1.588	0.0410	0.319	23.77
100	200	16369	467.8	1.573	0.0450	0.391	23.87
110	100	19807	609.6	1.579	0.0486	0.477	24.08
120	100	23456	548.5	1.576	0.0369	0.563	24.00
130	100	27326	668.7	1.568	0.0384	0.654	23.93
140	100	31544	751.2	1.564	0.0373	0.754	23.90
150	100	36216	834.3	1.568	0.0361	0.877	24.17
200	200	63896	1050.5	1.566	0.0257	1.559	24.37
250	100	99468	1489.1	1.566	0.0235	2.414	24.27
300	200	142310	2010.0	1.560	0.0220	4.480	31.42
400	200	252212	2854.2	1.561	0.0177	7.952	31.51

Table 3.2
Results of region size variation run for orthogonal fracture sets.

$$C(\rho,\infty)\propto(\rho-\rho_c)^{-\nu} \tag{3.30}$$

where ν is the correlation length exponent. This is known to be $\frac{4}{3}$ for two-dimensional lattices. In a finite system criticality is reached when $\frac{R}{C(\rho,\infty)}$ is some constant, i.e. when $B(\rho-\rho_c)^{\nu}$ is constant. So

$$(\rho-\rho_c)\propto R^{-\frac{1}{\nu}}. \tag{3.31}$$

This gives a relationship

$$\rho_c(R) = \rho_c(\infty)+aR^{-\frac{1}{\nu}} \tag{3.32}$$

if the lattice value for ν is assumed. The best least squares fit to the results gives $\rho_c(\infty) = 1.556$ with a=0.505. This is shown on figure 3.6 with all the results. If the more general form

$$\rho_c(R) = \rho_c(\infty)+aR^{-\frac{1}{\nu}} \tag{3.33}$$

is used with ν allowed to vary we find $\nu = 3.23$, $\rho_c(\infty) = 1.531$ and $a = 0.184$. This is also shown in figure 3.6.

As the region size increases the standard deviation in the density at percolation goes down, it must be zero for infinite regions. In figure 3.7 we plot the logarithm of the standard deviation against the logarithm of the region size. The best fit line is shown. This gives the relationship $\sigma_c(R) = 1.3R^{-0.722}$ which gives a very good fit. The exponent in this is very close to $-\frac{3}{4}$ suggesting that the variability in the percolation density is proportional to the discrepancy between the finite and infinite critical densities, i.e. $\sigma_c(R) = 2.57(\rho_c(R)-\rho_c(\infty))$.

It is clear from the above investigation that small region sizes should be avoided, both because the calculated critical density deviates from the infinite value at small region sizes and because the variability is larger. In the calculations that follow we have tried to use region sizes which give at least ten thousand fractures at percolation. Doing large numbers of realisations for many fracture statistics would become prohibitively expensive for any much larger number. The finite-size effect must always be borne in mind when comparing percolation results, as it may be as significant as any variations caused by the statistics of the fracture distributions.

The results of this example can be compared with the predictions of §3.6. In §3.6 we predicted that the critical density would correspond to 3.44 intersections per fracture. For the largest region size used in this example we had $I_c = 3.12$ and for the limiting value, with $\nu = \frac{3}{4}$ we would get $I_c = 3.11$. Thus the predicted result is around 10% too high, possibly because of the way we ignored corner connections.

As explained in §3.3 our definition of percolation requires a cluster to cross all four sides of the region. To see how much effect using a different criterion might have we have done some runs with a requirement that either pair of opposite sides be joined. This must give a lower value for the calculated critical densities. The fracture statistics were the same as for the previous example. For convenience some of the previous results are repeated in the table 3.2 together with the new results.

It can be seen that the reduction in calculated critical density caused by changing the criterion is approximately equal to the standard deviation of the critical density. It is clear that the average between old and new densities is very nearly constant, suggesting that the two densities are tending towards this value at equal rates. The previous estimate, using the finite size scaling with $\nu = \frac{3}{4}$

Region Size	Old density Average	Old density Std. Dev.	New density Average	New density Std. Dev.	Change in density	Average density
50	1.585	0.0770	1.520	0.0707	0.065	1.5525
100	1.573	0.0450	1.529	0.0483	0.044	1.5510
150	1.568	0.0361	1.530	0.0331	0.038	1.5490
200	1.566	0.0257	1.538	0.0306	0.028	1.5520
300	1.560	0.0220	1.539	0.0215	0.021	1.5495
400	1.561	0.0177	1.546	0.0151	0.015	1.5535

Table 3.3
Comparison of original percolation criterion and two-sided criterion.

gave $\rho_c = 1.556$ which agrees very closely with this average value of 1.552. Figure 3.8 shows all these results graphically.

After these results had been collected the size of the CRAY computer was increased. This enabled larger systems to be used. For a region size of 590 units we did ten runs. The average densities for two- and four-sided percolation were 1.551 and 1.556. On average there were over 545,000 fractures, and the time taken was 17.5 seconds per run. The average critical density between the two criteria was 1.5537, in good agreement with the previous results.

We now present the results for four different fracture statistics. The first of these is for a system with fractures of constant length, two units, and with orientations uniformly distributed in the interval $(-\alpha, \alpha)$, for $\alpha = 90°, 80°, 70°, 60°, 50°, 40°, 30°$ and $20°$. The $90°$ case corresponds to the uniformly distributed orientation of Pike and Seager (1974).

Table 3.4 gives the results, the final column being from the formula derived in §3.5

α	Density ρ Average	Density ρ Std. Dev.	Intersections I Average	Intersections I Std. Dev.	Ave. I / Ave. ρ	$\frac{2}{\alpha^2}(2\alpha - \sin 2\alpha)$
90°	1.434	0.0624	3.650	0.1568	2.545	2.546
80°	1.452	0.0509	3.650	0.1331	2.514	2.514
70°	1.498	0.0410	3.615	0.1091	2.413	2.413
60°	1.612	0.0618	3.606	0.1433	2.237	2.240
50°	1.795	0.0767	3.582	0.1559	1.996	1.997
40°	2.126	0.0835	3.590	0.1481	1.689	1.688
30°	2.728	0.1301	3.607	0.1700	1.322	1.322
20°	4.002	0.1495	3.639	0.1417	0.909	0.908

Table 3.4
Results for uniform distribution of orientations.

The region size was 80 by 80 so that there were more than 9000 fractures in each case. The

results given are an average over 50 realisations. It can be seen that the average density and average number of intersections are related as predicted in §3.5 and that the average number of intersections at percolation is decreasing slightly as α decreases. It should be remembered that more fractures are present in the fixed size region for smaller α and so the finite-size effects account for some of this decrease. For the smallest α values the number of intersections increases again. We will see in the next example that this occurs even when we know that it must be constant. It must therefore be due to the finite size region, and in particular the aspect ratio of this region as compared to the spread of angles. The region is effectively much wider at small α and so the calculated percolation density is increased.

The $\alpha = 90°$ case is the case considered by Pike and Seager. They obtain the result $I_c = 3.635$ and $\rho_c = 1.428$, giving a ratio which agrees with the predicted figure of 2.546. Since they have only used 1000 lines and have a percolation criterion based on two opposite sides being connected we would expect their result to be lower than ours. Also they have taken just 10 realisations giving error bars of ± 0.03 for the density. Given all these differences our results agree well with tieirs.

The second example was for the case with a fixed length of 2 units and orientations at $\pm\alpha$ from the horizontal. This is the case which we proved in §3.7 had I_c independent of α. The results presented in table 3.5 are for 50 realisations with over 10000 fractures in each case.

α	Density ρ		Intersections I		Ave. I / Ave. ρ	$2\sin 2\alpha$
	Average	Std. Dev	Average	Std. Dev		
45°	1.587	0.0565	3.171	0.1131	1.998	2.000
40°	1.616	0.0605	3.175	0.1149	1.965	1.970
35°	1.685	0.0569	3.161	0.1052	1.876	1.879
30°	1.835	0.0685	3.178	0.1160	1.732	1.732
20°	2.526	0.0867	3.248	0.1134	1.286	1.286

Table 3.5

Results for bimodal distribution of orientations.

Again the relationship between the average number of intersections and the density is as predicted in §3.5. I_c is constant, as predicted, except for the smallest angle. This is the same as for the previous example, presumably being due to the effective width increase for small α.

Balberg and Binenbaum have looked at this case and obtained a critical density of 2.41 for α=45°. They have used systems of only 100 lines, so we must assume that their result is so different because of the effect of small networks.

The third example looks at the way variability in fracture lengths affects the critical density. The predicted result from §3.7 has been checked.

In this example the fractures are oriented in uniformly random directions and their lengths are uniformly distributed in the interval $(2(1-\theta),2(1+\theta))$ for a range of θ between 0 and 1. The predicted behaviour derived in §3.7 was that density would be proportional to $(1+\frac{1}{3}\theta^2)^{-1}$.

θ	Density ρ		Intersections I		Ave. I / Ave. ρ	$\rho(1+\frac{1}{3}\theta^2)$
	Average	Std. Dev.	Average	Std. Dev.		
0.0	1.434	0.0624	3.650	0.1568	2.545	1.434
0.2	1.428	0.0532	3.640	0.1325	2.549	1.447
0.4	1.370	0.0614	3.493	0.1568	2.550	1.443
0.6	1.301	0.0469	3.320	0.1143	2.552	1.457
0.8	1.207	0.0523	3.077	0.1318	2.549	1.464
1.0	1.095	0.0304	2.788	0.0952	2.546	1.460

Table 3.6
Results for uniform distribution of fracture lengths.

It can be seen from the results in table 3.6 that the average number of intersections over the density is consistently close to the theoretical value of $\frac{8}{\pi} = 2.546$. The predicted change in critical density is close to the calculated value, giving an error of around 2%. For the large values of θ there are less lines generated so the finite size effect will push up the calculated density and explain some of the discrepancy.

The fourth example takes a different line length variation. This time the lines have lengths 2 or $2l$ with equal probability. l is taken between 0.0 and 1.2. In each case 50 realisations were done. The results are presented in table 3.7. The theoretical prediction is that $\rho\frac{1+l^2}{2}$ is constant, its value is given in the final column.

The $l=0$ result here was not actually calculated separately but was deduced from the $l=1$ case. The theoretical result again seems to work well in these cases. The least good results are for $l=0.2$ and $l=0.4$ although even these are only 2% in error.

These results have demonstrated that the formulae relating density and average number of intersections derived in §3.5 are correct. The predicted change in critical densities caused by introducing a variable fracture length gave a very good estimate for the calculated values. For the case of fractures oriented in one of two directions the critical number of intersections was found to

l	Density ρ		Intersections I		Ave. I / Ave. ρ	$\rho\frac{(1+l^2)}{2}$
	Average	Std Dev	Average	Std. Dev		
0.0	2.868	0.1248	1.825	0.0748	0.636	1.434
0.2	2.810	0.0945	2.577	0.0958	0.917	1.461
0.4	2.529	0.0879	3.158	0.1102	1.248	1.467
0.6	2.128	0.0885	3.470	0.1488	1.630	1.447
0.8	1.748	0.0675	3.604	0.1397	2.063	1.433
1.0	1.434	0.0624	3.650	0.1568	2.546	1.434
1.2	1.178	0.0463	3.633	0.1438	3.081	1.437

Table 3.7
Results for bimodal distribution of fracture lengths.

be constant as predicted, although in this case and for the uniform angle case the finite size region seemed to affect the results for small angles. In general it is clear that the finite size effect must be considered when comparing calculations for different fracture statistics.

The calculations on critical density variation with region size showed that the critical density decreases with increasing region size. The form of this decrease is consistent with the finite size scaling argument prediction of R^{-1}. The spread of densities at which percolation occurred also fell as R^{-}, so that for the largest case considered 90% of the realisations percolated at between 246,500 and 257,200 fractures, a range of only 4.2% of the average value.

In three dimensions the computation becomes more difficult. With planes 1 unit by 1 unit in a region of 50 by 50 by 50 there are over 200,000 fractures. Again a special computer program to deal with the case of three orthogonal fracture sets was written. All the fractures had sides parallel to one of the coordinate axes. The effect of using different percolation criteria was tested by calculating the density to give a cluster connecting any pair of opposite faces of the cube, as well as the density for a cluster connecting all six faces. Table 3.8 presents the results. In each case 100 realisations were done, except for the largest cube for which 50 realisations were done. In all cases the time taken pc. plane per realisation was just less than 60μsecs.

The pattern of results is similar to the two dimensional case, with the two definitions of percolation giving results that get closer as cube size increases. The scaling arguments this time predicts a decrease with C^{-1}, where C is the cube size. A least-squares fit to the results gives a limiting value of 0.1874, in good agreement with the trend of the average results. This limit corresponds to an average number of intersections of almost exactly 2.0. This compares with the theoretical prediction in §3.7 of 2.09. Figure 3.9. shows all these results and the predicted behaviour.

	Six faces			Two faces			
Cube Size	No. of Fractures	Density Average	Density Std. Dev.	Density Average	Density Std. Dev	Difference	Average
10	2197	2064	0131	1842	0134	0222	.1953
15	6536	1995	0087	1830	.0091	0165	.1913
20	14593	1970	0057	.1855	.0069	.0115	.1913
25	27282	.1940	.0054	.1845	.0063	0095	.1893
30	45921	.1927	.0039	.1853	.0051	.0074	.1890
35	71496	1916	.0034	.1856	.0040	.0060	.1886
40	105398	.1912	.0030	.1857	.0030	.0055	.1885
45	148094	.1902	0024	.1854	.0027	.0048	.1878
50	201906	.1903	.0022	.1856	.0028	.0047	.1879

Table 3.8
Comparison between original percolation criterion and two-faces criterion.

One other three dimensional case has been considered. This is the case of uniformly distributed orientations. Planes of size 1 unit square were used in a cube of side 20 units. The average over 100 realisations gave an average critical density of 1.231 planes per unit volume with an average of 2.461 intersections per plane. The ratio of 2.0 between these figures in as predicted in §3.5. As for the the two dimensional case the number of intersections at percolation is larger in the random case than in the orthogonal case, while the density is higher in the orthogonal case.

3.9 Summary and conclusions

The results of this chapter have shown that, in two and three dimensions, there is a critical density of fractures, above which large scale paths exist. The critical density occurs when the average number of intersections per fracture reaches a critical value. This average is weighted by fracture size. The critical value is around 3.1 for two dimensional systems and 2.0 for three dimensions.

In the three dimensional case we can say that if we put a borehole through all three fracture sets then the system will be percolating if the separation between fractures and the borehole is less than about $\frac{1}{7}$ of the typical fracture size. So if we find a separation of ten metres we can say that the system percolates if the fractures are bigger than 14 metres across.

In two dimensions the fracture separation is much less at percolation. Here the separation must

be less than 1/4 of the fracture length. So with a separation of 10 metres the fractures have to be over 40 metres long for the system to percolate.

From a purely percolation theory point of view the results have shown that the arguments from finite-size scaling can be used and correctly predict the critical density versus region size curves when using the lattice critical parameters.

The techniques developed to find the fracture intersections quickly are invaluable in the later work. They may also be useful in other percolation studies.

Chapter 4 Flow

4.1 Introduction

The modelling of groundwater flow systems has been dominated by the use of Darcy's law. This law, first suggested by Darcy in 1856, relates the average velocity of a fluid through a medium to the pressure gradient. It is usually written

$$\mathbf{u} = -\frac{K}{\mu}\nabla P \tag{4.1}$$

where $\mathbf{u}$ is the average velocity, ∇P is the pressure gradient, μ is the fluid viscosity and K is the permeability of the medium. This equation has been found to be valid for many porous media and can be derived theoretically under certain assumptions (Bear,1972). The pressure referred to here is the non-hydrostatic pressure as it is throughout this work.

In the case of flow through a fractured rock it is not clear whether Darcy's law is valid. In order to define an average velocity it is necessary to take a flux averaged over some cross-sectional area. This area must clearly be larger than the microscopic scale of the medium so that it includes a representative number of flow paths. For a fractured rock the 'microscopic' scale as far as groundwater flow is concerned can be several metres or tens of metres (Bourke et al.1982). In this case the averages must be over very large regions. Measured permeabilities of fractured rock vary over orders of magnitude (Brace,1980).

The purpose of the work presented in this chapter was to find under what conditions Darcy's law is valid for a fractured medium and, when it is valid, to find how the permeability relates to the statistical properties of the fracture system. Long (1983 and Long et al.1982) has also looked at the permeability of fracture networks, concentrating on the question of directional permeability. It has not been possible to compare our results with theirs as yet. Some experimental work on lattice conductivity has been reported (Last and Thouless,1971, Watson and Leath,1974, Shankland and Waff,1974). Koplik (1981) has looked at conductivity in a square lattice numerically.

4.2 The physical problem

The method we have used to address the question of flow through fractured rock is to generate two-dimensional fracture systems with given fracture statistics and to perform numerical experiments on these systems. The assumptions made about the flow were as follows. In each fracture segment, that is between each pair of intersections, we assume that the flux is proportional to the pressure gradient. The constant of proportionality is defined in terms of the effective aperture. At intersections we assume that there is no significant head loss, so that it is sensible to define a single pressure at the intersection. At each intersection there is mass balance. The assumption of proportionality between pressure gradient and flux within each fracture segment is reasonable for the cases of interest here where the flow is slow and so inertial effects can be ignored. If we think of the fracture segments as parallel sided planar openings then the relationship between flux and pressure gradient is given by

$$q = \frac{t^3}{12\mu}\frac{P_1 - P_2}{l} \tag{4.2}$$

where q is the fluid flux, t is the fracture aperture, l is the length and $P_1 - P_2$ is the pressure drop in the direction of flow. In this case the constant of proportionality is $\frac{t^3}{12\mu}$. We might alternatively think of the fracture as being full of some high permeability material, in which case it might be more appropriate to use Darcy's law in the individual fractures. This would give a constant of proportionality $\frac{tK}{\mu}$, where K is the permeability of the fracture filling. We could then define the effective hydraulic aperture to be the aperture which gives this value. So whichever way we think of fractures we can define an aperture for each one.

4.3 Computational technique

A realisation of a given set of fracture statistics is generated within some region of the plane, the generation region. Then, for any particular flow calculation, a solution region is defined. The sides of this region can be designated as no-flow or specified pressure boundaries. For a no-flow boundary no intersections with the fracture system need be found. For a specified pressure boundary all the intersections with the fracture network must be located. The method for finding the intersections in the fracture network is essentially that used in the percolation calculations and described in §3.4. The difference is that slightly more information must be kept. After the intersections have all been found we have the following information for each fracture.

- the number of intersections (including specified pressure boundaries)
- the fractures (or boundaries) at these intersections
- the position of the intersections.

From this information we must form the matrix equation whose solution gives the pressures at each intersection and hence the flows. The first thing that we do is to reduce the number of intersections involved in the calculation. This is done by removing dead-ends and isolated clusters. figure 4.1 shows an example of each type of non-flowing fracture and shows which intersections can be excluded. The removal of dead-ends is straight forward, we simply run through the list of fractures removing any which do not intersect two or more other fractures. If they intersected one other fracture then the corresponding entry for this is deleted. This process is repeated until no more fractures can be removed. The removal of isolated clusters is not so straight forward. It must be done however, not only to reduce the number of variables, but because they lead to singular submatrices. The way these are removed is by finding which cluster each fracture is in, and which clusters touch a boundary. All fractures in clusters which do not touch a boundary or which touch a boundary in one position only are removed.

There is one more class of non-flowing fractures shown in figure 4.1, these are in parts of clusters which are connected to the main flow system by a single fracture. These are quite difficult to find, requiring each fracture to be removed in turn and the clusters recalculated. The potential savings in terms of reducing the number of variables are not great enough to justify their removal, it is better to let the matrix solver calculate the zero fluxes in them.

We now have a list of all intersections to be included in the matrix equation. This equation arises from the mass balance at each intersection

$$\sum_j q_{ij} = 0 \tag{4.3}$$

where q_{ij} is the flux from intersection i to intersection j

$$q_{ij} = \sigma_{ij}(P_i - P_j) \tag{4.4}$$

with σ_{ij} the conductivity of the link from i to j

$$\sigma_{ij} = \frac{t_{ij}^3}{12\mu l_{ij}} \tag{4.5}$$

t_{ij} is the effective aperture of the link and l_{ij} is its length. P_i is the pressure at intersection i. Combining (4.3) and (4.4) we have

$$(\sum_j \sigma_{ij})P_i - \sum_j \sigma_{ij}P_j = 0 \tag{4.6}$$

We also have boundary conditions on the specified pressure boundaries

$$P_j = P(x_j, y_j) \tag{4.7}$$

so we end up with

$$(\sum_{all\ j} \sigma_{ij})P_i - \sum_{internal\ j} \sigma_{ij}P_j = \sum_{boundary\ j} \sigma_{ij}P(x_j, y_j) \tag{4.8}$$

Because any particular intersection can only have four neighbours the matrix is sparse, with at most five entries per row. In order to save space only the non-zero elements are stored. So for any row we store

k_i – the number of non-zero entries

$c_{i1}, c_{i2}, \ldots, c_{ik_i}$ – the column numbers for the non-zero entries

$v_{i1}, v_{i2}, \ldots, v_{ik_i}$ – the values of the non-zero entries

b_i – the right hand side.

Because the matrix is so sparse it is tempting to use an iterative solver (e.g. Gauss–Seidel, Jacobi or SOR). However the matrix is very ill-conditioned, because it is only just diagonally dominant, and these methods all converge extremely slowly. We have also tried a semi-iterative solver, the pre-conditioned conjugate gradient algorithm (Jackson and Robinson, 1982). This performed much better than the classical methods but, while producing the solution, was still slower than we had hoped.

Using a direct solver on the matrix as it stands would be very expensive and would require large amounts of computer space. We have found that by renumbering using a method based on the Cuthil-McKee algorithm (Cuthil and McKee,1969) the bandwidth can be reduced sufficiently to make a fast variable bandwidth solver practical. In order to allow for very large problems an out of core version of this solver was also written. For both the in core and out of core versions significant speed gains have been made on the CRAY-1S at Harwell by using full vector facilities of this machine. The out of core solver will deal with systems of 20000 intersections and a reduced bandwidth of 160 in 13 seconds on the CRAY-1S (including the renumbering). Small problems with less than 4000 intersections are solved in less than one second.

The renumbering algorithm can be described as follows. First the intersections along one specified pressure boundary are renumbered in sequence along the side to be the first variables. Then we run through each already renumbered variable and assign new numbers to all intersections connected to it that have not yet been renumbered. This results in the numbering running from the first side across the network to the opposite side. This can best be understood by an example. Figure 4.2 shows the original numbering for an example, this has a maximum bandwidth of 10. The renumbering proceeds as follows. First those intersections along the left hand edge are renumbered starting with the intersection nearest the bottom left corner. Next the intersections connected with new intersection 1 are renumbered, followed by those connected to new intersection 2 etc. In each case if there is a choice of intersections for the next number the one with the lowest number originally is chosen. The final numbering is shown in figure 4.3. The maximum bandwidth is now just 3. For square regions the bandwidth will be approximately the square root of the number of intersections. For rectangular regions the starting side should be one of the shorter sides. The initial, essentially random, numbering will have a bandwidth of the same order as the number of intersections, N. The time taken by the solver is proportional to the number of intersections times the bandwidth squared, and is therefore reduced by renumbering from order N^3 to order N^2. The space required to store the matrix is also dramatically reduced, meaning that the in core solver can be used for larger problems.

Once the pressures have been found it is a simple matter to find all the fluxes. For the purposes of this chapter it is only the cross-side fluxes which are important. In the continuum approximation these would be equal and opposite on opposite faces, but for a fracture system this is only approximately true. The average velocity is calculated for each face and the average over the opposite faces is used to give the effective permeability tensor.

Notice that the fact that we can define an effective permeability tensor for any particular portion of a fracture system does not imply that Darcy's law is valid for modelling a system with these fracture statistics and size. There is necessarily a linear relationship between pressure gradient and cross-side velocity, because there is a linear relationship in all the fractures. In order for Darcy's law to be sensible the permeability tensor must be a property of the statistics not of the individual realisation and must be independent of the scale of the problem.

The computer program has been verified by checking against an independently produced code. This code also included transport and the comparison is reported in chapter 7. For small cases the code has also been checked by hand. The internal consistency of the program is constantly checked by calculating the total flux into the region. This should of course be zero, and is always found to be at least eight orders of magnitude down on the average flux, the error being caused solely by roundoff errors in the solver.

4.4 Theoretical estimates of permeability

Many attempts have been made to relate the permeability of porous media to the microscopic properties of the media. In porous media some work on obtaining bounds on permeability by using correlation functions has been done (Beran,1968) but this is inapplicable to fracture systems. In fracture systems an infinite parallel plate model is often used (Snow,1968, Caldwell,1972, Castillo,1972). In this type model the fracture system is replaced by sets of infinite planar fractures. The aperture of the fractures is chosen to give the correct porosity, that is the correct amount of open space per unit volume. Within each plane the Pousseille flow law is used. In the sort of two-dimensional system we are considering the fractures form an infinite regular lattice. In this section we use this type of model, with some extensions to predict the permeability of fracture networks. The first type of network we consider is one in which the fractures are all either horizontal or vertical.

As a first attempt to model this system we take the infinite square lattice shown in figure 4.4, with an aperture equal to the aperture of the fractures in the network. If the separation between bonds of the lattice is d and the aperture is t the conductivity of each bond is $\frac{t^3}{12\mu d}$. If there is a

pressure gradient parallel to one fracture set there will be a corresponding flow which implies a permeability of $\frac{t^3}{12d}$. The porosity of the system is $2\frac{t}{d}$ and so we have the relationship

$$K = \frac{\phi t^2}{24} \tag{4.9}$$

where K is the permeability and ϕ is the porosity. If the fracture network has two fracture sets, with all fractures having length $2l$ and aperture t and with a total density ρ, then the porosity is $2\rho lt$ and hence the permeability predicted by this model is $\frac{\rho l t^3}{12}$. This is clearly going to be an overestimate, since it neglects the discontinuities in the fracture system. It also has no cut-off at low densities, whereas we know that below the critical density there will be no flow.

In order to get a better approximation we proceed as follows. We take the full infinite lattice with the appropriate aperture and porosity and cut some of the links at random, as shown in figure 4.5. If we cut a proportion ε of the links the 'flowing porosity' will be less than the full porosity by a factor $(1-\varepsilon)$. By flowing porosity we mean the amount of space available for flow per unit area. For the fracture network we can also calculate a flowing porosity. The derivation and exact result is given below, but for fairly dense systems the result is the full porosity times $(1-\frac{2}{\lambda})$, where λ is the average number of intersections per fracture, and is given by $\lambda = 2\rho l^2$. We set $\varepsilon = \frac{2}{\lambda}$ and use effective medium theory (Landauer,1952, Kirkpatrik,1971) to give the reduction in permeability of the lattice. The factor for this case is simply $(1-2\varepsilon)$ or $(1-\frac{4}{\lambda})$. This gives us a new estimate for the permeability

$$K = \frac{\rho l t^3}{12}\left(1-\frac{4}{2\rho l^2}\right)$$

$$\text{or } K = \frac{l t^3}{12}\left(\rho-\frac{2}{l^2}\right) \tag{4.10}$$

We have already seen, in §3.8 that the critical density for this system is when $\lambda = 3.12$, giving $\rho_c = \frac{1.56}{l^2}$. This approximation for the permeability cuts the axis when $\lambda=4$ at a density 20% above the critical density. This is improved somewhat if we use the full formula for the flowing porosity of a network which we will now derive.

In the system above we showed in §3.5 that the number of intersections per fractures had a Poisson distribution with mean $\lambda = 2\rho l^2$. The flowing porosity is given by the full porosity times the average proportion of each fracture available for flow. This proportion is zero if there are less than two intersections on a fracture and is given by the separation of the two extreme intersections if there two or more. We need to calculate the average separation of the extremes of r values chosen at random between 0 and 1. The probability that the maximum of the r values is less than X is given by X^r, since all r values must be less than X. From this we find that the average maximum value is $\frac{r}{r+1}$. Similarly the average minimum is $\frac{1}{r+1}$ and the average difference is $\frac{r-1}{r+1}$. The average proportion over all the fractures is therefore given by

$$\sum_{r=2}^{\infty} \frac{\lambda^r}{r!} e^{-\lambda} \left(\frac{r-1}{r+1} \right) \tag{4.11}$$

which we can sum to give

$$(1-\frac{2}{\lambda}) + e^{-\lambda}(1+\frac{2}{\lambda}) \tag{4.12}$$

If we use this full formula for the flowing porosity we are led to set $\varepsilon = \frac{2}{\lambda} - e^{-\lambda}(1+\frac{2}{\lambda})$. This gives a zero permeability at $\lambda = 3.72$ which is slightly closer to the true value than before. The accuracy of this predicted permeability will be seen in the next section. Note that we have still overestimated the true flowing porosity since isolated clusters have not been taken account of. However the cut lattice model will contain isolated clusters too, so the prediction should not be greatly affected.

The analysis above used infinite lattices and was therefore only valid for large regions. In order to get some idea of the magnitude of the region size effect we now calculate the average permeability for very small regions. If we take a region a by a with $a \ll l$ then the average number of fractures crossing this region will be approximately $\rho a l$. The length of all the paths across the region will be a so the average permeability is $\rho l a \frac{t^3}{12a}$, that is $\frac{\rho l t^3}{12}$. This is precisely the value given by the full network, as it must be since all the fracture space is used. It is higher than the large region value by a factor $\frac{\lambda}{\lambda - 4}$ giving a marked effect at low densities.

This small region size effect presumably decays away for regions whose size is larger than the

fracture length. To get some idea how region size affects the permeability over the whole range we can argue as follows. The important thing about small regions which increases the permeability is that the boundaries intersect fractures which would otherwise be dead ends. In other words they increase the average number of intersections. In order to estimate the size of this effect we can simply replace λ in the previous formulae by κ, the average number of intersections including boundaries. The number of fractures intersecting the left and right boundaries if the region size is R is given by $2\rho lR$, the new average is therefore

$$\kappa = 2\rho l^2 + \frac{2\rho lR}{\rho R^2} \tag{4.13}$$

which gives

$$\kappa = 2\rho l^2 + \frac{2l}{R} \tag{4.14}$$

Note that for large R we have $\kappa \rightarrow \lambda$ and for small R $\kappa \rightarrow \infty$. These two limits give a result for the permeability which agrees with that already calculated. For some fixed R the value of λ when permeability is zero is given by

$$\lambda = 3.72 - \frac{2l}{R}. \tag{4.15}$$

The permeability predicted in this way is compared to the numerical results in the next section.

The above arguments can be generalised to cases with other orientation distributions. In all cases the coordination number, z, should be 4, since each intersection cannot be connected to more than four other intersections. In the effective medium analysis the factor multiplying the full lattice permeability depends only on z and on the proportion of missing links ε, the general form being $1 - \frac{z\varepsilon}{z-2}$. The things that do change are the flowing porosity, and hence ε, and the full lattice permeability. If we use a lattice which has infinite fractures in sets at orientations θ_i and with separations d_i and apertures t_i for $i=1,\ldots,n$ then the porosity of the full lattice is given by

$$\varphi = \sum_{i=1}^{n} \frac{t_i}{d_i} \tag{4.16}$$

and the permeability in the $\theta = 0$ direction is given by

$$K = \frac{1}{12}\sum_{i=1}^{n}\frac{t_i^3\cos^2\theta_i}{d_i} \tag{4.17}$$

If all the t_i and d_i are the same then we have

$$\Phi = n\frac{t}{d} \tag{4.18}$$

$$K = n\frac{t^3}{12d}\overline{\cos^2\theta} \tag{4.19}$$

which gives

$$K = \frac{\Phi t^2}{12}\overline{\cos^2\theta}. \tag{4.20}$$

For the square lattice θ was 0 or $\frac{\pi}{2}$ and so $\overline{\cos^2\theta} = \frac{1}{2}$. This value also applies for the case of uniformly distributed orientations. In fact it applies to all cases with fracture orientations equally spaced as a consequence of the identity

$$\sum_{k=0}^{n-1}\cos^2\frac{k\pi}{n} = \frac{n}{2} \qquad n\geqslant 2. \tag{4.21}$$

In all these cases therefore we have

$$K = \frac{\Phi t^2}{24}. \tag{4.22}$$

In the uniform distribution case with density ρ and lengths $2l$ we know that the average number of intersections $\lambda = \frac{8}{\pi}\rho l^2$, and so using the approximate result for flowing porosity we get

$$K = \frac{t^3 l}{12}\left(\rho - \frac{\pi}{2l^2}\right) \tag{4.23}$$

As before we could use the full formula for ε to give a slightly better result, and we could include the boundary effect by using $\kappa = \lambda + \frac{8l}{\pi R}$. The accuracy of this result will be tested in the next section.

As we pointed out in §3.5 the average number of intersections for cases with fracture length variation is the same as in the equivalent case with all lengths set to the average. However, the

distribution is not Poisson so the calculation of flowing porosity earlier in this section is not valid. For fractures of any particular length the number of intersections is a Poisson distribution so we can use the formula as before and average over lengths at the end. This gives us an average useful length

$$\int\left[\left(1-\frac{2}{\lambda(l)}\right)+e^{-\lambda(l)}\left(1+\frac{2}{\lambda(l)}\right)\right].l.f(l)dl \tag{4.24}$$

where $\lambda(l) = 2\rho\bar{l}l$.

If we take a uniform distribution with $l_{min}<l<l_{max}$ with average $\bar{l}$ this gives a factor

$$1-\frac{2}{\lambda_{av}}+\frac{(\lambda_{min}+3)e^{-\lambda_{min}}-(\lambda_{max}+3)e^{-\lambda_{max}}}{\lambda_{av}(\lambda_{max}-\lambda_{min})} \tag{4.25}$$

where $\lambda_{max} = 2\rho\bar{l}l_{max}$, $\lambda_{min} = 2\rho\bar{l}l_{min}$, $\lambda_{av} = 2\rho\bar{l}^2$. This implies a slight increase in permeability as the spread in fracture length increases. This will be seen in the experimental results reported in the next section.

If we allow a variation in the fracture aperture then it is not clear how we can best predict the result. We could allow a variation in the conductivity of the links in our lattice model but this is likely to be unsatisfactory because it ignores the fact that a wide fracture is wide all the way along and not just between one pair of intersections. The result has been calculated to check that this is so. We can see what sort of behaviour to expect if we argue as follows. At low densities there are very few paths through the network and so the various conductivities will occur in series. In this case then the permeability is likely to relate to the harmonic average of the individual conductivities, and in particular if there are any very narrow fractures they will effectively block the paths and so produce a low permeability. At high densities the situation is different. Here there are many interconnected paths and the permeability will depend more on the arithmetic average of the individual conductivities. Narrow fractures can easily be bypassed while wide ones will form good flow paths and will push up the permeability.

Below we calculate the effective medium, harmonic and arithmetic averages for the case of uniformly distributed apertures.

In terms of apertures the effective medium theory requires

$$\int \frac{t^3 - t_e^3}{t^3 + t_e^3} f(t)\, dt = \frac{\varepsilon}{1-\varepsilon} \tag{4.26}$$

where $f(t)$ is the probability density function for the apertures and t_e is the effective medium aperture. The permeability calculated using t_e from by this formula will have the missing link factor $1-2\varepsilon$ in it.

The harmonic average t_h is given by

$$\frac{1}{t_h^3} = \int \frac{f(t)}{t^3}\, dt \tag{4.27}$$

and the arithmetic average t_a is given by

$$t_a^3 = \int t^3 f(t)\, dt. \tag{4.28}$$

For the harmonic and arithmetic average the missing link factor must also be included.

Table 4.1 shows how these averages depend on the spread of apertures in the uniform distribution case. The effective medium case is given for three values of ε, with the factor $1-2\varepsilon$ removed to allow comparison with the other averages.

$\frac{t_{min}}{t_{av}}$	$\frac{t_{max}}{t_{av}}$	$\frac{1}{1-2\varepsilon}\left(\frac{t_e}{t_{av}}\right)^3$			$\left(\frac{t_h}{t_{av}}\right)^3$	$\left(\frac{t_a}{t_{av}}\right)^3$
		$\varepsilon=0.0$	$\varepsilon=0.2$	$\varepsilon=0.4$		
1.0	1.0	1.0	1.0	1.0	1.0	1.0
0.9	1.1	0.9950	0.9913	0.9850	0.9801	1.01
0.8	1.2	0.9844	0.9655	0.9410	0.9216	1.04
0.7	1.3	0.9572	0.9242	0.8700	0.8281	1.09
0.6	1.4	0.9269	0.8692	0.7759	0.7056	1.16
0.5	1.5	0.8917	0.8036	0.6638	0.5625	1.25
0.4	1.6	0.8540	0.7310	0.5403	0.4096	1.36
0.3	1.7	0.8169	0.6557	0.4134	0.2601	1.49
0.2	1.8	0.7824	0.5821	0.2923	0.1296	1.64
0.1	1.9	0.7527	0.5138	0.1872	0.0361	1.81
0.0	2.0	0.7282	0.4535	0.1073	0.0	2.00

Table 4.1
Effective medium, harmonic and arithmetic averages for uniform aperture distribution.

As the density decreases the effective medium theory predicts a sharper fall in conductivity for the variable aperture case compared to the fixed aperture case. It will be seen how these averages compare with the experimental results in the next section.

4.5 Results of numerical experiments.

Numerical experiments have been carried out using the technique described in §4.3 for many different region sizes, fracture densities and fracture statistics. These have been compared to the predictions given in section §4.4 where possible. The first case to be considered was that of two orthogonal fracture sets with one set parallel to the pressure gradient. In this case all the fractures are of the same length and aperture. All that varies is the density of fractures and the size of the region used. The sides of the region parallel to the flow direction are no-flow boundaries in these cases, the effect of making them fixed pressure boundaries is investigated later. The fracture lengths are all 50 metres (l=25 metres) and the apertures 50 microns.

Density ρ 10^{-3} m	Region Size R	Number of runs	Permeability Ave. 10^{-10} m	Dev. 10^{-10} m	Min. 10^{-10} m	Max. 10^{-10} m	Pred. 10^{-10} m
2.00	200	100	0.08	0.21	0.0	1.07	0.0
2.00	400	40	0.01	0.04	0.0	0.24	0.0
2.50	200	100	0.48	0.55	0.0	1.99	0.0
2.50	400	40	0.32	0.28	0.0	0.96	0.0
3.00	200	100	1.10	0.63	0.0	2.75	0.43
3.00	400	65	0.79	0.39	0.0	1.57	0.24
4.00	10	200	7.74	8.68	0.0	41.67	6.25
4.00	50	200	4.68	2.66	0.0	15.22	3.54
4.00	100	200	3.55	1.54	0.0	7.56	2.96
4.00	200	200	2.99	0.91	0.0	5.57	2.63
4.00	300	100	3.02	0.62	1.10	4.08	2.52
4.00	400	165	2.93	0.47	1.45	4.06	2.46
4.00	500	100	2.92	0.34	1.99	4.18	2.42
4.00	600	100	2.87	0.30	1.70	3.49	2.40
4.00	700	100	2.88	0.24	2.16	3.46	2.38
4.00	800	100	2.84	0.23	2.26	3.27	2.37
4.00	900	125	2.90	0.23	2.33	3.40	2.36
5.00	200	100	5.55	1.00	2.95	7.60	5.06
5.00	400	40	5.30	0.48	4.35	6.28	4.91
6.00	10	300	11.76	10.53	0.0	43.90	10.63
6.00	50	100	8.65	3.58	0.0	20.46	8.28
6.00	100	100	7.91	1.97	2.53	12.78	7.83
6.00	200	100	7.92	1.03	4.92	10.74	7.58
6.00	300	100	7.77	0.65	5.98	9.27	7.49
6.00	400	124	7.85	0.45	6.42	8.86	7.45
6.00	500	50	7.72	0.36	6.72	8.58	7.42
6.00	600	50	7.81	0.29	7.19	8.35	7.40
6.00	700	25	7.80	0.28	7.07	8.23	7.39

7.00	200	100	10.50	1.19	7.10	12.66	10.13
7.00	400	40	10.42	0.54	9.10	11.34	10.02
8.00	200	125	13.02	1.13	10.42	15.39	12.71
8.00	400	65	13.00	0.47	11.76	13.89	12.60
9.00	200	100	15.71	1.17	13.06	18.46	15.29
9.00	400	25	15.41	0.54	14.48	16.66	15.20
10.0	200	100	18.26	1.18	15.47	21.36	17.87
10.0	300	50	18.20	0.87	16.22	19.83	17.82
10.0	400	50	18.26	0.54	17.06	19.24	17.79
11.0	200	100	20.76	1.22	18.22	23.12	20.46
11.0	400	25	20.70	0.56	20.05	21.92	20.39
12.0	200	125	23.45	1.32	20.19	26.47	23.05
12.0	300	50	23.53	0.80	21.77	25.44	23.01
12.0	400	50	23.35	0.65	21.88	24.79	22.99
16.0	200	25	33.86	1.31	31.42	36.83	33.44
20.0	200	25	44.03	1.84	39.94	47.58	43.83
24.0	200	20	53.47	2.33	49.52	58.50	54.24

Table 4.2
Results of region size and density variation runs for orthogonal fracture sets.

The critical density for this system is approximately 2.50×10^{-3} fractures per unit area in each set. Table 4.2 presents the results for various combinations of densities between 2×10^{-3} and 12×10^{-3} and region sizes between 10 and 900 metres. The predicted permeability uses the formula derived in §4.4

$$K = \frac{\rho l t^3}{12}\left(1-\frac{4}{\kappa}+2e^{-\kappa}\left(1+\frac{2}{\kappa}\right)\right) \tag{4.29}$$

with

$$\kappa = 2\rho l^2+\frac{2l}{R}. \tag{4.30}$$

It can be seen that this theoretical prediction gives good results for most cases. It breaks down for the very low density cases, because it fails to give the correct percolation value. For density 4×10^{-3} the predictions are consistently 15–20% low. For densities above this the predictions are very good, with less than 5% error in most cases.

If we concentrate on the variation of permeability with region size for a fixed density, we can see that there is a sharp decrease in calculated permeability initially and that, as the region size increases, the results settle down fairly quickly to a constant value. This value can be said to be the

infinite region permeability of the fracture system. Also, as the region size increases the variability in calculated permeability decreases. The standard deviation is given in the table. In order for the porous medium approximation to be useful the permeability on length scales of interest must have reached the infinite region permeability and the variability at this scale must be small. If we say that a standard deviation of 10% or the average value is acceptable then we can see that for $\rho = 4\times10^{-3}$ a region size of something over 600m is required as can be seen in figure 4.6. If the density is 6×10^{-3} then this is reduced to less than 300m, as figure 4.6 again shows, while for higher densities regions of size less than 200m are acceptable. At these region sizes the average value is within a few percent of the infinite region value, and the minimum and maximum values are within a factor of 2.0 of each other. The predicted average values of permeability are also shown in figure 4.6 and it can be seen that these predict the overall behaviour fairly well.

To see how well the predicted permeabilities do fit the calculated values for reasonably large region size we show in figure 4.7 the theoretical and experimental results for region size 400m with varying fracture density.

In these runs the top and bottom boundaries were taken as no-flow boundaries. A series of runs have been done with specified pressure boundaries to see how much this affects the results. In a real porous medium either boundary condition used here would give the same results. The results are set out in table 4.3. The permeability perpendicular to the pressure gradient comes from the net flux across the top and bottom faces, and indicates a local anisotropy. In these runs the density was fixed at 4×10^{-3}.

The first thing that can be said about these results is that the permeability is higher than with the fixed boundaries. This is because the number of flow paths has been increased – any fracture which cuts the top or bottom boundary is connected to any other fracture cutting the same boundary. For the large region size runs this increase is around 15% but for the small regions it is much greater. We can see that this increase in the average results more from an increase in the minimum than in the maximum, in other words the effect of open boundaries is to allow poorly connected networks to have significant flow.

The second thing to say is that the net flow leaving the sides is quite significant. For all cases the average was small but the range was large, with permeabilities up to 25% of the component parallel to the pressure gradient. This local anisotropy may well be significant in contaminant transport calculations.

Region Size	Parallel to pressure gradient			Perpendicular to pressure gradient	
	Ave. $10^{-16}\kappa$	Min. $10^{-16}\kappa$	Max $10^{-16}\kappa$	Min. $10^{-16}\kappa$	Max. $10^{-16}\kappa$
10	8.58	0.00	41.67	-3.54	4.55
50	5.95	1.30	13.52	-3.95	4.90
100	5.30	2.48	9.06	-2.17	2.13
200	4.30	2.52	6.59	-1.44	1.97
300	4.01	2.57	5.30	-1.08	1.26
400	3.76	2.84	4.81	-1.06	1.04
500	3.63	2.69	4.61	-0.93	1.00
600	3.48	2.71	4.18	-0.95	0.86
700	3.42	2.70	4.16	-0.72	0.78
800	3.37	2.59	3.99	-0.77	0.68
900	3.30	2.73	3.85	-0.71	0.58

Table 4.3
Results of region size variation runs for orthogonal fracture sets with specified pressure boundaries.

The high permeabilities calculated are unrealistic because they allow flow to leave the top or bottom at one point and re-enter anywhere else. For this reason we have used the no-flow boundary condition for the rest of the calculations.

We next looked at a uniform distribution of fracture orientations. The density was varied between 2×10^{-3} and 8×10^{-3} fractures per square metre. The region size was fixed at 400m and, except for the two largest densities, 100 realisations were done for each density. The fractures all had a fixed aperture of 50um and a fixed length of 50m. The results are presented in table 4.4. The theoretical results given are from the full formula with boundary corrections. The results for the equivalent orthogonal case are given for comparison. Figure 4.7 presents the same results graphically.

The theoretical estimates in this case are all too high, and are not as good as in the orthogonal case. The network is acting as if there are effectively fewer intersections per fracture. One possible reason for this is that when two nearly parallel fractures intersect they add more flowing porosity without proportionately increasing the permeability. Whatever the cause of the discrepancy it is clear that the slope of the results is well modelled and that the difference between these results and the orthogonal case are small, except near the critical density. For the case of fixed length, fixed aperture fractures we can therefore say that the porosity permeability relationship

$$K = \frac{\phi t^2}{24} \tag{4.31}$$

Density	Permeability				
	Ave.	Min.	Max.	Orthogonal case	Pred.
$10^{-3}\times$	$10^{-16}\times$	$10^{-16}\times$	$10^{-16}\times$	$10^{-16}\times$	$10^{-16}\times$
2.0	0.04	0.0	0.41	0.01	0.0
2.5	0.40	0.0	1.28	0.32	0.53
3.0	1.22	0.0	2.21	0.74	1.64
4.0	3.45	2.16	4.45	2.90	4.07
5.0	5.88	4.48	6.77	5.30	6.61
6.0	8.40	7.25	9.47	7.89	9.19
7.0	10.87	10.13	11.83	10.42	11.78
8.0	13.50	12.52	14.59	13.06	14.37

Table 4.4
Results of density variation runs for uniformly distributed fracture orientations.

gives a good estimate of the average permeability if ϕ is the flowing porosity provided that the density is not too close to the critical density for the particular orientation distribution.

We now turn to the case where either the fracture lengths or apertures or both are allowed to vary. We base these runs on the orthogonal case with a region size 400m and density 6×10^{-3} fractures per square metre.

For the length variation realisations we have taken a fixed aperture of 50μm. The fracture length was given a uniform distribution with average 50m but with a spread ranging from zero to 50m. Table 4.5 presents these results, in each case 100 realisations were done. Figure 4.9 presents the results graphically.

Minimum length	Maximum length	Permeability			
		Ave.	Min.	Max.	Pred.
		$10^{-16}\times$	$10^{-16}\times$	$10^{-16}\times$	$10^{-16}\times$
50	50	7.89	6.51	8.86	7.45
40	60	7.93	6.88	8.81	7.45
30	70	7.99	6.75	9.00	7.48
20	80	8.15	7.15	9.45	7.56
10	90	8.44	7.33	9.81	7.76
0	100	8.96	7.56	10.39	8.24

Table 4.5
Results of fracture length variation runs for orthogonal fracture sets.

The predictions come from the result of the previous section including the boundary correction. The increase in permeability with length spread is predicted reasonably well showing that most of the change in the permeability is due to the increase in flowing porosity.

The effect of varying the aperture is more difficult to predict. We argued that at high densities the arithmetic average of conductivities would be important while at low densities the harmonic average would dominate. The results presented in table 4.6. are for the fixed length 50m with the standard density 6×10^{-3} fractures per square metre and with uniformly distributed apertures.

Minimum aperture µm	Maximum aperture µm	Permeability Ave. $10^{-16}\times$	Min. $10^{-16}\times$	Max. $10^{-16}\times$
50	50	7.89	6.51	8.86
40	60	7.87	6.88	8.88
30	70	7.87	6.75	9.08
20	80	7.84	6.60	9.12
10	90	7.76	5.81	9.87
0	100	7.71	5.02	10.32

Table 4.6
Results of aperture variation runs for orthogonal fracture sets with fixed density.

In each case 100 realisations were done. The average permeability remains nearly constant, presumably this case falls between the high density and low density limits. The variability in permeability is greatly affected by the spread in fracture aperture. The region size required before the permeability settles down will therefore be somewhat larger when the fracture length varies.

In order to see how the density affects the results we repeated the case with apertures between zero and 100µm for a range of densities. These results are given in table 4.7 and in figure 4.9.

Density $10^{-3}\times$	Permeability Ave. $10^{-16}\times$	Min. $10^{-16}\times$	Max. $10^{-16}\times$	Average/ Fixed aperture average
4	1.56	0.19	2.86	0.54
6	7.71	5.02	10.32	0.98
8	16.13	12.46	19.04	1.24
10	25.71	21.76	29.46	1.39
12	35.71	32.17	40.61	1.52

Table 4.7
Results of aperture variation runs for orthogonal fracture sets with various densities.

These results agree qualitatively with the prediction and although it is difficult to say whether the ratio is tending to zero for low density and 2.0 for high density the results certainly do not contradict this. The effective medium results shown in table 4.1 give the correct trend as density

increases but are out by a large factor. $\rho=4\times10^{-3}$ corresponds to $\varepsilon=0.4$ and here the difference is a factor of five, while at the high density end the factor is two.

In a real system there is a strong possibility that fracture length and fracture aperture are correlated. In order to see how this might affect the prediction of the permeability of the system we have looked at the following case. Four fracture sets are present, two oriented parallel to the pressure gradient and two oriented perpendicular to it. In each direction one of the sets has length uniformly distributed between 20m and 50m, while the other has length between 50m and 80m. The apertures are also uniformly distributed, between 20μm and 50μm for the first set and 50μm and 80μm for the second. The lengths and apertures are therefore correlated, with the shorter fractures being thinner, the correlation coefficient is 0.75. We will compare the results from this case with the uncorrelated case, where the full range of lengths and apertures [illegible] occur in any combinations.

The general method for predicting the permeability using a cut lattice model is as follows. First we set up a rectangular grid with the same total fracture length per unit area as the network. Then we remove some links at random to reduce the fracture length per unit area to the flowing fracture length in the network. Thus we have the separation between the lattice links and the proportion cut. The aperture must then be fixed. This is done by taking a weighted average of the network apertures, the weight being the length of flowing fracture with a given aperture. The type of average used will depend on the degree of connectivity, as previously explained. For low densities a harmonic average of the conductivities will be best, and at high densities an arithmetic average of the conductivities. At intermediate densities the best average is unclear, for our case we have taken an arithmetic average of the apertures, which emphasises neither the particularly low conductivity links nor the high ones.

In our example, both for the correlated and uncorrelated cases, the above prescription gives a lattice separation of 6.67m and a proportion of cut links of 0.262. For the uncorrelated case we use the average aperture, 50μm. For the correlated case we find that the average flowing length of the short fractures is 22.10m, and for the long fractures 51.68m, giving a weighted average aperture of 56.01μm. The predicted permeabilities are therefore $7.431\times10^{-16}\mathrm{m}^2$ and $1.045\times10^{-15}\mathrm{m}^2$ for uncorrelated and correlated respectively, giving a ratio of 1.41.

The numerically calculated average permeabilities in the two cases were $8.38\times10^{-16}\mathrm{m}^2$ and $1.28\times10^{-15}\mathrm{m}^2$, which gives a ratio of 1.53. Thus the predictions are both too low, but the ratio is

quite reasonable. The ratio in the calculations is higher, implying that the wider fractures have a bigger effect than the lattice model predicts.

4.6 Summary and conclusions

The work presented in this chapter has shown that it is possible to calculate flow through large fracture systems. We can predict the average permeability for such systems by using a cut lattice model. This gives the correct behaviour for the change in permeability with fracture density, length spread and network size. The variability in permeability is reduced as the network size increases, reaching 10% of the mean value for networks larger than ten times the fracture length. The average value is also dependent on the network size. This dependence can be predicted by including the boundary intersections when calculating the average number of intersection, and hence the flowing porosity.

When the fracture aperture is allowed to vary the permeability is found to increase or decrease according to the fracture density. For well connected systems there are many interconnected paths and low aperture fractures are easily bypassed, while for poorly connected systems the paths are like chains and low aperture fractures cannot be avoided.

Chapter 5 Contaminant Transport

5.1 Introduction

Once the flow of water through a fracture system has been calculated and a permeability tensor deduced we have the parameters we need to set up a continuum model approximation to the flow. In many applications, including radioactive waste disposal, it is the movement of contaminants by the flow that is important. The major mechanism is advection, which is usually assumed to be related to the Darcy velocity through the relationship

$$\mathbf{q} = \phi \mathbf{v} \tag{5.1}$$

where $\mathbf{q}$ is the Darcy velocity, $\mathbf{v}$ is the average velocity for a contaminant particle and ϕ is the porosity. The next mechanism to consider is hydrodynamic dispersion. This is usually modelled by a diffusion-like equation with a dispersion coefficient measured experimentally. This coefficient may have components which depend on the local velocity. In this and the following two chapters we shall concentrate on advection and hydrodynamic dispersion. Other mechanisms include sorption and diffusion into the rock matrix, we discuss these further in chapter 11.

Hydrodynamic dispersion occurs as a result of differing path lengths in the fracture network. An individual particle of contaminant will, to some extent, choose its path randomly and a group of particles which are initially close will be dispersed.

There are two possible mechanisms at work randomising the particles' paths. The first occurs within each fracture, here molecular diffusion will spread contaminant across the width of the fracture, and along the length of the fracture. The second mechanism occurs at intersections, here contaminant arriving from all inflowing fractures is mixed and flows out with equal concentrations in each outflowing fracture. The exact cause of the mixing is unimportant. We shall show in the following that molecular diffusion alone is sufficient to cause mixing but the roughness of typical fracture will also contribute.

The molecular diffusivity will depend on exactly what contaminant we are concerned with, we denote it by κ. If the typical fracture aperture is t, the typical velocity of flow in a fracture is u and the typical fracture length is l, then the distance spread by the contaminant in the time to travel along a fracture is d_f given by

$$d_f^2 = \frac{2\kappa l}{u}. \tag{5.2}$$

If the fracture intersection is also of size t then the distance spread while passing through an intersection will be d_i given by

$$d_i^2 = \frac{2\kappa t}{u}. \tag{5.3}$$

For the cases of interest to us we have $\kappa \approx 2\times10^{-9}\,\mathrm{m^2/s}$, $t \approx 50\mu\mathrm{m}$, $l \approx 10\mathrm{m}$ and u between 10^{-7} m/s and 10^{-4} m/s. This gives d_l between 6cm and 60cm. and d_i between 140μm and 1.4mm. This implies that complete mixing occurs at intersections and that we can treat the concentration in a fracture as constant across the width. The contaminant in a fracture travels at the average flow velocity. that is the flux over the aperture. The aperture in this relation need not be the same as the effective aperture used for hydraulic conductivity. but they are assumed equal in this work.

In some cases we may wish to consider fracture zones. rather than single fractures. Then the intersections will be highly fractured. hydrodynamic dispersion will occur in the intersections and the complete mixing assumption is still reasonable.

5.2 The diffusion equation approximation

From the numerical calculations. of whatever sort. we obtain the output rate for a pulse input and for a step function input. From this we wish to estimate the coefficients in the diffusion like equation used to model the system as a continuum. In order to do this we compare the results with the analytic solution of the one-dimensional diffusion equation

$$\frac{\partial C}{\partial t} + u\frac{\partial C}{\partial x} = D\frac{\partial^2 C}{\partial x^2}. \tag{5.4}$$

The initial conditions for the pulse input are simply zero everywhere except for a delta function at the origin. The boundary conditions relevant to the continuum model are less clear. In the numerical calculation the concentration at the extremities is not constrained. so that the sides are effectively just monitoring points. not boundaries. This leads us to take the boundary conditions at infinity where the concentration and its derivative must be zero. The problem with boundary conditions is caused by the fact that we only have convection in the network and so only one boundary condition. whereas in the continuum we require two conditions.

The solution to the diffusion equation is the gaussian

$$C_p(x,t) = \frac{C_0}{\sqrt{\pi}} \frac{e^{-\frac{(x-ut)^2}{4Dt}}}{\sqrt{4Dt}}. \tag{5.5}$$

At time t the mass which has passed $x=l$ is

$$M_p(t) = \int_l^x C_p(x,t)dx = \tfrac{1}{2}C_0 erfc\left(\frac{l-ut}{\sqrt{4Dt}}\right). \tag{5.6}$$

The rate at which this mass passes $x=l$ is

$$R_p(t) = \frac{dM_p}{dt} = \frac{C_0}{\sqrt{\pi}} \frac{e^{-\frac{(x-ut)^2}{4Dt}}}{\sqrt{4Dt}} \frac{(l+ut)}{2t}. \tag{5.7}$$

We can deduce D and u from a knowledge of the arrival rates using several different methods. If the diffusion equation exactly modelled the system all would give the same result. The difference between the results indicates how far from diffusion-like the system is.

The first method is to obtain a least squares best fit to the arrival rate data, with the end of timesteps being the fitting points. This will tend to fit the peak of the arrival rate curve and ignore the tail. One disadvantage of this method is that it cannot be used very easily if only the arrival times of discrete particles are known.

The second method uses the 25% and 75% breakthrough times (any pair of percentages could be used). These are the times at which 25% and 75% of the mass has arrived. The analytic solution gives us the formula for these times which, noting that $erf(0.477) = \frac{1}{2}$, we can write as

$$\frac{l-ut}{\sqrt{4Dt}} = \pm 0.477. \tag{5.8}$$

So the breakthrough times t_{25} and t_{75} are the roots of

$$u^2t^2 - (2ul + 0.91D)t + l^2 = 0 \tag{5.9}$$

which implies that

$$t_{25} + t_{75} = 2\frac{l}{u} + 0.91\frac{D}{u^2} \tag{5.10}$$

and

$$t_{25}t_{75} = \frac{l^2}{u^2} \tag{5.11}$$

from which we can readily deduce D and u.

The final method involves calculating the average arrival time and other moments of the arrival time distribution. We write

$$<t^n> = \int_0^\infty t^n R_p(t)dt \tag{5.12}$$

and find that

$$\begin{aligned}
<t> &= \left(\frac{l}{u}\right)+\left(\frac{D}{u^2}\right) \\
<t^2> &= \left(\frac{l}{u}\right)^2+4\left(\frac{l}{u}\right)\left(\frac{D}{u^2}\right)+6\left(\frac{D}{u^2}\right)^2 \\
<t^{-1}> &= \left(\frac{u}{l}\right)+\left(\frac{D}{l^2}\right) \\
<t^{-2}> &= \left(\frac{u}{l}\right)^2+4\left(\frac{u}{l}\right)\left(\frac{D}{l^2}\right)+6\left(\frac{D}{l^2}\right)^2
\end{aligned} \tag{5.13}$$

These results can be derived by direct integration using the substitution $z = \frac{ut-l}{\sqrt{4Dt}}$ or by relating $<t^n>$ to the n-th derivative of the Laplace transform of $R_p(t)$. The Laplace transform of $R_p(t)$ is

$$R_p^*(s) = \frac{C_0 e^{\alpha l}}{(2D\alpha-u)\alpha}$$

where

$$\alpha = \frac{u-(u^2-4Ds)^{\frac{1}{2}}}{2D}. \tag{5.14}$$

From these results we can derive D and u, given l, in a number of ways. The more useful formulae are collected below

(i) from $<t>$ and $<t^{-1}>$

$$\begin{aligned}
u^2 &= l^2\frac{<t^{-1}>}{<t>} \\
D &= l^2<t^{-1}>-lu \\
\text{or}\quad D &= u^2<t>-lu
\end{aligned} \tag{5.15}$$

(ii) from $<t>$ and $<t^2>$

$$\frac{l}{u} = \tfrac{1}{2}(4<t>-(3<t^2>-2<t>^2)^{\frac{1}{2}})$$

$$D = u^2<t>-lu \tag{5.16}$$

(iii) from $<t^{-1}>$ and $<t^{-2}>$

$$\frac{u}{l} = \tfrac{1}{2}(4<t^{-1}>-(3<t^{-2}>-2<t^{-1}>^2)^{\frac{1}{2}})$$

$$D = l^2<t^{-1}>-lu \tag{5.17}$$

For any arrival rate data we can use any of these methods to derive values for the parameters D and u. If the data comes from a system which behaves exactly according to the diffusion equation then the method we use is irrelevant. By comparing the results of all the methods we can see how well the diffusion equation models the system.

In the fracture systems we have assumed a linear relationship between pressure gradient and flow rate, and between flow rate and contaminant velocity. The coefficients D and u will therefore both be proportional to the overall pressure gradient. The ratio $l^{(D)} = D/u$ is independent of the pressure gradient, and so is a property of the network. The dependence of this parameter on fracture statistics and region size will be looked at in the numerical calculations reported later. The other ratio which is only dependent on the network is the ratio between u and the Darcy velocity. If q is the Darcy velocity we write $\varphi = q/u$. φ is expected to be equal to the flowing porosity discussed in chapter 4.

5.3 Transverse dispersion

Up to now we have been looking at the longitudinal component of dispersion, that is the component parallel to the flow direction. The tranverse component is also important, and can be obtained from arrival information in a similar way.

For an infinitely wide system the arrival rate at $x=l$, with an initial pulse at the origin is

$$R_P(y,t) = R_P(t)\cdot\frac{e^{-\frac{y^2}{4D_T t}}}{\sqrt{\pi}\sqrt{4D_T t}} \tag{5.18}$$

where D_T is the tranverse diffusion coefficient. If the system is not infinitely wide, but has no flow boundaries at $y = \pm h$ the single multiplying factor is replaced by a sum,

$$R_P(y,t) = R_P(t)\cdot\frac{1}{\sqrt{\pi}\sqrt{4D_T t}}\cdot\sum_{k=-\infty}^{k=\infty} e^{-\frac{(y+2hk)^2}{4D_T t}} \tag{5.19}$$

For the cases we are considering the boundaries are far enough away to allow the simpler form, in this case we have

$$<y^2> = 2D_T<t> \tag{5.20}$$

and so we can find D_T from the spatial distribution of the arriving mass.

Chapter 6 Mass–Lumping Algorithm

6.1 Introduction

In modelling contaminant transport through a network the most natural technique is to follow particles through the network, allowing them to take random directions at intersections. This technique has been used and is discussed in the next chapter. In this chapter we discuss a different technique, which may provide a starting point for the inclusion of other mechanisms.

To begin with we assume that we have set up a network and solved the flow equations. We therefore know the geometry of the network, the pressure at each intersection and the apertures and conductivities of each link.

We wish to calculate the time dependent transport of some contaminant through the network. If phenomena such as sorption are to be included later we will need to know the concentration of contaminant at all positions at all times. In this technique we discretise in space and time so that the concentration is approximated by a piecewise constant function in space and is calculated at the end of discrete timesteps. The important thing is that the length of the sections over which the concentration is constant is chosen so that on a single timestep contaminant moves from one section to the next. The section lengths are therefore different in each link, but are always equal to the timestep multiplied by the flow velocity in the link. At intersections all arriving mass is split up so that the concentration in each outflowing fracture is the same.

The advantage of this technique over particle following is that concentration is known everywhere. Sorption and rock matrix diffusion depend on this concentration, so the model could be extended to include them. Finding local concentrations if particles are being followed is difficult unless a huge number of particles is used. The disadvantage is one of cost, particle following can be made very fast, and while this method can be speeded up on the CRAY it is still comparatively rather slow.

As stated above the algorithm seems straightforward, however there are a number of problems to be overcome.

The first problem is how to deal with intersections. We could treat them as points, with no mass of their own, through which the mass from inflowing fractures passes as it splits and goes to the outflowing fractures. Alternatively we could give them a finite size, so that mass resides at the fracture for one timestep before being split and moved on. There does not seem to be any strong

reason for choosing one method over the other. We have chosen the second, mainly because it is easier to program.

The second problem is that the fracture lengths are not going to be convenient multiples of the distance moved in a timestep. The number of sections along a fracture must be chosen to be the nearest integer to the true number. The error of up to half a timestep that this introduces will be of random sign and will therefore tend to cancel out after a few links. This is unlikely to cause any difficulties.

The third problem is that some fractures will have very slow flow. In any network there are bound to be some fractures which just happen to take almost no flow, either because they are poorly connected to the main flow paths or simply by chance. The algorithm as it stands requires a large number of sections for these fractures, since the section length is proportional to the flow rate. Since there is very little flow we cannot afford to waste time calculating concentrations for all these sections. We therefore impose an upper limit on the number of sections allowed per fracture, and if this limit is exceeded the fracture is treated separately. Any mass which moves into it is collected in a special lost mass section. As long as the amount of lost mass by the end of a run is small the overall results will not be affected. If there is too much lost mass the run must be repeated with a relaxed limit, or with longer timesteps.

The final problem is at the opposite extreme, very fast flowing fractures. If the time taken for flow between two intersections is less than half a timestep we must take some special action. The minimum time required by the normal algorithm is one timestep, and using that would lead to an error of up to one timestep which would accumulate as more fast flowing links were encountered. We get over the problem by jumping the mass around the intersection straight into the next fracture. This results in some intersections having more than three outputs, once the mixing which occurs at the jumped intersection has been taken into account.

Figure 6.1 shows the possible movements of mass on a single timestep.

6.2 Computational details

The implementation of the algorithm is more or less as stated above, except for a final stage which puts the information in a form which enables some of the fast library routines on the CRAY to be used. The sections are numbered so that, except at intersections, the mass in each section moves to the next higher numbered section. The other types of move are from section to intersection, intersection to intersection and intersection to section. Each of these types is dealt with in two parts. The first movement into any section or intersection is dealt with first, these can be done using the very fast GATHER and SCATTER routines on the CRAY. Subsequent movements into these sections require the mass to be added to that already present, these are done separately.

The timestepping uses two sets of arrays to store masses, these are used on alternate steps. For steps at which processing, such as cross section plots, is required the mass is dumped to backing store to be processed at the end of the run.

Usually mass starts on one side of a region at time zero and is transported across to the far side where the rate of mass arrival is monitored. Timesteps are continued until no more significant amount of contaminant is arriving. If results are required for a continuous input, or any other input function, they can be derived from the pulse input calculation. From the output rate the parameters for a diffusion like approximation can be derived as described in the previous chapter.

6.3 Results

As an example of the use of the mass-lumping program we have done 20 runs with a region 200m square. The fractures are all of length 50m and have aperture 50μm. There are two fracture sets, one horizontal and the other vertical, with 2.5×10^{-3} fractures per square metre in each. The pressure gradient imposed is 100 Pa/m and the viscosity 10^{-3} kg/m/s. The timestep was taken as 1 day with a check done at ½ day for one realisation.

We first describe the results for a single realisation. The network for this realisation is shown in figure 6.2. The flow calculation gave a permeability of $5.087\times10^{-16}\mathrm{m}^2$, slightly below average for these statistics. In the course of the mass transport calculations the fractures were divided into 26185 sections. Of the 890 intersection to intersection links 20 had very low velocities (more than 700 timesteps to move along them) and were therefore designated as lost mass links, the others had an average of 30 sections each. 36 links were very fast (less than half a timestep) and the mass entering these moved directly into the next sections. The initial arrival occurred after 161 timesteps and after 1117 timesteps the algorithm was terminated. At this point 0.74% of the mass had gone into the lost mass section and 0.39% was still in the network.

The breakthrough times are given in table 6.1.

Percentage Arrival	Time(days) 1-day timestep	½-day timestep	Least squares fit
initial	161.00	161.50	-
10%	223.40	223.37	201.26
25%	257.46	257.50	244.24
50%	307.54	307.33	303.59
75%	409.84	409.74	377.35
90%	534.55	534.65	457.94

Table 6.1
Breakthrough times for single realisation.

The results from the half day timestep run are also shown, it can be seen that reducing the timestep has little effect showing that the one day timestep is short enough. The least squares best fit for D and u were used to obtain the final column of the table. Figure 6.3 shows the full breakthrough curve with this fit. It is clear that the tail is much longer than this fit predicts. We can use the other methods to calculate D and u, these results are shown in table 6.2.

The results shown here are for the one day timestep, the half day timestep run gave almost identical results.

Method	u (m/s) $10^{-6}\times$	D m^2/s $10^{-5}\times$
Least squares	7.617	7.947
$<t>$ and $<t^2>$	7.155	10.30
$<t>$ and $<t^{-1}>$	7.059	8.024
$<t^{-1}>$ and $<t^{-2}>$	7.143	6.342
t_{25} and t_{75}	7.126	8.499

Table 6.2
Diffusion equation parameters using various methods.

We can also look at the mass distribution at a given time. This is shown after 80 days in figure 6.4. The mass present in slices across the network running from top to bottom is plotted as a histogram with the least squares fit prediction as a solid line. Figure 6.5 shows the cross section after 160 days, just before initial breakthrough. It is clear in both cases that the fit is not good, underlining the fact that the dispersion is not diffusion like.

The results for the twenty runs are given below. For these runs the 1 day timestep was used. The average lost mass was 0.56% and the average mass still in the network when the algorithm stopped was 0.24%. Figure 6.6 shows the average arrival rate. This shows a sharp initial rise with a very much longer tail. The D and u calculated from this curve show the same behaviour as for the single run, with the weight given to the tail determining the size of D. The breakthrough times for this average curve are given in table 6.3.

Percentage Arrival	Time(days) Average	Least squares fit	Minimum	Maximum
initial	134.00	-	134.00	195.95
10%	212.42	195.80	193.06	270.49
25%	245.26	237.15	221.76	305.79
50%	298.01	294.06	270.49	386.81
75%	378.54	364.63	334.03	523.73
90%	488.90	441.62	414.70	677.55

Table 6.3
Breakthrough times for average arrival curve and minimum and maximum over 20 realisations.

This table also gives the range of breakthrough times found over the 20 realisations, the range is fairly large presumably because these runs are for a low fracture density and small region. The effect of density and region size are looked at in the next chapter.

The calculated D and u values have a similarly large range, and the average values follow the same pattern as the single run, as table 6.4 shows.

Method	u (m/s) $10^{-6}\times$	D m^2/s $10^{-5}\times$
Least squares	7.769	7.421
$<t>$ and $<t^2>$	7.423	9.890
$<t>$ and $<t^{-1}>$	7.328	7.735
$<t^{-1}>$ and $<t^{-2}>$	7.402	6.240
t_{25} and t_{75}	7.493	7.790

Table 6.4
Average diffusion equation parameters using various methods.

The value of u is determined mainly by the position of the peak arrival rate, it therefore varies only a small amount according to the method used. D depends on the weight each method gives to the tail, and so varies much more.

The dispersion length, $l^{(D)} = D/u$, has been calculated for the runs using the least squares fit. It has an average of 9.68m with minimum 6.25m and maximum 18.18m. The ratio of Darcy velocity to u has an average of 7.05×10^{-6} with a variation from 4.98×10^{-6} to 8.40×10^{-6}. The average porosity of the networks is 10^{-5} and the average flowing porosity 6×10^{-6}, in fairly good agreement with the velocity ratio.

These results will be cross checked against the results of the particle following program in the next chapter.

The computer time taken for the mass moving step in these runs was 2 seconds per run. This time will be proportional to the number of intersections, N, to the power $\frac{3}{2}$. In these runs the average N was 600, so for a more realistic case with around 5000 intersections the time needed would be 50 seconds per realisation. We will see in the next chapter that a similar particle following run with 10000 particles would take less than 1 second. The algorithm described in this chapter is therefore not quick enough to use for large numbers of realisations. It does however have the potential to include the other mechanisms which the particle following method does not.

Chapter 7 Particle Following Algorithm

7.1 Introduction

If the only output required from a contaminant transport model is the arrival behaviour at some point or points, and no mechanisms other than convection and mixing are to be included, then a particle following method is ideal. In this method the contaminant is transported in discrete particles of fixed mass. Convection is simply modelled by the motion of the particles along fractures and mixing is modelled by allowing each particle to go down any outflowing fracture with probabilities proportional to the fluxes. For this approximation to complete mixing to be satisfactory a large number of particles must be followed.

The way we have implemented the algorithm means the the spatial distribution of contaminant at a given time is not readily available. The advantage gained in terms of computer time is substantial and was considered to outweigh the disadvantages. It is, in any case, possible to modify the algorithm to produce the information if it is required.

The basic method is as follows. At time zero the initial pulse input is divided among all the particles equally and they each start at an intersection. If input is along a side of the network then the probability of each particle starting at a particular intersection is proportional to the flux entering the network at that point. At each step the particles all move to a new intersection, according to a random number. The probability of going to each intersection is proportional to the flux from the current position to the new position. The time taken by each particle is recorded and updated on each step. Once all the particles arrive at the far side of the network the algorithm terminates. The reason that the spatial distribution is not easy to obtain is that the time for each particle at the end of a given step is different, depending on the route taken by the particle so far. The advantage of this is that the number of steps of the algorithm depends on the number of intersections on routes from side to side. This will be similar for all routes, including any with very slow flow, so the algorithm terminates in a predictable number of steps.

The only information required by the algorithm about the network is the probabilities and times for moves from each intersection. So for each intersection we must calculate

- the number of outflowing links
- the intersections at the end of these links

- the probability of moving down each link

- the time taken to move to the end of each link.

By using some special CRAY library routines the whole process can be vectorised over the number of particles and the time taken reduced to just 1μs per particle per step. So 10000 particles can be followed through a network with paths of length 100 in 1 second. On the IBM 3081K the same operations are 10 times slower.

The output from the particle following algorithm is a list of arrival times. These can be sorted so that a plot of mass arrived against time can be drawn and the percentage breakthrough times calculated. The averages $<t>$, $<t^2>$, $<t^{-1}>$ and $<t^{-2}>$ can readily be found and the continuum parameters D and u can be calculated in a number of ways, as described in chapter 5. The discrepancies between these ways of calculating the parameters will indicate how well (or badly) the continuum approximation fits the data. By taking averages over many realisations the average parameter values and the variation in these values can be found. The dependence of both averages and variations on region size and fracture statistics can be investigated.

7.2 Verification

The network flow and transport computer programs used throughout this work have been verified against an independently produced code, written by Schwartz and Smith (Schwartz et al.1983). The FORTRAN source was taken to the University of Alberta and run on the computer there. Because their program is less general than ours the comparison was done using a network generated by their program. The usual network generation routines in our program were bypassed and the network properties were read in directly.

Their program uses a grid on which fractures lie. This caused two problems. First, their program modifies the fracture lengths so that fractures end exactly on a grid line. This can cause fractures which should not meet to do so. Second, if two fractures are generated on top of each other they count as in single fracture in their program. In our program this would not normally happen and the fractures are treated as if they were parallel, with a small distance between them. These two problems were overcome by some modifications to our program so that it mimicked theirs. After

these changes the two programs produced identical results for number of intersections, number of boundary conditions, flow rates and permeabilities.

The two programs use different systems for generating the random numbers needed for particle following. The results were therefore not identical but the discrepancy in arrival times was well within the range of statistical fluctuations.

This intercomparison verified that there were no significant errors in either program.

7.3 Results

First, in order to confirm that the algorithm produces results consistent with the mass lumping algorithm, the example run of the previous chapter has been repeated, using 10000 particles. For convenience some of the results given there are repeated here.

The permeability calculated was of course identical. The particles had all passed through the network by 100 steps giving the arrival times shown in table 7.1.

Percentage Arrival	Time(days) This run	Mass lumping run
initial	161.84	161.50
10%	223.81	223.37
25%	257.87	257.50
50%	306.75	307.33
75%	411.48	409.74
90%	535.31	534.65
100%	8810.25	-

Table 7.1
Breakthrough times for particle following and mass lumping.

The agreement is almost exact, showing that both algorithms are behaving properly. The comparison of the calculated u and D show up discrepancies however, as table 7.2 shows.
It seems that the reason for these discrepancies is that for the mass lumping runs the last 0.5% of the mass was not allowed to arrive. This greatly affects the calculated $<t^2>$ and slightly affects $<t>$. The particle following run allows all the particles to arrive, the last one after 8810 days. The last few particles have a disproportionate effect on the averages and hence on D, and to a lesser extent on u. This again highlights the problem of using these averages to calculate D and u, in the rest of this chapter we have not used $<t^2>$ at all.

Method	This run		Mass lumping run	
	u (m/s)	D m^2/s	u (m/s)	D m^2/s
	$10^{-6}\times$	$10^{-4}\times$	$10^{-6}\times$	$10^{-4}\times$
$<t>$ and $<t^2>$	8.327	53.886	7.155	10.30
$<t>$ and $<t^{-1}>$	6.817	11.404	7.059	8.024
$<t^{-1}>$ and $<t^{-2}>$	7.045	6.850	7.143	6.342
t_{25} and t_{75}	7.106	8.565	7.126	8.499

Table 7.2
Diffusion equation parameters using various methods.

In the following work we use three ways of calculating D and u, we use the notation

u_1 D_1 calculated from t_{25} and t_{75}

u_2 D_2 calculated from $<t>$ and $<t^{-1}>$

u_3 D_3 calculated from $<t^{-1}>$ and $<t^{-2}>$.

Similarly we use Φ_1, Φ_2 and Φ_3 for the porosities v/u_1, v/u_2 and v/u_3 and $l_1^{(D)}$, $l_2^{(D)}$ and $l_3^{(D)}$ for D_1/u_1, D_2/u_2 and D_3/u_3.

We first looked at the effect of region size for networks with two orthogonal sets of fractures. All the fractures had length 50m and aperture 50μm with a density of 4×10^{-3} fractures per square metre. The region size ranged from zero to 800m. 100 runs were done for each size.

The permeability results for these runs were reported in chapter 4, where it was shown that the permeability average settles down to a constant value for regions of larger than 600m. At this region size the variations between runs were small. For the particle following runs reported here there are more things to consider. For some of the smaller regions there are cases with no flow, for these the various parameters cannot be defined so averages are taken over the flowing cases. The number of runs with no flow is indicated in brackets in the tables.

Table 7.3 shows the particle mean velocity, u, as calculated by the three methods. They clearly settle down to a constant value at around 600m, in a similar way to the Darcy velocity. The discrepancies between the three results are quite small and show some signs of reducing for the larger region sizes.

The porosity results are given in table 7.4. These appear to be tending to a value slightly below the geometrically calculated flowing porosity, 6×10^{-6}. For the low density used here a more exact calculation, taking account of isolated clusters, could well give the reduction needed.

Region Size	Number of realisations	u_1 Average $10^{-6}\times$	u_1 Std. Dev. $10^{-6}\times$	u_2 Average $10^{-6}\times$	u_2 Std Dev $10^{-6}\times$	u_3 Average $10^{-6}\times$	u_3 Std. Dev. $10^{-6}\times$
10	100(45)	20.41	1.42	20.08	1.75	20.21	1.47
50	100(12)	11.26	2.14	10.30	1.93	10.83	2.00
100.	100(7)	7.91	1.72	7.35	1.69	7.72	1.72
200	100	6.00	1.08	5.64	1.11	5.89	1.05
300.	100	5.76	0.85	5.49	0.86	5.65	0.84
400.	140	5.45	0.64	5.23	0.66	5.35	0.63
500.	100	5.36	0.47	5.18	0.47	5.27	0.46
600.	100	5.21	0.41	5.05	0.42	5.13	0.4[illegible]
700.	100	5.21	0.33	5.04	0.35	5.12	0.34
800.	100	5.12	0.33	4.98	0.34	5.04	0.33
900.	25	5.14	0.30	5.02	0.30	5.07	0.30

Table 7.3
Diffusion equation parameter u using various methods for different region sizes.

Region Size	Number of realisations	Φ_1 Average $10^{-6}\times$	Φ_1 Std. Dev. $10^{-6}\times$	Φ_2 Average $10^{-6}\times$	Φ_2 Std. Dev. $10^{-6}\times$	Φ_3 Average $10^{-6}\times$	Φ_3 Std. Dev. $10^{-6}\times$
10.	100(45)	7.60	3.46	7.76	3.56	7.68	3.50
50.	100(12)	4.80	1.66	5.20	1.71	4.95	1.66
100	100(7)	4.76	1.20	5.11	1.18	4.88	1.21
200	100	4.90	0.79	5.21	0.69	4.99	0.80
300	100	5.21	0.51	5.46	0.42	5.31	0.51
400.	140	5.30	0.40	5.52	0.33	5.40	0.39
500	100	5.43	0.26	5.62	0.23	5.52	0.25
600.	100	5.50	0.27	5.68	0.21	5.60	0.25
700.	100	5.52	0.20	5.71	0.19	5.62	0.18
800.	100	5.55	0.17	5.71	0.13	5.64	0.15
900.	25	5.61	0.11	5.75	0.09	5.69	0.10

Table 7.4
Flowing porosity ϕ using various methods for different region sizes.

We can look at the dispersion results in two ways, either as the coefficient D or as the dispersion length $l^{(D)}$. We first look at D, table 7.5 gives the results. D_1 and D_3 become very similar as region size increases, while D_2 is always 40% higher. Each is settling down to a constant value, although not as quickly as the velocities do, a region size of 1000m rather than 600m seems to be the size above which variation is small. The reason that D_1 and D_3 converge is that they both take little account of the tail of the arrival distribution. D_1 is derived from the 25% and 75% arrival times and so the tail has no effect and D_3 uses $<t^{-1}>$ and $<t^{-2}>$ which gives very small weight to the

tail. D_2 on the other hand uses $<t>$ which is greatly affected by the tail of the distribution. These results show that, even at large region sizes, the dispersion is not fully diffusion like.

Region Size	Number of realisations	D_1 Average $10^{-5}\times$	D_1 Std. Dev. $10^{-5}\times$	D_2 Average $10^{-5}\times$	D_2 Std. Dev. $10^{-5}\times$	D_3 Average $10^{-5}\times$	D_3 Std. Dev. $10^{-5}\times$
10	100(45)	0.08	0.41	0.22	0.64	0.09	0.25
50.	100(12)	6.30	4.92	6.00	2.97	3.35	1.49
100.	100(7)	7.34	5.42	8.67	4.80	4.98	1.95
200	100	8.46	4.32	11.92	7.46	6.94	2.03
300.	100	8.99	3.40	12.69	5.90	7.98	1.93
400.	140	9.75	3.42	13.68	4.79	8.94	2.09
500.	100	10.03	2.74	13.98	3.82	9.55	1.75
600.	100	10.97	2.88	15.06	4.94	10.47	2.07
700	100	11.07	2.72	16.57	7.72	10.90	2.21
800.	100	11.51	2.36	16.47	3.74	11.52	1.92
900.	25	11.35	1.96	15.79	3.10	11.33	1.61

Table 7.5
Diffusion equation parameter D using various methods for different region sizes.

The dispersion length results show very similar behaviour to the dispersion coefficient. Table 7.6 shows the results. The standard deviation of $l_2^{(D)}$ shows that not only does the tail of the distribution affect the average value but can cause large variations. This is due to occasional very slow particles.

Region Size	Number of realisations	$l_1^{(D)}$ Average	$l_1^{(D)}$ Std. Dev.	$l_2^{(D)}$ Average	$l_2^{(D)}$ Std. Dev.	$l_3^{(D)}$ Average	$l_3^{(D)}$ Std. Dev.
10.	100(45)	0.06	0.31	0.14	0.41	0.06	0.15
50.	100(12)	5.97	5.12	6.04	3.22	3.22	1.63
100.	100(7)	9.59	6.55	12.45	7.01	6.66	2.50
200.	100	15.07	10.19	23.46	19.97	12.29	4.69
300.	100	16.06	7.27	24.39	15.13	14.46	4.25
400	140	18.42	8.36	27.24	13.36	17.12	5.57
500	100	18.91	5.85	27.39	8.77	18.30	4.06
600.	100	21.26	6.37	30.40	12.92	20.63	4.83
700	100	21.37	5.65	33.43	17.89	21.44	4.86
800	100	22.58	4.98	33.42	8.75	22.99	4.23
900.	25	22.16	4.10	31.66	6.90	22.48	3.78

Table 7.6
Dispersion length $l^{(D)}$ using various methods for different region sizes.

The next set of runs was for a fixed region size, 400m, with fracture densities up to 12×10^{-3}

fractures per square metre. The other fracture statistics were as before, fixed length 50m and fixed aperture 50μm. Some of the low density runs gave no flow, the number of these is indicated in brackets in the tables, with the average given being over the flowing runs.

We know from chapter 4 that the Darcy velocity depends on density through the equation

$$v = -\frac{lt^3}{12\mu}(\rho - \frac{2}{l^2}) \cdot \frac{\partial P}{\partial x} \tag{7.1}$$

and that the flowing porosity is approximately

$$\phi = 2lt(\rho - \frac{1}{l^2}) \tag{7.2}$$

which gives a prediction for the particle velocity

$$u = -\frac{t^2}{24\mu} \frac{\rho l^2 - 2}{\rho l^2 - 1} \frac{\partial P}{\partial x} \tag{7.3}$$

For this case the large density limit is 10.42×10^{-6} m/s. Table 7.7 shows the numerical results for particle velocity. They agree fairly well with the theoretical prediction. The discrepancy between the different methods is small but does not get smaller as the density increases.

Density $10^{-3}\times$	Number of realisations	u_1 Average $10^{-6}\times$	u_1 Std. Dev. $10^{-6}\times$	u_2 Average $10^{-6}\times$	u_2 Std. Dev. $10^{-6}\times$	u_3 Average $10^{-6}\times$	u_3 Std. Dev. $10^{-6}\times$	u Predicted $10^{-6}\times$
2.00	40(39)	3.21	0.0	2.91	0.0	3.08	0.0	-
2.50	40(13)	3.25	0.90	2.95	0.86	3.17	0.87	-
3.00	40(4)	3.55	0.86	3.17	0.78	3.47	0.82	-
4.00	140	5.45	0.64	5.23	0.66	5.35	0.63	3.47
5.00	40	6.76	0.48	6.59	0.48	6.66	0.47	5.52
6.00	40	7.72	0.32	7.55	0.31	7.61	0.31	6.63
7.00	40	8.23	0.33	8.05	0.33	8.11	0.33	7.33
8.00	40	8.67	0.26	8.49	0.26	8.55	0.26	7.82
9.00	25	8.88	0.25	8.69	0.24	8.75	0.25	8.17
10.0	25	9.25	0.21	9.05	0.21	9.11	0.21	8.44
11.0	25	9.34	0.20	9.13	0.20	9.20	0.20	8.65
12.0	25	9.54	0.20	9.33	0.20	9.39	0.20	8.82

Table 7.7

Average particle velocity u using various methods for different fracture densities.

The porosity behaves just as expected, the results are given in table 7.8.

Density $10^{-3}\times$	Number of realisations	Φ_1 Average $10^{-6}\times$	Φ_1 Std. Dev. $10^{-6}\times$	Φ_2 Average $10^{-6}\times$	Φ_2 Std. Dev. $10^{-6}\times$	Φ_3 Average $10^{-6}\times$	Φ_3 Std. Dev. $10^{-6}\times$	Φ Predicted $10^{-6}\times$
2.00	40(39)	0.74	0.0	0.82	0.0	0.77	0.0	1.0
2.50	40(13)	1.46	0.41	1.60	0.42	1.49	0.41	2.25
3.00	40(4)	2.30	0.49	2.56	0.48	2.35	0.50	3.5
4.00	140	5.30	0.40	5.52	0.33	5.40	0.39	6.0
5.00	40	7.83	0.27	8.02	0.25	7.94	0.26	8.5
6.00	40	10.30	0.24	10.54	0.23	10.46	0.23	11.0
7.00	40	12.66	0.24	12.94	0.25	12.84	0.24	13.5
8.00	40	15.06	0.25	15.38	0.24	15.28	0.24	16.0
9.00	25	17.35	0.30	17.73	0.30	17.60	0.30	18.5
10.0	25	19.90	0.28	20.34	0.28	20.21	0.28	21.0
11.0	25	22.16	0.30	22.67	0.28	22.50	0.29	23.5
12.0	25	24.52	0.28	25.06	0.26	24.90	0.26	26.0

Table 7.8
Flowing porosity φ using various methods for different fracture densities.

The dispersion coefficient D is given in table 7.9. It appears to tend to a constant value, although there is no convergence of the three methods.

Density $10^{-3}\times$	Number of realisations	D_1 Average $10^{-5}\times$	D_1 Std. Dev. $10^{-5}\times$	D_2 Average $10^{-5}\times$	D_2 Std. Dev. $10^{-5}\times$	D_3 Average $10^{-5}\times$	D_3 Std. Dev. $10^{-5}\times$
2.00	40(39)	6.76	0.0	13.12	0.0	6.04	0.0
2.50	40(13)	12.79	15.05	17.85	8.53	9.03	4.62
3.00	40(4)	11.95	5.49	21.41	11.45	9.68	2.79
4.00	140	9.75	3.42	13.68	4.79	8.94	2.09
5.00	40	8.47	1.93	10.98	2.40	8.25	1.45
6.00	40	7.58	1.08	9.99	1.29	7.57	0.87
7.00	40	7.92	1.36	10.25	1.60	7.73	0.93
8.00	40	7.71	0.76	10.08	0.90	7.70	0.54
9.00	25	7.48	0.60	10.03	0.71	7.62	0.40
10.0	25	7.29	0.72	9.87	0.94	7.43	0.60
11.0	25	7.45	0.42	10.35	0.59	7.61	0.29
12.0	25	7.29	0.42	9.93	0.56	7.51	0.32

Table 7.9
Dispersion coefficient D using various methods for different fracture densities.

So, the discrepancy between methods is unaffected by density, and we saw in the previous runs that it was not affected by region size. It must therefore be a genuine property of these fracture systems, showing that dispersion in fracture systems is not diffusion like.

The dispersion length is also falling as density increases. In table 7.10 we can see that this fall off

is not as fast as the reduction in the separation between fracture intersections, which is inversely proportional to density. It is not clear whether the dispersion length is tending to a finite constant or whether it will eventually reach zero.

Density $10^{-3}\times$	Number of realisations	$l_1^{(D)}$ Average	$l_1^{(D)}$ Std. Dev.	$l_2^{(D)}$ Average	$l_2^{(D)}$ Std. Dev.	$l_3^{(D)}$ Average	$l_3^{(D)}$ Std. Dev.
2.00	40(39)	21.04	0.0	45.13	0.0	19.59	0.0
2.50	40(13)	41.77	50.28	64.69	34.71	29.33	14.13
3.00	40(4)	36.07	20.46	70.87	37.81	29.01	9.16
4.00	140	18.42	8.36	27.24	13.36	17.12	5.57
5.00	40	12.58	2.96	16.77	4.00	12.45	2.40
6.00	40	9.85	1.57	13.28	1.93	9.98	1.33
7.00	40	9.64	1.80	12.77	2.19	9.55	1.28
8.00	40	8.89	0.89	11.89	1.07	9.02	0.66
9.00	25	8.43	0.71	11.54	0.83	8.71	0.52
10.0	25	7.89	0.80	10.91	1.06	8.16	0.66
11.0	25	7.98	0.49	11.34	0.68	8.28	0.35
12.0	25	7.65	0.49	10.65	0.72	8.00	0.40

Table 7.10
Dispersion length $l^{(D)}$ using various methods for different fracture densities.

In order to look at the variation of dispersion length up to higher densities we used a smaller region size, 200m. This enabled us to go to densities of 24×10^{-3}. The dispersion length results are shown in table 7.11.

Density $10^{-3}\times$	Number of realisations	$l_1^{(D)}$ Average	$l_1^{(D)}$ Std. Dev.	$l_2^{(D)}$ Average	$l_2^{(D)}$ Std. Dev.	$l_3^{(D)}$ Average	$l_3^{(D)}$ Std. Dev.
4.	100	15.07	10.19	23.46	19.97	12.29	4.69
8.	25	7.26	1.03	10.09	1.37	7.01	0.80
12.	25	6.59	0.89	8.91	1.18	6.34	0.77
16.	25	6.14	0.66	8.47	0.84	5.96	0.46
20.	25	5.97	0.44	8.41	0.79	5.84	0.36
24.	20	5.71	0.59	7.78	0.87	5.63	0.48

Table 7.11
Dispersion length $l^{(D)}$ using various methods for different fracture densities for a smaller region.

These results confirm that there is no convergence of the three methods but it is still difficult to be sure what the final value of $l^{(D)}$ is. We can be sure that the dispersion length does not only depend on the distance between fractures. The other lengths in the problem are the region size,

which is ruled out because of the results of the runs with varying region size, and the actual fracture length. This is constant and we shall see that there are some grounds for believing that it is this length that is important at high densities, this is discussed in chapter 8.

We have looked at transverse dispersion as the fracture density changes. The fracture network statistics are the same as those used above, but instead of starting particles all along the side they are started from as near to the centre of the side as possible. This allows the transverse component to be found quite easily, but increases the variability of the results between realisations. The averages are still accurate enough to see the trends in values. In all cases the spread of particles is small compared to the width of the region used, which allows us to ignore the effect of the top and bottom boundaries. Table 7.12 summarises the results.

Density $10^{-3}\times$	Number of realisations	D_l Average $10^{-5}\times$	D_l Std. Dev. $10^{-5}\times$	D_T Average $10^{-5}\times$	D_T Std. Dev. $10^{-5}\times$	$\frac{Ave\ D_l}{Ave\ D_T}$
3.00	50(2)	8.58	7.14	1.73	1.60	4.96
4.00	50	6.58	3.95	1.93	1.14	3.41
6.00	100	6.66	4.50	1.03	0.37	6.47
8.00	50	6.50	1.64	0.708	0.29	9.18
10.0	50	7.21	1.87	0.485	0.20	14.9
12.0	25	7.13	1.83	0.355	0.12	20.1

Table 7.12
Transverse and longitudinal components of dispersion for different fracture densities.

We can see from these results that the transverse component decreases rapidly as density increases. This reduction is faster than the reduction in separation between fractures, which certainly implies that this component tends to zero as fracture density increases. In fact it is closer to the square of the separation. It is also clear from these results that any attempt to relate the two components by a simple ratio will not work, the ratio between them depends crucially on the connectivity of the network.

Finally we looked at the effect of network orientation on both components of dispersion. Using the same fracture statistics as before with a fixed density of 6×10^{-3} fractures per square metre and a region size of 400m, we rotated the whole system through various angles while keeping the flow direction constant. The results are presented in table 7.13, the angle is the angle between one fracture set and the flow direction.

Angle (degrees)	Number of realisations	D_l Average $10^{-5}\times$	D_l Std. Dev. $10^{-5}\times$	D_T Average $10^{-5}\times$	D_T Std. Dev. $10^{-5}\times$	$\frac{Ave\ D_l}{Ave\ D_T}$
0	100	6.66	4.50	1.03	0.37	6.47
5	80	5.56	1.65	1.17	0.45	4.75
10	80	5.03	1.61	1.16	0.48	4.34
15	80	4.56	2.39	1.42	0.55	3.21
20	80	3.92	1.50	1.39	0.45	2.82
25	80	3.13	1.05	1.40	0.51	2.24
30	80	2.47	0.83	1.70	0.66	1.45
35	80	1.82	0.79	1.81	0.58	1.01
40	80	1.83	1.22	1.86	0.50	0.98
45	80	1.63	0.84	1.92	0.69	0.85

Table 7.13
Transverse and longitudinal components of dispersion for different angles between flow direction and fractures.

As the angle to the flow direction increases the longitudinal dispersion coefficient falls quite rapidly, while the transverse component increases slowly. This is the same behaviour as for a full square lattice, where the maximum transverse component occurs at 45°, with the minimum longitudinal component. In the full lattice case both components have minimum values of zero, whereas here the minimum values are determined by the connectedness of the network.

Chapter 8 Theories of Dispersion

8.1 Introduction

The theory of dispersion in porous media has a long history. When dispersion is modelled by a continuum equation it is usual to use a diffusion-like (Fickian) equation. So, for a one-dimensional flow, we would use

$$\frac{\partial C}{\partial t}+u\frac{\partial C}{\partial x}-D\frac{\partial^2 C}{\partial x^2} = 0 \tag{8.1}$$

where C is the concentration at position x, time t, u is an average velocity and D is the dispersion coefficient.

Many attempts have been made to show that (8.1) holds and to calculate D (Scheidegger,1972) Random walk models envisage particles of contaminant undergoing a random walk through the porous medium, with the distance travelled and time taken for each step being random variables. By using the central limit theorem the probability distribution function for particle position can be shown to tend to a Gaussian. We relate this probability density to the concentration in the real system and hence deduce values for u and D from the mean and variance of the distribution.

Scheidegger (1954) introduced the idea of dispersivity, or dispersion length. We write

$$D = l_D u \tag{8.2}$$

and call l_D the dispersion length. In models where the step duration scales linearly with a change of velocity, l_D is a constant length, independent of the velocity and hence a property of the porous medium. This will not be true if molecular diffusion is significant or if the flow is turbulent.

Saffman (1959,1960) uses a random walk model for hydrodynamic dispersion and molecular diffusion. His results rely on a maximum time for a step determined by the molecular diffusion. If this is not imposed the second moment of the time-step length distribution is infinite and D is undefined. This model is discussed further later in this chapter. Saffman points out that it is the distribution of $\frac{X-uT}{\sqrt{T}}$ which becomes Gaussian according to the central limit theorem, and not $X-uT$, which has third moment $\overline{(X-uT)^3} \propto T$.

Fried and Combarnous (1971) review the historical developments in the area of dispersion in porous media and give some experimental results. They say that there is a systematic disagreement

between theory and experiment. Scheidegger has suggested that the steps in the random walk should be correlated. He introduced an autocorrelation function for the velocity and derived a telegraph equation for the concentration

$$\frac{\partial C}{\partial t}+u\frac{\partial C}{\partial x}-D\frac{\partial^2 C}{\partial x^2} = A\left(u^2\frac{\partial^2 C}{\partial x^2}+2u\frac{\partial^2 C}{\partial x\partial t}+\frac{\partial^2 C}{\partial t^2}\right) \tag{8.3}$$

This leads to a sharp cut off in concentration which moves into the medium with velocity $\sqrt{\frac{D}{A}}$ and does not fit experimental results.

Coats and Smith (1964) speculated that the discrepancy was due to dead end pores, in which only diffusion occurs.

Simmons (1982) has argued that correlations can greatly affect the validity of the Fickian assumption.

There is, then, no satisfactory theory of dispersion in porous media, and some doubt as to the validity of the Fickian continuum model, especially at small lengths.

In fractured rock the random walk model looks sensible, it is easy to think of the steps of the walk as the fractures, with complete mixing at intersections before the next step. The number of steps taken may be small, again casting doubt on the validity of the Fickian assumption. The hypothesis that complete mixing takes place at intersections has been verified experimentally by Krizek et al (1972) for a range of flow velocities.

We shall consider some random walk models and see what can be said about the effect of correlations between steps.

8.2 A simple random walk model

We start with a simple case to show how random walk models behave. We take a random walk where all the steps are of the same length but take a time which is randomly distributed with probability density $f(t)$. The mean value of t is denoted $\bar{t}$ and the variance σ^2. The time taken for N steps is given by

$$T_N = \sum_{i=1}^{N} t_i \tag{8.4}$$

where the t_i are independent samples of the distribution. It is clear that the average time is given by

$$T_N = N\bar{t} \tag{8.5}$$

and the variance by

$$\Sigma_N^2 = \overline{(T_N - \bar{T}_N)^2} = N\sigma^2. \tag{8.6}$$

By using Laplace transforms, or moment generating functions, we can say more.

Let

$$f^*(s) = \int_0^\infty e^{-st} f(t)dt \tag{8.7}$$

and

$$f_N^*(s) = \int_0^\infty e^{-sT_N} f_N(t_N)dT_N \tag{8.8}$$

We can see that

$$f_N(T_N) = \int_0^{T_N} f_{N-1}(T_N - t)f(t)dt \tag{8.9}$$

that is

$$f_N = f_{N-1} * f \tag{8.10}$$

where $*$ denotes the convolution operation.

Hence

$$f_N^*(s) = (f^*(s))^N \tag{8.11}$$

The Laplace transform of a probability density function is called the moment generating function because

$$f^*(s) = \sum_{r=0}^{\infty}(-s)^r\frac{\overline{t^r}}{r!} \tag{8.12}$$

So

$$1-s\overline{T_N}+\frac{s^2}{2}\overline{T_N^2}-\frac{s^3}{6}\overline{T_N^3}+ \quad = \left(1-s\bar{t}+\frac{s^2}{2}\overline{t^2}-\frac{s^3}{6}\overline{t^3}+ \quad \right)^N \tag{8.12}$$

which, by equating powers of s, gives the relationships

$$\overline{(T_N-\overline{T_N})^2} = N\overline{(t-\bar{t})^2} = N\sigma^2 \tag{8.13}$$

$$\overline{(T_N-\overline{T_N})^3} = N\overline{(t-\bar{t})^3} = N\mu_3. \tag{8.14}$$

The central limit theorem result is for $C_N = \dfrac{T_N-\overline{T_N}}{N^{\frac{1}{2}}\sigma}$. We can see that

$$\overline{C_N} = 0$$

$$\overline{C_N^2} = 1$$

$$\overline{C_N^3} = \frac{1}{N^{\frac{1}{2}}}\frac{\overline{(t-\bar{t})^3}}{\sigma^3} \tag{8.15}$$

So for large N $\overline{C_N^3}\rightarrow 0$ and we have a normal distribution.

For one particular $f(t)$ we can explicitly calculate $f_N(T_N)$. If

$$f(t) = \alpha e^{-\alpha t} \tag{8.16}$$

then

$$f^*(s) = \frac{\alpha}{\alpha+s} \tag{8.17}$$

which implies

$$f_N^*(s) = \frac{\alpha^N}{(\alpha+s)^N} \tag{8.18}$$

and consequently

$$f_N(T) = \alpha^N e^{-\alpha T} \frac{T^{N-1}}{(N-1)!} \tag{8.19}$$

This does not look like the normal distribution when written in this way this but by using Stirling's formula for the factorial and setting $C = \frac{\alpha T_N - N}{N^{\frac{1}{2}}}$ we can show that

$$f_N(C) \sim \frac{e^{-\frac{1}{2}C^2}}{\sqrt{2\pi N}} \tag{8.20}$$

We can see this in figure 8.1 where we plot $\sqrt{2\pi N} f(T_N)$ against $\frac{\alpha T_N - N}{N^{\frac{1}{2}}}$ for $N=10$ and $N=50$, as well as the Gaussian. $f_N(T_N)$ itself does not tend to a Gaussian. For $\alpha=1$ the maximum arrival time is at $N-1$ and the times after which 1% and 99% of the particles have arrived differ from the Gaussian results by over one time unit for all N, as can be seen from figure 8.2.

If there is a correlation between steps of the random walk this will affect the calculated dispersion coefficient and increase the number of steps before a Gaussian is reached. We again take the simple random walk with

$$\bar{t}_i = \bar{t}$$

$$\overline{(t_i - \bar{t}_i)^2} = \sigma^2 \tag{8.21}$$

but now also assume that

$$\overline{(t_i - \bar{t}_i)(t_j - \bar{t}_j)} = \sigma^2 V_{ij} \tag{8.22}$$

where $V_{ij} = v(|i-j|)$. If we take $v(k) = \lambda^k$ then we still have

$$\overline{T_N} = N\bar{t} \tag{8.23}$$

but now

$$\overline{(T_N - \overline{T_N})^2} = N\sigma^2 \frac{1+\lambda}{1-\lambda} - 2\sigma^2 \lambda \frac{1-\lambda^N}{1-\lambda^2} \tag{8.24}$$

The number of steps required before the final value of the dispersion coefficient is reached depends on λ, as does the final value.

If we wish to predict dispersion coefficients we cannot ignore correlations between successive steps. If they are ignored the resulting prediction will underestimate dispersion. Even in a more complicated model we can get some idea of the effect of correlations by multiplying the result of an uncorrelated model by $\frac{1+\lambda}{1-\lambda}$, where λ is the correlation coefficient between successive steps.

8.3 Random direction models.

In this section we look at a class of random walk models, where we assume that the probability distributions for direction, length and velocity of each step are independent of all previous steps but may be correlated with each other. The validity of this assumption is open to question, but we believe that the effect of correlations can be mimicked by varying the step length so that a step can include a number of correlated smaller steps. A wide range of models is covered by our assumptions, from simple random walks in one dimension to three dimensional random walks with any correlations within a step. Since the length scales involved can take any values the models can be used for flow in a fine grained porous medium or in a fractured rock.

From the statistics of the individual steps we deduce the distributions after a fixed time, and hence the dispersion coefficients. By doing this we are implicitly assuming that we can equate the probability density function for a single particle with the concentration. This seems to be a reasonable assumption. If we solve the one-dimensional diffusion equation (8.1) for a pulse initially at the origin we get the gaussian curve, which we can interpret as a probability density function for our single particle, which at time T has mean

$$\mu = uT \tag{8.25}$$

and variance

$$\sigma^2 = 2DT. \tag{8.26}$$

From these simple relationships we can deduce u and D.

The basic model

We suppose that the displacement on step j, (x_j, y_j, z_j), and its duration t_j are random variables with known probability density functions. The means and variances we denote by μ and σ^2 with

suffices x,y,z and t. The covariances we denote by σ_{xt} etc. The random variables for each step are identically distributed and independent of all other steps. The first of these assumptions corresponds to statistical homogeneity of the medium, the second seems unavoidable and was discussed in the previous section.

We denote the position after n steps by (X_n, Y_n, Z_n) and the time T_n. We therefore have

$$X_n = \sum_{j=1}^{n} x_j \qquad Y_n = \sum_{j=1}^{n} y_j \qquad Z_n = \sum_{j=1}^{n} z_j \qquad T_n = \sum_{j=1}^{n} t_j \tag{8.27}$$

After a large number of steps the joint distribution becomes multivariate normal. We concentrate on the joint distribution of X_n and T_n to simplify the analysis. Just how large n must be before we can use the normal we can estimate from the proof of the Central Limit Theorem given in section 8.2. from this we can see that we must have

$$\left|\frac{\mu_3}{n^{\frac{1}{2}}\sigma^3}\right| \ll 1 \tag{8.28}$$

by taking the next term in the expansions we also have

$$\left|\frac{\mu_4 - 3\sigma^4}{n\sigma^4}\right| \ll 1 \tag{8.29}$$

which is generally weaker than the previous condition but deals with cases where μ_3 is zero. In these formula we have used μ_3 and μ_4 to denote the third and fourth moments.

Probability density for X given T

If the above conditions hold for x and t we can write the joint probability density function of X and T, given n as

$$P(X\&T|n) = \frac{1}{2\pi n\sigma_x\sigma_t}\frac{e^{-\frac{1}{2}q}}{\sqrt{1-\rho^2}} \tag{8.30}$$

where

$$q = \frac{1}{1-\rho^2}\left(\frac{(X-n\mu_x)^2}{n\sigma_x^2} + \frac{(T-n\mu_t)^2}{n\sigma_t^2} - \frac{(X-n\mu_x)(T-n\mu_t)}{n\sigma_x\sigma_t}\right) \tag{8.31}$$

and

$$\rho = \frac{\sigma_{xt}}{\sigma_x \sigma_t} \tag{8.32}$$

is the correlation coefficient between x and t.

The probability density function for T alone, given n is

$$P(T|n) = \frac{1}{\sqrt{2\pi} n^{\frac{1}{2}} \sigma_t} e^{-\frac{1}{2}\frac{(T-n\mu_t)^2}{2n\sigma_t^2}} \tag{8.33}$$

We are interested in the probability density function for X at given T. This is given by

$$P(X|T) = \frac{P(X\&T)}{P(T)} = \frac{\sum_n P(X\&T|n)P(n)}{\sum_n P(T|n)P(n)} \tag{8.34}$$

All the $P(n)$ are equal so, converting the sums to integrals we get the approximation

$$P(X|T) = \frac{\int_n P(X\&T|n)dn}{\int_n P(T|n)dn} \tag{8.35}$$

Evaluation of the integrals

We wish to find the moments of this distribution, and so we must evaluate $\int_X X^r P(X\&T|n)dX$.

To do this we write

$$q = 2W^2 + \frac{(T-n\mu_t)^2}{n\sigma_t^2} \tag{8.36}$$

where

$$W = \frac{1}{\sqrt{2}\sqrt{1-\rho^2}}\left(\frac{(X-n\mu_x)}{n^{\frac{1}{2}}\sigma_x} - \rho\frac{(T-n\mu_t)}{n^{\frac{1}{2}}\sigma_t}\right) \tag{8.37}$$

We can then write

$$\int_X X^r P(X\&T|n)dX = \frac{1}{\sqrt{\pi}}\int_W X^r e^{-W^2} dW\ P(T|n) \tag{8.38}$$

where

$$X = \sqrt{2}\sqrt{1-\rho^2}\,n^{\frac{1}{2}}\sigma_x W + n\mu_x + \rho\frac{\sigma_x}{\sigma_t}(T-n\mu_t) \tag{8.39}$$

for conciseness we will write

$$a_1 = \rho\frac{\sigma_x}{\sigma_t} \qquad a_2 = \sqrt{2}\sqrt{1-\rho^2}\,\sigma_x \qquad a_3 = \mu_x - \rho\frac{\sigma_x}{\sigma_t}\mu_t \tag{8.40}$$

and

$$J_r = \frac{1}{\sqrt{\pi}}\int_W (a_1 T + a_2 n^{\frac{1}{2}} W + a_3 n)^r e^{-W^2}\,dW \tag{8.41}$$

J_r is just a polynomial in n. since the range of W is $-\infty$ to ∞ and the $\frac{1}{2}$ powers of n in the integrand always appear with odd powers of W. The first few values are

$$\begin{aligned} J_0 &= 1 \\ J_1 &= a_3 n + a_1 T \\ J_2 &= \tfrac{1}{2}a_2^2 n + (a_3 n + a_1 T)^2 \\ J_3 &= \tfrac{3}{2}a_2^2(a_3 n + a_1 T) + (a_3 n + a_1 T)^3 \end{aligned} \tag{8.42}$$

To evaluate $\int J_r P(T|n)dn$ and the denominator in (8.35) we need to evaluate

$$N_p = \int_0^\infty n^p P(T|n)dn \tag{8.43}$$

for integer p. This can be done by the substitution

$$v = \frac{T-n\mu_t}{\sqrt{2}\sigma_t n^{\frac{1}{2}}} \tag{8.44}$$

by noting that

$$n(v)+n(-v) = 2\frac{T}{\mu_t} + 2\frac{\sigma_t^2}{\mu_t^2}v^2 \tag{8.45}$$

$$n(v).n(-v) = \frac{T^2}{\mu_t^2} \tag{8.46}$$

and

$$N_p = \frac{4}{\sigma_t\sqrt{2\pi}(2p+1)}\int_0^{\infty} v\left(n(-v)^{p+\frac{1}{2}} - n(v)^{p+\frac{1}{2}}\right)e^{-v^2}\,dv \tag{8.47}$$

If we write $\bar{n} = \frac{T}{\mu_t}$ and $s^2 = \frac{\sigma_t^2}{\mu_t^2}$ we find that

$$\begin{aligned} N_0 &= \frac{1}{\mu_t} \\ N_1 &= N_0(\bar{n}+s^2) \\ N_2 &= N_0(\bar{n}^2+3\bar{n}s^2+3s^4) \\ N_3 &= N_0(\bar{n}^3+6\bar{n}^2s^2+15\bar{n}s^4+15s^6) \end{aligned} \tag{8.48}$$

Calculation of the moments

We now have all the tools we need to calculate the various moments. The first moment is found to be

$$\overline{X} = \frac{\mu_x}{\mu_t}T + \frac{\mu_x\sigma_t^2}{\mu_t^2} - \frac{\sigma_{xt}}{\mu_t} \tag{8.49}$$

which shows that for large T we have an average velocity $u = \frac{\mu_x}{\mu_t}$ as we would expect. The second moment turns out to be

$$\overline{(X-\overline{X})^2} = \frac{T}{\mu_t}\left(\sigma_x^2 - 2\frac{\mu_x}{\mu_t}\sigma_{xt} + \sigma_t^2\frac{\mu_x^2}{\mu_t^2}\right) + 2\frac{\mu_x^2\sigma_t^4}{\mu_t^4} - 4\frac{\mu_x\sigma_{xt}\sigma_t^2}{\mu_t^3} + (1+\rho^2)\frac{\sigma_x^2\sigma_t^2}{\mu_t^2} \tag{8.50}$$

and so, for large T we have

$$D = \frac{1}{2\mu_t}\left(\sigma_x^2 - 2\frac{\mu_x}{\mu_t}\sigma_{xt} + \sigma_t^2\frac{\mu_x^2}{\mu_t^2}\right) \tag{8.51}$$

Notice that the correlation between x and t has an effect on D which can be very significant. Finally we look at the third moment

$$\overline{(X-\overline{X})^3} = \left(\frac{3T}{\mu_t} + \frac{\sigma_t^2}{\mu_t^2}\right)\frac{\sigma_t^4}{\mu_t^4}\left(\mu_x - \rho\frac{\sigma_x}{\sigma_t}\mu_t\right)^3 \tag{8.52}$$

At large times this is proportional to T, so the distribution of X given T is not normal even though we have assumed normal distributions for X_n and T_n. However $\frac{(X-\bar{X})}{\sqrt{T}}$ does have a decreasing third moment, the rate of decrease depends on the statistics of the individual steps.

General results

The results above indicate that the probability distribution of a particle looks gaussian when the time is large enough, in the sense that the higher moments only increase linearly with time so that they become less important. There are two things which affect the time before we can say the distribution is gaussian. These are

- the number of steps must be large enough to make the assumption that X_n and T_n are distributed as a multivariate normal valid.
- the time must be large enough for the skewness of the distribution to be unimportant.

The first condition is given by (8.28) and (8.29) for both x and t, the second requires

$$|\overline{(X-\bar{X})^3}| \ll |\overline{(X-\bar{X})^2}|^{\frac{3}{2}} \tag{8.53}$$

Examples

In this section we look at some specific models for the individual steps. We start with the model we used before and then move on to more complicated models with correlations.

We use the model where all steps are the same length, l, and the time for a step has probability density function $\alpha e^{-\alpha t}$. For this model we have

$$\mu_t = \frac{1}{\alpha} \qquad \sigma_t^2 = \frac{1}{\alpha^2} \qquad \mu_{3t} = \frac{2}{\alpha^3} \qquad \mu_{4t} = \frac{9}{\alpha^4}$$

$$\mu_x = l \qquad \sigma_x^2 = 0 \qquad \mu_{3x} = 0 \qquad \mu_{4x} = 0 \tag{8.54}$$

This leads to the conditions

$$n^{\frac{1}{2}} \gg 2$$

$$n \gg 6$$

$$T^{\frac{1}{2}} \gg \frac{3}{\alpha^{\frac{1}{2}}} \tag{8.55}$$

The strictest of these is the last, requiring $n^{\frac{1}{2}} \gg 3$. We saw before that by $n=50$ the gaussian looked a good approximation, which is in agreement with this. In the limit we find that

$$D = \tfrac{1}{2}\alpha l^2 = \tfrac{1}{2}ul \tag{8.56}$$

Saffman's model

Saffman (1959,1960) proposes a model for dispersion in porous media which, for the case of interest here, has Taylor diffusion equalising the concentration over the pore width and Poussellie flow in the pores. He takes fixed length pores randomly oriented. The flow in each pore is determined by assuming a constant pressure gradient in the x-direction, so flow is proportional to $(\cos\theta)^{-1}$ where θ is the angle between the pore and the x-axis. As it stands this leads to an infinite σ_t^2 and so the Central Limit Theorem does not apply. Saffman points out that the diffusion time along a pore acts as a maximum for the time distribution, when this is taken into account a finite σ_t^2 is regained. He then has

$$\mu_t = \frac{2l}{3U} \qquad \sigma_t^2 = \frac{l^2}{U^2}\left(\tfrac{2}{3}\log\frac{3Ut_0}{l} - \tfrac{1}{3}\right)$$

$$\mu_x = \frac{2l}{3} \qquad \sigma_x^2 = \frac{l^2}{18}$$

$$\mu_y = 0 \qquad \sigma_y^2 = \frac{l^2}{4}$$

$$\mu_{3t} = \tfrac{1}{3}\frac{l^2 t_0}{U^2} \qquad \mu_{3x} = -\frac{l^3}{135}$$

$$\mu_{xt} = -\frac{l^2}{9U} \qquad \mu_{yt} = 0 \tag{8.57}$$

where l is the pore length, U is the average flow velocity, $t_0 = \dfrac{l^2}{2\kappa}$ is the time to diffuse along a pore, with κ the molecular diffusivity. In the limit we have

$$D = \tfrac{1}{3}lu\left(\log\frac{3Ut_0}{l} - \tfrac{1}{3}\right). \tag{8.58}$$

If we take l=1cm, U=10^{-5}m/s we find that we must have the number of steps satisfying $n^{\frac{1}{2}}$>>17 and a limiting value of D=6.78×10^{-8}m^2/s. If we take the larger values, more appropriate for a fracture system, l=10m, U=10^{-6}m/s we find that we must have the number of steps satisfying $n^{\frac{1}{2}}$>>500 and a limiting value of D=5.95×10^{-5}m^2/s. In each case we have assumed

$\kappa = 2\times10^{-9}\mathrm{m}^2/\mathrm{s}$. The number of steps required here is very large because of the large cut-off time t_0.

The dependence of the hydrodynamic dispersivity is a surprising result. It arises because of the way velocity is related to orientation. In a real system the fluctuations in pressure gradient would change this relationship and avoid the problem. In the next model we assume that four pores meet at an intersection, with random orientations, and that the flows are determined by the equilibrium state with the pressures at the far end of each pore satisfying the constant pressure gradient. In this way a pore perpendicular to the overall flow direction will still take flow.

The random direction model

Using the model proposed above we calculate the velocities in the pores by setting the pressure at an intersection to the average of the pressures at the far ends of the pores meeting there. These pressures are assumed to obey the constant pressure gradient. If the lengths or apertures of the pores were variable we would have to take an appropriate weighted average. The following calculation is for the two-dimensional case. If we again let U be the overall average velocity we find that the average for a pore at an angle θ with x-axis is

$$\frac{U}{a}\left(\tfrac{3}{4}\cos\theta+\tfrac{1}{8}\right) \tag{8.59}$$

where

$$a = \frac{3}{8}+\frac{1}{\pi^2} \tag{8.60}$$

The proportion of material going into any one pore is proportional to the flux, and hence to the velocity. The moments can therefore be calculated quite easily.

$$\mu_t = 0.74820\frac{l}{U} \qquad \sigma_t^2 = 0.13065\frac{l^2}{U^2}$$

$$\mu_x = 0.74820l \qquad \sigma_x^2 = 0.06520l^2$$

$$\mu_{3y} = 0.13744\frac{l^3}{U^3} \qquad \mu_{3x} = -0.52605l^3$$

$$\mu_{xt} = -0.08348\frac{l^2}{U} \qquad \sigma_y^2 = 0.37500l^2 \tag{8.61}$$

From this we find that we require $n^{\frac{1}{2}} \gg 32$ and that the limiting value of the longitudinal dispersion coefficient is $D = 0.24246lU$, with transverse component $D_T = 0.25060lU$. This constant relationship between the two coefficients is not what is found numerically, implying that there is more to hydrodynamic dispersion in a fracture network than the random walk model can predict. The large n required implies that in real systems the gaussian approximation may not be good enough.

8.4 Cut lattice model.

The results from chapter 7 that need an explanation are that the longitudinal dispersion length seems to tend to a constant as the density increases, while the transverse component tends to zero faster than the separation between fractures. As the orientation varies the tranverse coefficient changes by a factor of two while the longitudinal component varies by a factor of four. At 45° the longitudinal component is 6 times the transverse while at 0° it is 20% less.

In the work on flow through fracture networks reported in chapter 4 we found that the permeability of the networks could be predicted quite well using a cut lattice. In particular the dependence of permeability on fracture density was predicted, using an effective medium approximation to the cut lattice.

The success of this predictive tool there makes it a candidate for the prediction of dispersion coefficients. We look at the simplest case, with fractures oriented either parallel to or perpendicular to the flow direction, all with length $2l$. The fracture density is denoted by ρ. All fractures have the same aperture t. The cut lattice also has aperture t, and has separation distance d and proportion of missing links ε.

We relate the lattice parameters to the network parameters by equating the full and flowing porosities. Using the formulae for large densities we have

$$2\rho lt = 2\frac{t}{d} \tag{8.62}$$

$$2\rho lt(1-\frac{2}{\lambda}) = 2\frac{t}{d}(1-\varepsilon) \tag{8.63}$$

where $\lambda=2\rho l^2$ is the average number of intersections per fracture. Thus we are led to set

$$d = \frac{1}{\rho l} \tag{8.64}$$

$$\varepsilon = \frac{1}{\rho l^2}. \tag{8.65}$$

We note in passing that $\frac{d}{\varepsilon} = l$, which means that the average uninterrupted path is half the fracture length.

For the permeability we simply took the effective medium approximation, but dispersion is more difficult. There is no dispersion without the cut links, it is not simply a perturbation about the full lattice value. To try to get the dependence of dispersion on fracture density we might argue as follows.

Suppose that each missing link affects only those particles which would have passed through it, and that it contributes to the variance of the particle positions by an amount $d^2\sigma_X^2$. The d here is the scaling factor for different size lattices. Then the overall variance after moving a distance X across a network will be this time the number of missing links encountered. So

$$\sigma^2 = \frac{\varepsilon X}{d} \cdot d^2 \sigma_X^2 = \frac{X \sigma_X^2}{\rho^2 l^3} \tag{8.66}$$

The time taken for a particle to cross the distance X will be insensitive to the density at high densities, and so we have a dispersion coefficient

$$D \propto \frac{1}{\rho^2}. \tag{8.67}$$

Clearly the same argument applies for the transverse component. So this gives both coefficients going to zero very quickly, much more quickly than is observed in the longitudinal case, and slightly too quickly in the transverse case.

To explain this we could argue as follows. Suppose that the distance dispersed by a missing link is large, so that there is interference between links causing a cut off in the interlink distance. We must replace $d\sigma_X$ by $\frac{d\sigma_X}{\varepsilon^{\frac{1}{2}}}$, since $\frac{1}{\varepsilon^{\frac{1}{2}}}$ is the distance between missing links. If we work through the calculation we find

$$D \propto \frac{1}{\rho}. \tag{8.68}$$

Even this falls faster than the observed longitudinal component. Clearly however this type of model could explain the transverse coefficient.

We can get a constant D if we suppose that the important distance is the distance between missing links in a single direction. In that case the variance for each missing link would be $\frac{\sigma_X^2 d^2}{\varepsilon^2}$ and

$$D = \text{constant} . \tag{8.69}$$

At this time it is not clear whether the correct behaviour can be deduced from a cut lattice model or if the network results are fundamentally different.

Chapter 9 An Example of a Full Network

In this chapter we present the results of transport calculations in a full network, that is in a network which might be taken to represent the fracturing in a large region around a potential repository. The example is not intended to represent any particular site but rather to indicate how a real site might be modelled, and to discover any unforeseen problems that arise.

The transport calculations were done using a modified version of the particle following program described in chapter 7. The main modifications were

- the top boundary is not straight
- the fracture density can vary from point to point
- the fracture aperture can vary from point to point
- the particles can start from any specified positions
- the output at each position against time is recorded.

These have been implemented as follows.

The height of the top boundary is given as a function of the horizontal coordinate. This function is used in all calculations of intersections with the boundary.

The variation of fracture density is achieved by supplying a mapping function. This maps fracture centres from the specified generation region to the solution region. Any density variation can therefore be specified. Fracture sets can be mapped independently.

Fracture apertures are made to vary by specifying a multiplication factor which is a function of position. The aperture of each fracture is chosen from the original distribution and then multiplied by this factor, evaluated at the fracture centre.

The particle start points can be anywhere in the region. The nearest intersection that is not a dead end is used. For each run any number of different points can be specified, with any number of particles at each.

The particles will return to the surface at a boundary intersection. As each particle arrives the arrival intersection and time are recorded for later processing. In the example here we use this information to plot the spatial distribution of the first 10%, next 40% and final 50% of the particles.

The example used initially had a top boundary with high ground at each end and a valley between. The fracture density was higher near the surface, and the fracture aperture was also higher there. It was found that the slight variation in surface height caused large flows near the surface, so that all the particles finally emerged at or near to the lowest point. In a real system there would generally be a layer of soil or highly fractured rock at the surface which equalises pressure differences. It is the arrival at this layer that is of interest, and so the example finally used has a totally flat valley bottom.

Figure 9.1 shows the example used. The side and bottom boundaries are no-flow. There is a flow from each end to the centre, caused by the hills. Between 2400m and 25000m from the left end is a zone of wider fractures. In this zone the fracture aperture factor is constant while elsewhere it decreases with depth. Four start points are indicated, in fact for each of these the particles were started from four points at the corner of a 100m square. Full details of the problem are given below.

Region 0 to 7000 metres by −2500 to height(x) metres

$$\text{Height} = 100+300\cos\frac{\pi x}{4000} \qquad x<2000$$

$$\text{Height} = 100 \qquad 2000<x<5500$$

$$\text{Height} = 100+200\cos\pi\frac{7000-x}{3000} \qquad x>5500$$

Fracture set 1

Orientation	0°±8° to horizontal. Uniform distribution.
Half-length	mean 120m st. dev. 40m. −ve exponential.
Basic Aperture	50μm ±25μm. Uniformly distributed.
Basic Density	$10^{-4}\,m^{-2}$. Into region 7300m by 3200m.

Fracture set 2

Orientation	75°±8° to horizontal. Uniformly distributed.
Half-length	mean 120m st. dev. 25m. −ve exponential.
Basic Aperture	50μm ±25μm. Uniformly distributed
Basic Density	$8\times10^{-5}\,m^{-2}$. Into region 7300m by 3200m.
Fracture mapping.	x unaltered, $y'=550-2000a+1200a^2$ where $a=\frac{550-y}{3200}$.

Aperture factor. 1 if $2400<x<2500$ or $y>0$. Otherwise $\frac{400}{400-y}$.

For the particular realisation used here there were 3489 fractures, with 8758 intersections after dead-ends had been removed.

Four start positions were used. The first run started 2500 particles at (1000,-500), (1000,-600), (1100,-500) and (-1100,-600). The other runs also started particles in a 100m square, the top left corner being at (4000,-500), (1000,-1000) and (4000,-1000).

For each run the arrival curve against time was plotted. These are shown in figures 9.2 to 9.5. In the first run particles arrive very quickly, after just two years, with 90% arriving by 15 years. This is because the flow is to the fracture zone and then up to the surface. In the other cases the particles take much longer to reach the surface. In case 2 this is because the start points are not well connected to the surface, and in the other cases because of the deeper start points. It seems that for case 3 there is no route to the surface via the fracture zone, presumably because it is not well enough connected to take flow from -1000m to the surface. Case 4 takes only twice as long as case three despite the reduced fracture density and aperture at depth, the start points must be in a better connected zone than the average for that depth.

The positions at which the particles arrive are shown in figures 9.6 to 9.9. The arrival positions for the first 10%, the next 40% and the final 50% are shown. The distances are the percentage distance across the region, the fracture zone is therefore 34 to 35. It seems that no particles arrive directly from the fracture zone, but the aperture increase is for fractures centred in the zone so there will be wider fractures for a few hundred metres either side of it.

As we would expect, the positions where particles first arrive are generally the positions where most particles arrive in all; although for case 3 arrival position 43 takes none of the first 10% and yet takes 36% of the total, while the three intervals taking 99.5% of the initial arrivals take just 4% of the second half arrivals.

We note that in all cases there is very little lateral spreading of the particles.

In general then we have shown that transport through large fracture systems can be calculated, with the system parameters tailored to the site in question. An indication of arrival positions can be gained. For the particular case used here there is little lateral spreading of the particles. In general the initial arrival points indicate where the most will arrive, with a notable exception in case 3.

Chapter 10 Network Models in Three Dimensions

10.1 Introduction

In this chapter we collect together some ideas on the extension of network models to three dimensions.

In a real fracture system fractures are nearly planar openings in a three dimensional rock mass. The shape of the fractures in their plane can vary, they may have variable apertures, and channelling may occur. Even when we simplify this system and consider only planar parallel sided fractures, rectangular in shape, modelling is very difficult. Finding how such a system of fractures intersect does not present any great problems, it has been done for very large systems in order to look at connectivity, see chapter 3. Once a flow field has been calculated, finding the paths of particles by a particle following method would not be very different to the two dimensional case and could be handled without much difficulty. The problem is finding the flow field. In two dimensions this required simply solving a set of conservation equations, one for each intersection, with pressure specified on the boundary of some region. In three dimensions the fracture intersections are line segments, and the fractures between them are two dimensional planes where complicated flows can take place. It is not simple to relate pressure at intersections to fluxes and the two dimensional technique cannot be directly extended.

Let us examine what equations we need to satisfy.

(i) At each intersection there must be conservation of mass. This might apply point by point or for the intersection as a whole if there is flow down the intersection.

(ii) Within each fracture plane we must satisfy the Navier–Stokes equations, which for our case of very slow flow leads to a linear relationship between pressure and flow.

(iii) Pressure must be continuous everywhere.

10.2 Pressure formulation

We could take pressure as the basic variable, just as we did in two dimensions. We assume that the head losses at intersections can be ignored so that each point along an intersection has a unique pressure. This pressure is then discretised, by finite elements say, so that the variation along the intersections is represented by a small number of nodal values. We could allow flow along the intersection, or not, as appropriate. If we assume no flow along the intersection we proceed as follows. Within each fracture we calculate the velocity field as a function of the nodal pressures. This gives the flux into or out of each point along each intersection. From these we can formulate a conservation equation for each intersection. The simplest way to do this would be to look at the fluxes at the nodes. It is better to take the flux along each intersection weighted by each basis function. This is because it gives true mass conservation, since the sum of all basis functions on an intersection is unity, and because it leads to a symmetric system of equations as we shall see later.

The important thing that makes the method simple to implement is that the velocity and hence the fluxes are linear combinations of the nodal pressure values. We write $f_{rs}^{(k)}$ for the integrated flux times the rth basis function when the pressure is unity at node s and zero at the other nodes, that is the pressure is equal to the sth basis function. Here r and s are both nodes on the same fracture. From this we can see that the flux into the intersection times the rth basis function when the nodal pressures are P_s is given by

$$\sum_s f_{rs}^{(k)} P_s \tag{10.1}$$

for fracture k. This leads to an overall set of equations for conservation

$$\sum_s F_{rs} P_s = 0 \text{ for all } r \tag{10.2}$$

where

$$F_{rs} = \sum_k f_{rs}^{(k)}. \tag{10.3}$$

It is not immediately clear from this that F_{rs} is symmetric. We shall prove that each $f_{rs}^{(k)}$ is symmetric for a wide class of fracture shapes, from which it follows that F_{rs} is also symmetric. The example of section 10.4 will show the symmetry for one particular case.

We have a number of lines in a region bounded by some no-flow boundary C. Each intersection

has a number of nodes, with each node we associate some basis function. These basis functions are defined only along the lines. Usually they are piecewise polynomials which take value one at one node and zero at other nodes, but this is not relevant for our proof. We shall write $\Phi_i(\mathbf{l})$ for the ith basis function at the point $\mathbf{l}$ on the lines. The pressure along the lines is denoted $P(\mathbf{l})$ and the flux into the line $\gamma(\mathbf{l})$. These are related by a Green's function $G(\mathbf{l},\mathbf{l}')$ through the equation

$$P(\mathbf{l}) = \int_{\mathbf{l}'} G(\mathbf{l},\mathbf{l}')\gamma(\mathbf{l}')d\mathbf{l}' \tag{10.4}$$

where the integral is along the intersections. Here $G(\mathbf{l},\mathbf{l}')$ is the pressure at $\mathbf{l}$ for a unit sink at $\mathbf{l}'$ with a matching unit source at some other fixed point, subject to no-flow boundary conditions on the curve C.

If $P(\mathbf{l}) = \Phi_i(\mathbf{l})$ corresponds to a flux $\gamma_i(\mathbf{l}')$ we have

$$\Phi_i(\mathbf{l}) = \int_{\mathbf{l}'} G(\mathbf{l},\mathbf{l}')\gamma_i(\mathbf{l}')d\mathbf{l}'. \tag{10.5}$$

Our definition of f_{ij} is

$$f_{ij} = \int_{\mathbf{l}} \Phi_i(\mathbf{l})\gamma_j(\mathbf{l})d\mathbf{l}. \tag{10.6}$$

Substituting (10.5) into (10.6) we get

$$f_{ij} = \int_{\mathbf{l}} d\mathbf{l} \int_{\mathbf{l}'} d\mathbf{l}' G(\mathbf{l},\mathbf{l}')\gamma_i(\mathbf{l}')\gamma_j(\mathbf{l}). \tag{10.7}$$

Therefore in order to show that $f_{ij}=f_{ji}$ we need to show that $G(\mathbf{l},\mathbf{l}')=G(\mathbf{l}',\mathbf{l})$. In order to do this we will use the complex potential and conformal mappings.

If the region bounded by the curve C can be conformally mapped onto the upper half-plane, with the curve C going to the real axis, then the result follows from the following argument.

Let us have a point sink at $\mathbf{a}$ with a corresponding point source at infinity. Then the complex potential at $\mathbf{z}$ is given by

$$-\frac{1}{2\pi}(\log \mathbf{z}-\mathbf{a} \;+\; \log \mathbf{z}-\bar{\mathbf{a}}). \tag{10.8}$$

The second term is from the image giving no flow across the real axis. The pressure is the real part of this, and is unchanged by switching $\mathbf{a}$ and $\mathbf{z}$, since the real part of the logarithm is unchanged if the argument changes sign or is conjugated.

So for this case we have the required result. When we do a conformal mapping the source at infinity will be mapped to a point on the boundary C. In all cases the total flux into the lines will be zero so the strength of this source will be zero.

It is a consequence of the Reimann Mapping Theorem (Nevanlinna and Paatero,1964) that any region bounded by a piecewise analytic Jordan curve can be mapped conformally onto the half plane, with the boundary being mapped continuously. The fracture matrix will therefore be symmetric for all likely fracture shapes.

The symmetry of F_{rs} means that (10.2) can be solved more quickly, and can be stored more efficiently. The solver used in the two-dimensional system could also be used here. This type of matrix equation is well known in finite-element analysis. Effectively each fracture is acting as a finite element and the $f_{rs}^{(k)}$ matrices are the element matrices which are assembled to give F_{rs}. If there are a large number of nodes in total it may be sensible to use a frontal solver. This does not assemble the full matrix at once, rather it brings in the element (or fracture) matrices only when they are needed and eliminates variables once they are fully summed, that is once all fractures on which occur have been included.

With this formulation we can include fixed pressure boundaries simply be replacing the corresponding equation by the assignment to the required value. Specified fluxes can also be included quite simply, by adding a term to the right hand side of the equations.

If flow along the intersections is to be included then $f_{rs}^{(k)}$ would be modified. Care would have to be taken not to double count the effects of the intersection by including it in both fractures.

The fracture matrices can be calculated in any way, without modification to the overall method. This allows the inclusion of the different fracture characteristics with little additional effort. The fracture matrices could be approximated crudely or calculated accurately with, say, a finite element scheme in each fracture. A library of matrices could be formed to allow quick calculations to be made. Even for approximate methods the fracture matrix should be made symmetric. Also the overall conservation requires

$$\sum_r f_{rs}^{(k)} = 0 \text{ for all } k. \tag{10.8}$$

Note that the symmetric relationship

$$\sum_s f_{rs}^{(k)} = 0 \text{ for all } k \tag{10.9}$$

also has a physical interpretation. It says that there is no flow if all the nodal pressures are equal.

10.3 Flux formulation

We could use the fluxes at the intersections as the basic variables. The advantage of doing this is that the analytic solutions within fractures are easier to obtain in terms of fluxes. However it would be impossible to specify pressure boundary conditions. We feel that this would be too big a handicap and will therefore not pursue this method further.

10.4 An example of a fracture matrix

To show one way in which the fracture matrix could be calculated we have used the finite element program NAMMU (Rae and Robinson. 1979) to calculate it for a simple case. We take a square fracture. 40m by 40m. with two intersections. Taking one corner of the fracture at the origin these run from (10.10) to (10.25) and from (25.20) to (25.30). The pressure is discretised by linear functions. giving two nodes on each fracture which are numbered as follows. Node 1 is at(10.10) with node 2 at (10.25) and node 3 is at (25.20) with node 4 at (25.30).

For flow between two parallel planes we can use the porous medium program with permeability replaced by a transmissivity equal to $\frac{h^2}{24}$, where h is the fracture aperture. The flux is given by h times the calculated Darcy velocity. We have taken the factor $\frac{h^3}{24\mu}$ out of the fracture matrix in presenting the results.

The pressure contours for each of the four cases are shown in figure 10.1. The resulting fracture matrix was

	P=1 at node 1	P=1 at node 2	P=1 at node 3	P=1 at node 4
Flux for node 1	-1.0311	0.3527	0.4249	0.2535
Flux for node 2	0.3528	-1.2389	0.4293	0.4569
Flux for node 3	0.4244	0.4290	-1.2718	0.4184
Flux for node 4	0.2534	0.4569	0.4183	-1.1286

The slight lack of symmetry here is due to the approximate nature of the finite element method. The row sums are all very small, because when the nodal pressures are all the same there is no flow in the finite element problem. The column sums are less good, because of discretisation errors from the finite element grid.

Chapter 11 Including Other Transport Phenomena

The models used in this work have looked simply at convective transport of contaminant in fracture networks. There are other important phenomena to be considered and the ways that these might be included are discussed in this chapter. The chapter is in three parts. In the first we give a description of the phenomena that we wish to look at, in the second the extension of the current models to include some of these is discussed, and finally, in the third section, we describe a different method which has the ability to model a wide range of phenomena.

11.1 Transport phenomena in networks

The models used earlier deal with transport of contaminant by convection. Within each fracture we might also wish to include

- molecular diffusion or dispersion
- sorption (equilibrium or kinetic)
- matrix diffusion
- radioactive decay (single species or chains).

Each of these is discussed in turn. Throughout we use C to denote number of atoms per unit volume of water.

Convection

Contaminant is simply carried along with the flow. The governing equation is

$$\frac{\partial C}{\partial t} + u\frac{\partial C}{\partial x} = 0 \tag{11.1}$$

where u is the flow velocity.

Molecular diffusion or dispersion

We include here any mechanism which acts diffusively in the fracture. With convection the governing equation is

$$\frac{\partial C}{\partial t} + u\frac{\partial C}{\partial x} = D\frac{\partial^2 C}{\partial x^2} \tag{11.2}$$

where D is the diffusion coefficient.

Sorption

Sorption is the process by which contaminant becomes chemically attached to the fracture walls. The equation used depends on the rate of the chemical processes. If they are fast we use equilibrium sorption, otherwise we use kinetic sorption. For equilibrium sorption there is a constant ratio between the amount sorbed and the amount in the flow, while for kinetic sorption the transfer rates are included in the equations. In each case S denotes the number of atoms sorbed per unit area of wall. In either case we have

$$\frac{\partial C}{\partial t} + u\frac{\partial C}{\partial x} = -\frac{1}{b}\frac{\partial S}{\partial t} \tag{11.3}$$

where $2b$ is the fracture aperture. The equation for sorption is

$$\frac{\partial S}{\partial t} = bk_s C - k_r S \tag{11.4}$$

where k_s and k_r are the rates for sorption and desorption. If the rates are fast we have $S = \frac{bk_s}{k_r}C$.

We then write $R = 1 + \frac{k_s}{k_r}$. R is the retardation factor, and (11.3) and (11.4) are replaced by

$$R\frac{\partial C}{\partial t} + u\frac{\partial C}{\partial x} = 0. \tag{11.5}$$

Matrix diffusion

The fracture walls are not quite impermeable. Some contaminant will diffuse into the pores in the walls, slowing up the transport. We model this by introducing C_p, the concentration in the pores, which is a function of position in fracture, time and distance into the rock, w. In the fracture we have convection with a source from the walls (Lever et al.1982, Lever and Bradbury.1983)

$$R\frac{\partial C}{\partial t} + u\frac{\partial C}{\partial x} = \frac{D_t}{b}\frac{\partial C_p}{\partial w}\bigg|_{w=0} \tag{11.6}$$

and in the rock we have diffusion

$$\alpha_P \frac{\partial C_P}{\partial t} = D_i \frac{\partial^2 C_P}{\partial w^2} \tag{11.7}$$

where D_i is the intrinsic rock diffusion coefficient and α_P is the rock capacity factor, which may include a factor for equilibrium sorption in the rock matrix.

Radioactive decay

If we are concerned solely with the decay of a single species then we have simply

$$\frac{\partial C}{\partial t} + u\frac{\partial C}{\partial x} = -\lambda C \tag{11.8}$$

where λ is the decay constant.

If a chain is to be modelled then we have

$$\frac{\partial C_i}{\partial t} + u\frac{\partial C_i}{\partial x} = -\lambda_i C_i + \lambda_{i-1} C_{i-1} \tag{11.9}$$

where C_i is the concentration of the ith species in the chain and λ_i is the corresponding decay constant. For the first member of the chain the $\lambda_{i-1} C_{i-1}$ term is not present.

Boundary conditions

For each case we must have the appropriate boundary conditions. For first order equations we will require the concentration at one end. For second order equations the concentration at both ends, or concentration and its first derivative at one end is required. For the matrix diffusion equation (11.7) we can either have no diffusion beyond some set distance into the rock, or allow diffusion to infinity with zero concentration at infinity.

Other time-dependent effects

In certain circumstances the parameters of the networks might be time-dependent. For example fractures may close-up as they are mineralised, or they may open up if a pumping test is done. If the waste is emitting heat then the viscosity may change, as well as sorption constants.

11.2 Extension of current models

The inclusion of equilibrium sorption and radioactive decay for a single species presents no problems for any model. Equilibrium sorption leads to a scaling of the flow velocity by the retardation factor. Radioactive decay can be ignored until the end when all concentrations can be reduced by the appropriate amount.

Kinetic sorption could be added to the mass-lumping method by introducing a second mass for each section, to represent the mass of contaminant on the wall. Mass could then be transferred between the two compartments on each timestep as required by (11.4).

Matrix diffusion could be included in a similar way, except that more than one extra mass would be required for each section, representing the mass at various distances into the rock.

Decay chains could be added to mass-lumping or particle following. If sorption is also to be included with different retardations for the different nuclides then the particle following method cannot be used.

Molecular diffusion or sorption could be included in the mass-lumping method by transferring mass to adjacent sections on each step. It could also be included in the particle following method, by introducing a random component into the travel times for each link.

Other time-dependent effects come into two categories, those which modify the flow, and those which affect only the transport parameters. If the flow is affected then the flow equations must be re-solved from time to time. This will cause problems for both mass-lumping and particle following, requiring major modifications in both methods. If only transport parameters are changing then both methods, if applicable to the fixed parameter case, could be modified quite simply to cope.

11.3 Modelling network transport using Laplace transforms

For many of the phenomena of interest we can write down a linear partial differential equation governing the transport of contaminant in a single fracture. Analytic solutions can be obtained, in many cases by using a Laplace transform. In general these solutions are complicated, requiring significant computational effort to evaluate. Moreover any attempt to chain together such solutions quickly becomes impractical. The technique proposed here inverts the Laplace transforms numerically, and can be used to find the solution for a single fracture or for a network of fractures.

The method described below is for cases with no second order terms in the fracture transport equation, that is no diffusion in the fracture. This restriction means that the concentration value against time at one end of a fracture is sufficient to give the full solution.

Description of the network.

We assume here that the flow through the network has been calculated, either by the program described earlier or in some other way. A network can be described in terms of its intersections and the links between them. Some intersections will be linked to external sources or sinks. In general, the majority of intersections will be internal, receiving contaminant from from other 'upstream' intersections, mixing it and passing it on to the next 'downstream' intersections. The links through which the contaminant moves from intersection to intersection will have certain properties which are basically the coefficients of the differential equation governing transport. For the purposes of this section it is convenient to regard the water flow rate as a property, since it is known. The other properties will include length, aperture, sorption coefficient, rock matrix diffusion coefficients, etc. There may be some global properties, such as decay rates, but these can all be included for each link. The network is fully described by the list of source intersections, the list of next downstream intersections for each intersection, the properties of each link, and the list of output intersections.

Given the network description and the contaminant concentrations against time at the input intersections we wish to find the contaminant concentration against time at the output intersections.

The transformed problem

The method we use is as follows. Instead of using concentration against time we use the Laplace transform of this. This makes the problem tractable because the Laplace transform of concentration at the downstream end of a link is given by the Laplace transform at the upstream end times a transfer function. This transfer function depends on the properties of the link, but not on the concentrations. If we write $C_i^*(s)$ for the transform of the concentration at intersection i then we have

$$C_i^*(s) = \sum_{j=1} T_{ij}(s) C_j^*(s) \tag{11.10}$$

where $T_{ij}(s)$ is the transfer function for the link from j to i and is zero unless i is at the downstream end of a link from j. If we let $T_{ii}(s) = 1$ we can write

$$\sum_j T_{ij}(s) C_j^*(s) = 0 \qquad \text{for all } i. \tag{11.11}$$

The transfer functions here include the factor to take account of mixing.

The problem can now be solved as follows. We start with the transformed concentration, C^*, at each source intersection. Then we simply cycle round, each time calculating C^* for every intersection whose immediate upstream predecessors have been dealt with. Eventually we will have got the transform for every intersection and in particular for the output intersections. We now invert the transforms to find the concentration against time at the intersection of interest.

There are three things we need to know: the input transforms, the transfer functions, and how to invert the transforms.

Input Transforms

Any function could be used for the input but normally the input would be one of the following

Delta-function

$$C(t) = C_0 \delta(t - t_0)$$

$$C^*(s) = C_0 e^{-st_0} \tag{11.12}$$

Step-function

$$C(t) = 0 \quad \text{for} \quad t < t_0$$

$$C(t) = C_0 \quad \text{for} \quad t > t_0$$

$$C^*(s) = C_0 \frac{e^{-st_0}}{s} \tag{11.13}$$

Decaying radioactive source $\quad C(t) = 0 \quad \text{for} \quad t < t_0$

$$C(t) = C_0 e^{-\lambda t} \quad \text{for} \quad t > t_0$$

$$C^*(s) = C_0 \frac{e^{-st_0}}{s+\lambda} \tag{11.14}$$

Finite length pulse

$$C(t) = 0 \quad \text{for} \quad t < t_0 \quad \text{or} \quad t > t_1$$

$$C(t) = C_0 \quad \text{for} \quad t_0 < t < t_1$$

$$C^*(s) = C_0 \frac{\left(e^{-st_0} - e^{-st_1}\right)}{s} \tag{11.15}$$

Fracture Transfer Functions

We give examples for the cases listed in section 11.1. In all cases we denote the fracture length by l.

(1) Pure convection

For pure convection the governing equation is (11.1) and the corresponding transfer function is

$$T(s) = e^{-\frac{l}{u}s} \tag{11.16}$$

(2) Convection with equilibrium sorption and matrix diffusion

In this case the governing equation in the fracture is (11.6), with an additional retardation factor, R, multiplying the $\frac{\partial C}{\partial t}$ term. The equation for the rock is (11.7). We take the rock boundary condition to be zero at infinity. The transfer function is then

$$T(s) = e^{-\frac{l}{u}\alpha}$$

$$\alpha = sR + s^{\frac{1}{2}} \frac{(\alpha_p D_i)^{\frac{1}{2}}}{b} \tag{11.17}$$

(3) Two radionuclides in a chain with different retardations

In this case the equations are (11.9) with the addition of retardations, R_1 and R_2.

$$\begin{aligned} R_2 \frac{\partial C_2}{\partial t} + u \frac{\partial C_2}{\partial x} &= \lambda_1 R_1 C_1 - \lambda_2 R_2 C_2 \\ R_1 \frac{\partial C_1}{\partial t} + u \frac{\partial C_1}{\partial x} &= -\lambda_1 R_1 C_1 \end{aligned} \tag{11.18}$$

Instead of a single transfer function we have a two by two array relating the output transforms to the input by

$$\begin{aligned} C^*_{1\,out}(s) &= T_{11}(s)C^*_{1\,in}(s) + T_{12}(s)C^*_{2\,in}(s) \\ C^*_{2\,out}(s) &= T_{21}(s)C^*_{1\,in}(s) + T_{22}(s)C^*_{2\,in}(s) \end{aligned} \tag{11.19}$$

Since the output of nuclide 2 does not depend on the input of nuclide 1 $T_{12}(s)=0$. The other values are

$$\begin{aligned} T_{11}(s) &= e^{-\frac{l}{u}\alpha} \\ T_{22}(s) &= e^{-\frac{l}{u}\beta} \\ T_{21}(s) &= \frac{\lambda_1 R_1}{\beta-\alpha}\left(e^{-\frac{l}{u}\alpha} - e^{-\frac{l}{u}\beta}\right) \end{aligned} \tag{11.20}$$

where $\alpha=(s+\lambda_1)R_1$ and $\beta=(s+\lambda_2)R_2$.

Inversion of the Laplace transform

The inversion formula for Laplace transforms is

$$f(t) = \frac{1}{2\pi i}\int_C e^{st} f^*(s)\,ds \tag{11.21}$$

where C is a contour in the complex plane which runs to the right of all singularities of $f^*(s)$. The contour used analytically is the Bromwich contour running from $a-i\infty$ to $a+i\infty$ where a is large enough to satisfy the condition on singularities. Numerically this contour is no use. The integrand oscillates and large errors are introduced. The curve C should be chosen to minimise the oscillations. Talbot (1979) proposed a method which uses the best curve for one particular transform and applies it to all transforms. This works well in many cases and has been used to invert some single fracture transforms (Lever et al. 1982. Hodgkinson and Lever. 1982. Hodgkinson et al. 1983). Unfortunately one class of problem that it cannot deal with is where there is a discontinuity in the solution. In this case the method cannot be used for times before the discontinuity. since the integrand of (11.20) does not go to zero at the ends of the contour C. For a network the solution will have many discontinuites. corresponding to the differing path lengths.

and so the method does not work. It may be that similar methods could be developed that would be able to deal with this case.

The hope is that a method can be found which gives the original function at any time from a small number of values of the transform. These values could be found in the way outlined in section 11.2. Until such a method is found this technique cannot be used.

Chapter 12 Summary and Conclusions

It is important that radioactive waste is disposed of in a safe and reliable fashion. When considering disposal underground the possibility of groundwater carrying waste back to the surface must be considered. Modelling this process has generally been done using continuum models, but for fractured rock it is not clear that these are valid. If they are valid then the parameters for them must be found.

This study has looked at various aspects of flow through fractured rock. Its purpose was to develop a better understanding of the processes that occur in fracture systems. Statistical fracture networks were used to do this. In these the fracture properties are specified by probability distributions. Realisations of these distributions are generated and analysed numerically. Averages and variabilities between realisations have been found and the effect of varying the statistical properties assessed.

The study was in three main sections: connectivity, flow and transport.

The connectivity of fracture networks is closely related to percolation theory. The work, described in chapter 3, concentrated on finding critical densities for various systems. In order to find these a computer program was developed to run on the CRAY computer at Harwell. The general program can deal with all distributions of orientation and length. A more specialised program was developed from this to deal with the case of fixed length, orthogonal systems. This can analyse systems of 250,000 fractures in under 8 seconds.

As a result of these studies it has been found that the critical density of networks varies with the network size used to calculate them. By using finite-size scaling arguments the asymptotic critical density can be deduced. It has been discovered that the average number of intersections for each fracture at percolation is insensitive to the fracture statistics. In two dimensions the value is between 3.1 and 3.7 while in three dimensions values of 2.0 and 2.5 have been found. For cases where fracture length varies the average number of intersections is taken as a weighted average with weights proportional to the fracture length.

A simple argument was presented to relate the critical densities in networks to the critical probabilities in lattices. The predictions that this makes agree well with the numerical results.

In chapter 4 we looked at the flow of water through fracture networks. This was done by using another computer program. The techniques used in the connectivity program proved invaluable

for finding the intersections in large networks. The matrix equations for pressure at the intersections were solved using a specially developed variable bandwidth solver.

By calculating the effective permeability of many realisations of the fracture statistics the average permeabilities and their variabilities were found. The permeability depends on the size of the network, which implies that small scale experiments may be misleading. The network size has to be at least 10 fracture lengths for the variability in permeability to be less than 10% of the mean.

The dependence of permeability on fracture density, length variability and aperture variability was investigated. It was found that the variation with density could be predicted by a cut lattice model, which also gave an indication of the permeability variation with spread of fracture length and with network size. The permeability change with aperture spread was more difficult to predict. It depends on the fracture density, because at low density the flow is predominantly along chains of fractures while at high densities there are many interconnected paths.

The transport of radionuclides in the groundwater is of most importance to radioactive waste disposal. In this study we concentrated on the transport by convection in the flow with mixing at the intersections giving hydrodynamic dispersion. Two computer programs were developed from the flow program. One of these, the mass-lumping program described in chapter 6, was designed to be extendable to include other processes such as rock matrix diffusion and sorption. The other, the particle following program described in chapter 7, is specifically for convection and mixing. It is fast, enabling many realisations to be used, with large numbers of particles in each.

Most of the work on transport was in the system with two orthogonal fracture sets, with fixed length and fixed aperture fractures. The effect of changing the fracture density and network size was investigated. In chapter 5 we derived a number of different ways of getting the continuum parameters from the particle arrival time data. The discrepancies found between the parameters derived in the different ways shows that dispersion in networks is not fully diffusion-like. The discrepancies were found to persist when fracture density and network size were increased. The origin of this discrepancy is the long tail of the arrival times, caused by some particles passing through fractures with very little, and hence very slow, flow.

The average particle velocity was found to be related to the Darcy velocity by the flowing porosity, as calculated from geometrical considerations.

The longitudinal dispersion coefficient was found to tend to a constant as fracture density increased, while the transverse component tended to zero surprisingly quickly.

Some models of hydrodynamic dispersion were looked at in chapter 8. Random walk models were studied and some general results obtained. These were applied to some particular cases. These models were unable to predict the observed behaviour. The cut lattice model, which had successfully predicted permeabilities, was considered. Some arguments which might explain the observed behaviour were put forward. The numerical results are still not understood.

In chapter 9 the particle following method was generalised to handle a network model of a large region surrounding a potential repository. This indicated the sort of results that could be obtained and the problems that arise.

In chapter 10 the extension of the methods to three dimensions was discussed. It was snown that the fractures could be thought of a elements in a finite-element problem, with fracture matrices being assembled to form the overall matrix equation for the pressures. One such fracture matrix was evaluated.

In chapter 11 the inclusion of other phenomena was discussed. Extensions to the existing models were considered and a new method based on Laplace transforms was proposed.

In conclusion, this work has shown that connectivity and permeability of fracture networks can be understood in terms of quite simple models, enabling critical densities and permeabilities to be estimated. Dispersion is much more complicated, even predicting the dependence on fracture density could not be done. At the same time the results have shown that interpreting experimental results in terms of a diffusion equation will give misleading values for the parameters. It is clear that a better understanding of hydrodynamic dispersion in fracture networks is still required.

References

Atkinson.R. et al (1984) 'Review of the Groundwater Flow and Radionuclide Transport Modelling in KBS-3' Harwell Report AERE-R 11140

Balberg.I.. Binenbaum.N. (1983) 'Computer Study of the Percolation Threshold in a Two-dimensional Anistropic System of Conducting Sticks' Physical Review B Vol 28(7) p3799

Bear.J. (1972) 'Dynamics of Flow through Porous Media'. American Elsevier

Beran.M.J. (1968) 'Statistical Continuum Theories' p283–288. Interscience

Bourke.P.J.. Bromley.A.. Rae.J.. Sincock.K. (1981) 'A Multi-Packer Technique for Investigating Resistance to Flow through Fractured Rock' Proceedings of the NEA Workshop on Siting Radioactive Waste Repositories in Geological Formations. Paris. p173

Bourke.P.J.. Evans.G.V.. Hodgkinson.D.P.. Ivanovich.M. (1982) 'An Approach to Water Flow and Radionuclide Transort through Fractured Rock' Proceedings of the NEA Workshop on the Investigation of Rock for Burial of Radioactive Waste. Ottawa

Bourke.P.J.. Durrance.E.. Heath.M.J.. Hodgkinson.D.P. (1984) 'Water Flow and Radionuclide Transort through Fractured Rock' AERE Report (in preparation)

Brace.W.F. (1980) 'Permeability of Crystalline and Argillaceous Rocks' Int. J. Rock Mech. Min. Sci. & Geomech. Abstr. Vol.17 p241

Broadbent.S.R.. Hammersley.J.M. (1957) 'Percolation Processes. I. Crystals and Mazes' Proc. Camb. Phil. Soc.. Vol. 53. p629

Caldwell.I.A. (1972) 'The Theoretical Determination of the Permeability Tensor for Jointed Rock' Symposium on Flow through Fissured Rock. Stuttgart

Castillo.E. (1972) 'Mathematical Model for Two-Dimensional Percolation through Fissured Rock' Symposium on Flow through Fissured Rock. Stuttgart

Coats.K.H.. Smith.B.D. (1964) 'Dead End Pore Volume and Dispersion in Porous Media' Soc. Petro. Eng. Vol. 4(1) p73

Cuthil.E.. McKee J. (1969) 'Reducing the Bandwidth of Sparse Symmetric Matrices' Proc. 24th Nat. Conf. Assoc. Comput. Mach. ACM Publ P-69. New York

Darcy,H. (1856) 'Les Fontaines Publiques de la Ville de Dijon' Dalmont, Paris

Dolman,E.A., Robinson,P.C. (1983) 'NAMSOL: Finite Element Program for Migration of Radionuclides in Groundwater' Harwell Report AERE-R 10882

Essam,J.W. (1980) 'Percolation Theory' Reports of Progress in Physics, Vol.43, p833

Fisher,M.E. (1971) in 'Critical Phenomena' ed. M.S. Green, Academic, London

Fried,J.J., Combarnous,M.A. (1971) in 'Advances in Hydroscience, Volume 7' ed. V.T. Chow, Academic, London

Heath, M.J. (1983) 'Geological Control of Fracture Permeability in the Carmmenellis Granite, Cornwall' meeting on Mineralogical Aspects of the Disposal of Toxic Wastes, London

Heath,M.J, Durrance,E. (1984) 'Hydrogeological Measurements in Cornish Granite' AERE Report (in preparation)

Hodgkinson,D.P., Lever,D.A. (1982) 'Interpretation of a Field Experiment on the Transort of Sorbed and Non-sorbed Tracers through a Fracture in Crystalline Rock' Harwell Report AERE-R 10702

Hodgkinson,D.P., Lever,D.A., England,T.H. (1983) 'Mathematical Modelling of Radionuclide Transport through Fractured Rock using Numerical Inversion of Laplace Transforms: Application to INTRACOIN Level 3' Harwell Report AERE-R 10986

Hodgkinson,D.P. (1984) 'Analysis of Steady-state Hydraulic Tests in Fractured Rock' Harwell Report AERE-R 11287

Jackson,C.P., Robinson,P.C. (1982) 'A Numerical Study of Various Algorithms Related to the Preconditioned Conjugate Gradient Method' Harwell Report TP 949 (submitted to Int. J. Num. Methods in Eng.)

KBS (1983) 'Final Storage of Spent Nuclear Fuel – KBS-3. II. Geology' KBS, Swedish Nuclear Fuel Supply Company

Kirkpatrick,S. (1971) 'Classical Transport in Disordered Media: Scaling and Effective-Medium Theories' Physical Review Letters Vol. 27(25) p1722

Koplik,J. (1981) 'On the Effective Medium Theory of Random Linear Networks' J. Phys. C, Vol. 14, p4821

Koplik.C.M., Kaplan.M.F., Ross.B. (1982) 'The Safety of Repositories for Highly Radioactive Wastes' Reviews of Modern Physics, Vol.54(1) p269

Krizek.R.J., Karadi.G.M., Socias.E. (1972) 'Dispersion of a Contaminant in Fissured Rock' Symposium on Flow through Fissured Rock. Stuttgart

Landauer.R. (1952) 'The Electrical Resistance of Binary Metallic Mixtures' Journal of Applied Physics, Vol.23(7), p779

Last.B.J., Thouless.D.J. (1979) 'Percolation Theory and Electrical Conductivity' Physical Review Letters Vol.27(25) p1719

Lever.D.A., Bradbury.M.H., Hemingway.S.J. (1982) 'Modelling the Effect of Diffusion into the Rock Matrix on Radionuclide Migration' Harwell Report AERE-R 10614

Lever.D.A., Bradbury.M.H. (1983) 'Rock-matrix Diffusion and its Implications for Radionuclide Migration' meeting on Mineralogical Aspects of the Disposal of Toxic Wastes, London

Long.J.C.S., Remer.J., Wilson.C., Witherspoon.P.A. (1982) 'Porous Media Equivalent for a Network of Discontinuous Fractures' Water Resources Research Vol.18(3) p645

Long.J.C.S. (1983) Investigation of Equivalent Porous Medium Permeability in Networks of Discontinuous Fractures' Ph. D. Thesis, University of California

McEwen.T.J Lintern.B.C. (1980) 'Fracture Analysis of The Rocks of the Altnabraec Area' Institute of Geological Sciences Report ENPU 80-8

Nevanlinna.R. and Paatero.V. (1964) 'Introduction to Complex Analysis' Addison-Wesley

Pike.G.E., Seager.C.H. (1974) 'Percolation and Conductivity: A Computer Study' Physical Review B, Vol.10(4), p1421

Rae.J., Robinson.P.C. (1979) 'NAMMU: Finite Element Program for Coupled Heat and Groundwater Flow' Harwell Report AERE-R 9610

Rae.J., Robinson.P.C., Wickens.L.M. (1981) 'A User's Guide for the Program NAMMU: I. General Information' Harwell Report AERE-R 10120

Rae.J., Robinson.P.C., Wickens.L.M. (1983) 'Coupled Heat and Groundwater Flow in Porous Rock' Numerical Methods in Heat Transfer Volume II, ed. R.W. Lewis, John Wiley

Saffman.P.G. (1959) 'A Theory of Dispersion in a Porous Medium' Journal of Fluid Mechanics, Vol. 6 p321

Saffman.P.G. (1960) 'Dispersion due to Molecular Diffusion and Macroscopic Mixing in Flow through a Network of Capillaries' Journal of Fluid Mechanics. Vol. 7 p194

Scheidegger.A.E. (1954) 'Statistical Hydrodynamics in Porous Media' Journal of Applied Physics. Vol. 25(8) p994

Scheidegger.A.E. (1972) 'The Physics of Flow through Porous Media' University of Toronto

Schwartz.F.W. Smith.L., Crowe.A.S. (1983) 'A Stochastic Analysis of Macroscopic Dispersion in Fractured Media' Water Resources Research. Vol.19. p1253

Shankland.T.J., Waff.H.S. (1974) 'Conductivity in Fluid–Bearing Rocks' Journal of Geophysical Research. Vol.79(32). p4863

Shante.V.K.S., Kirkpatrick.S. (1971) 'An Introduction to Percolation Theory' Advances in Physics. Vol.20. p325

Simmons.C.S. (1982) 'A Stochastic–Convective Transport Representation of Dispersion in One–Dimensional Porous Media Systems' Water Resources Research. Vol. 18(4). p1193

Snow.D.T. (1968) 'Rock Fracture Spacings. Openings and Porosities' Journal of the Soil Mech. and Found. Div. of ASCE. Vol SM1. p73

Talbot.A. (1979) 'The Accurate Numerical Inversion of Laplace Transforms' J. Inst. Maths. Applics. Vol. 23. p 97

Watson.B.P., Leath.P.L. (1974) 'Conductivity in the two-dimensional Site Percolation Problem' Physical Review B Vol.9. p4893

Wickens.L.M. (1981) 'A User's Guide for the Program NAMMU: II. An Example Problem' Harwell Report AERE-R 10274

Wickens.L.M., Robinson.P.C. (1984) 'Finite-element Modelling of Groundwater Flow in Hard Rock Regions Containing a Heat-emitting Radioactive Waste Repository' Ann. Nucl. Energy. Vol. 11. p15

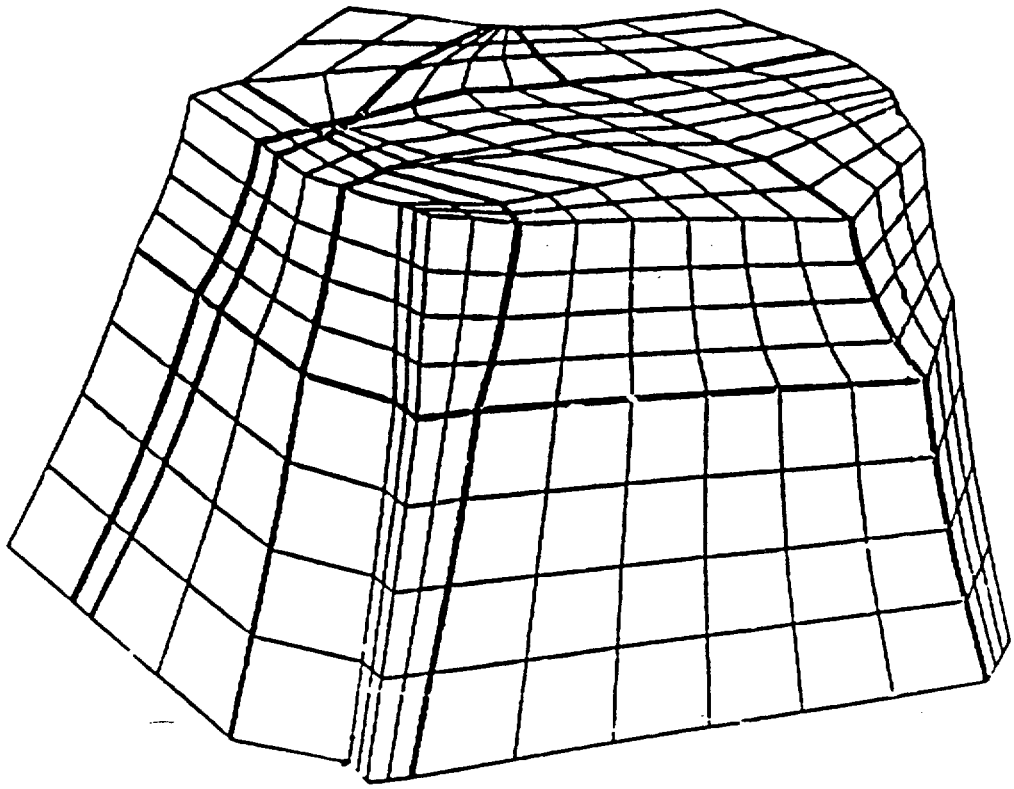

Figure 1.1. Finite element grid for typical three-dimensional continuum groundwater flow calculation. Only the surface elements are shown. The dark bands are fracture zones modelled by three rows of thin elements.

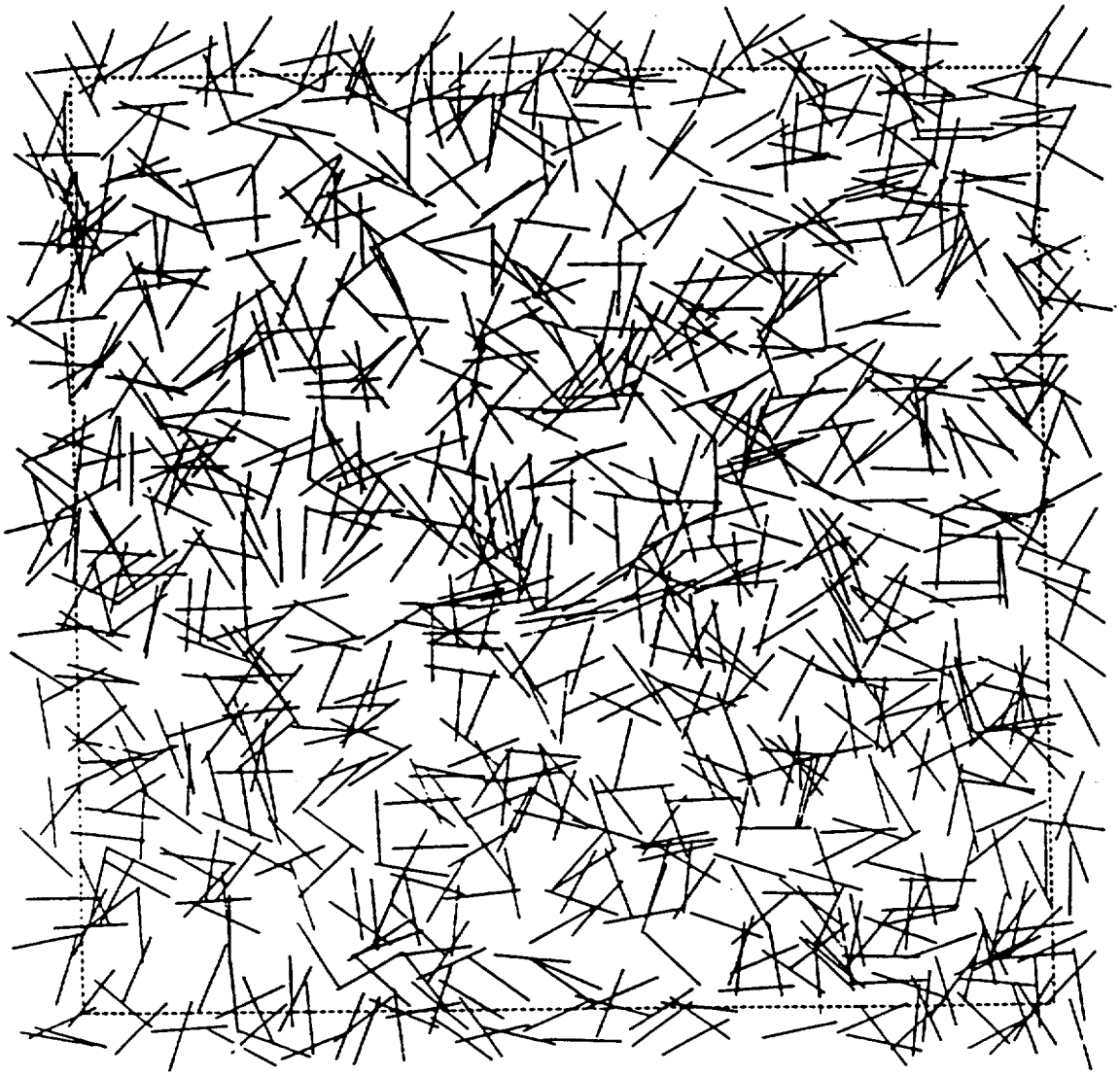

Figure 3.1. Typical percolating system. This example is from the case with uniformly distributed orientations and fixed length fractures.

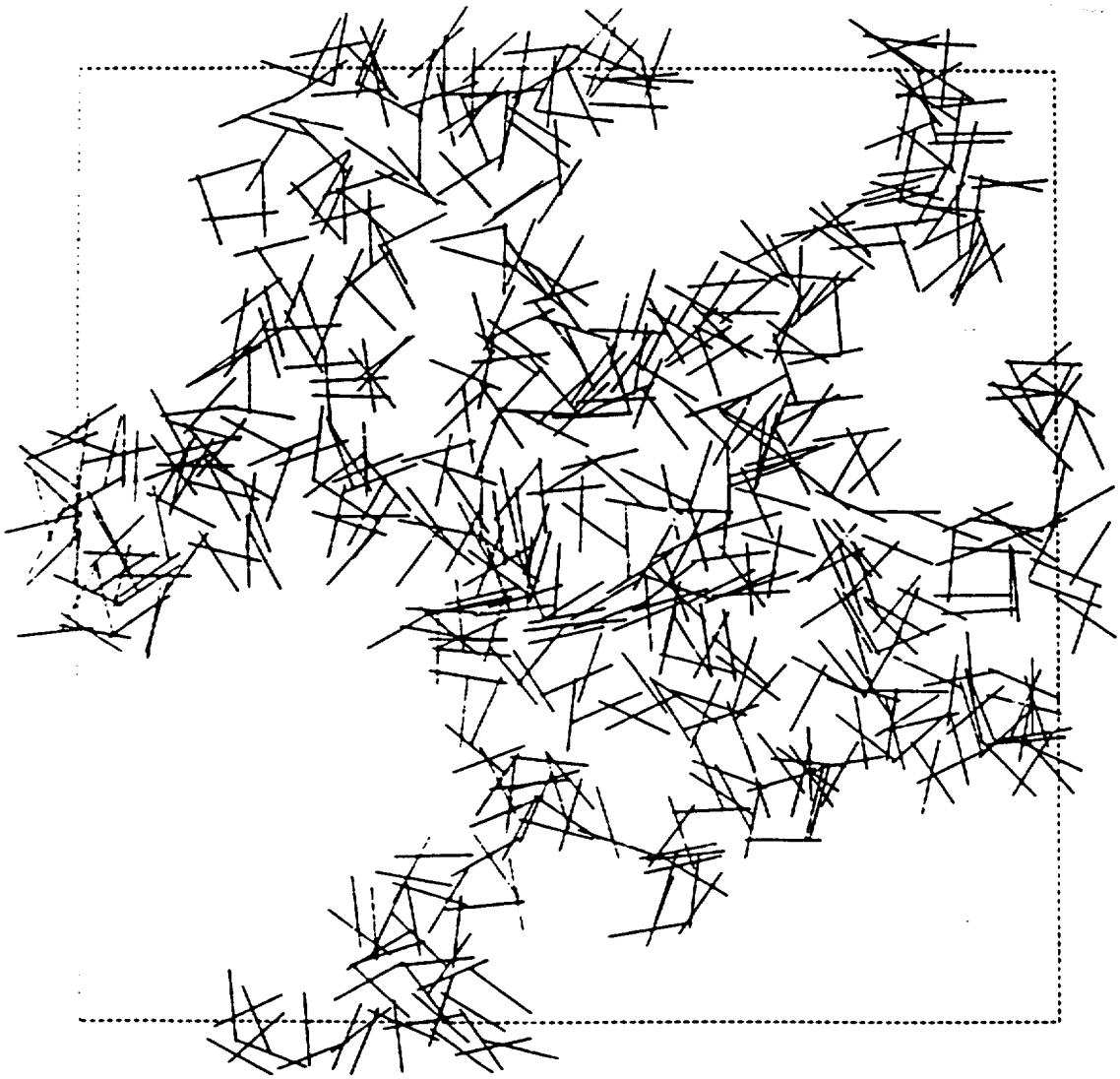

Figure 3.2. The percolating cluster from the system shown in figure 3.1. All the fractures in the cluster which reached all four sides are shown.

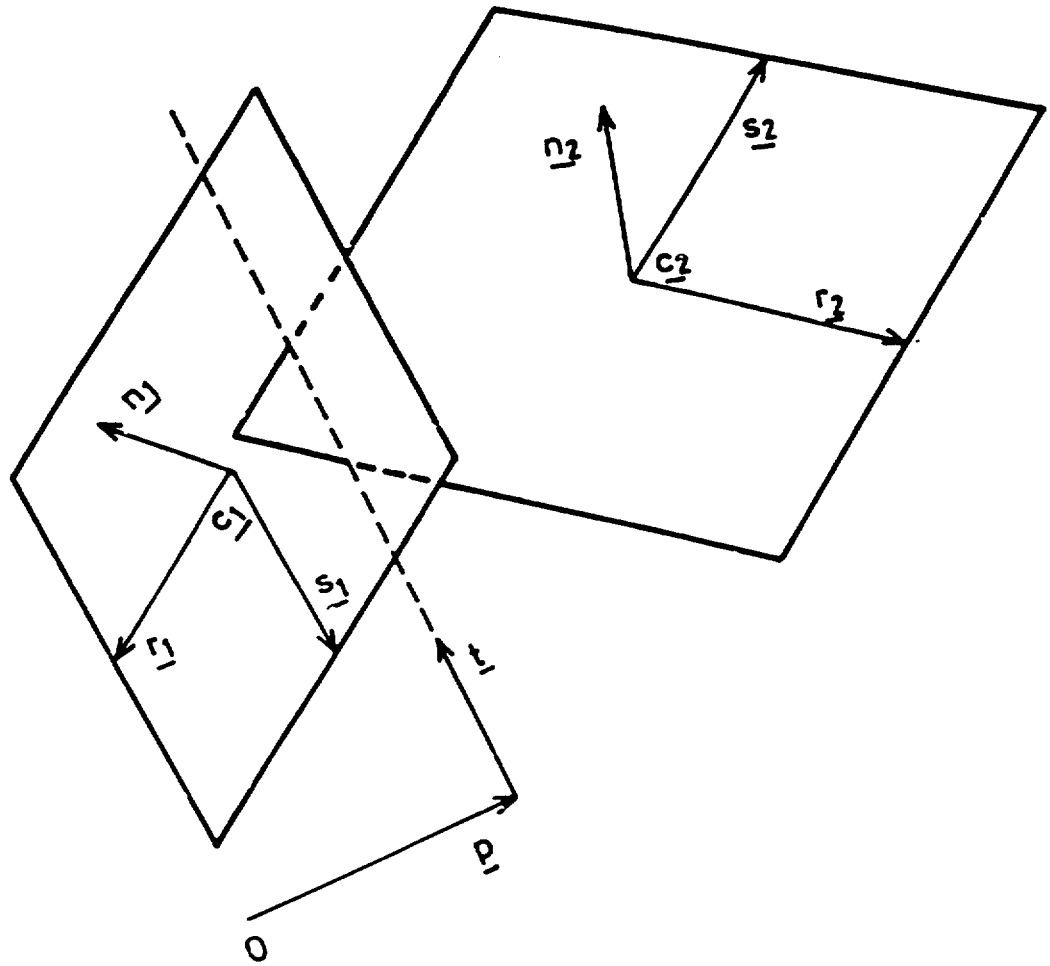

Figure 3.3. Notation for intersecting fracture planes.

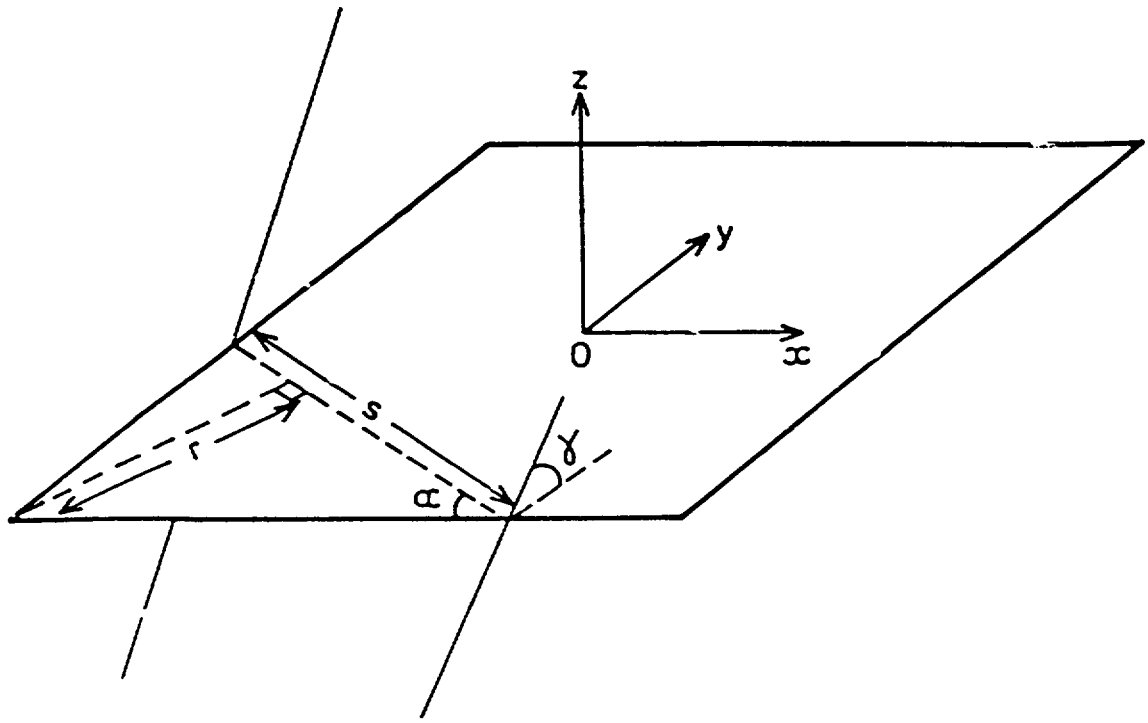

Figure 3.4. Notation for calculating the average number of intersections per plane in three-dimensional systems.

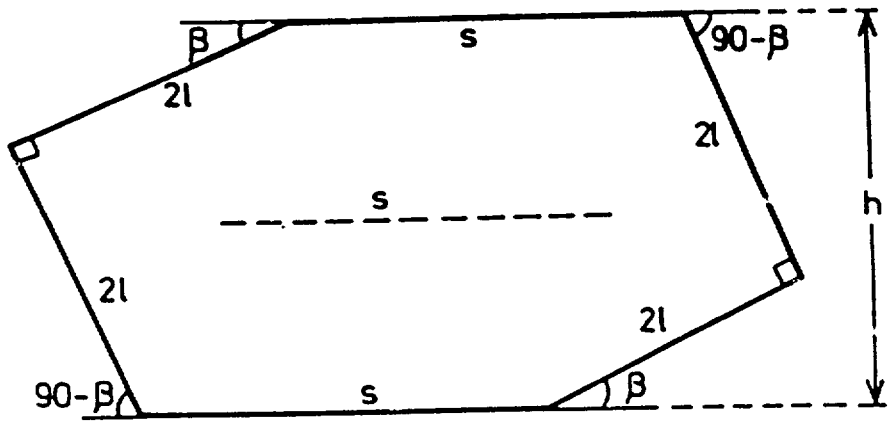

Figure 3.5. Notation for calculating the average number of intersections per plane in three-dimensional systems.

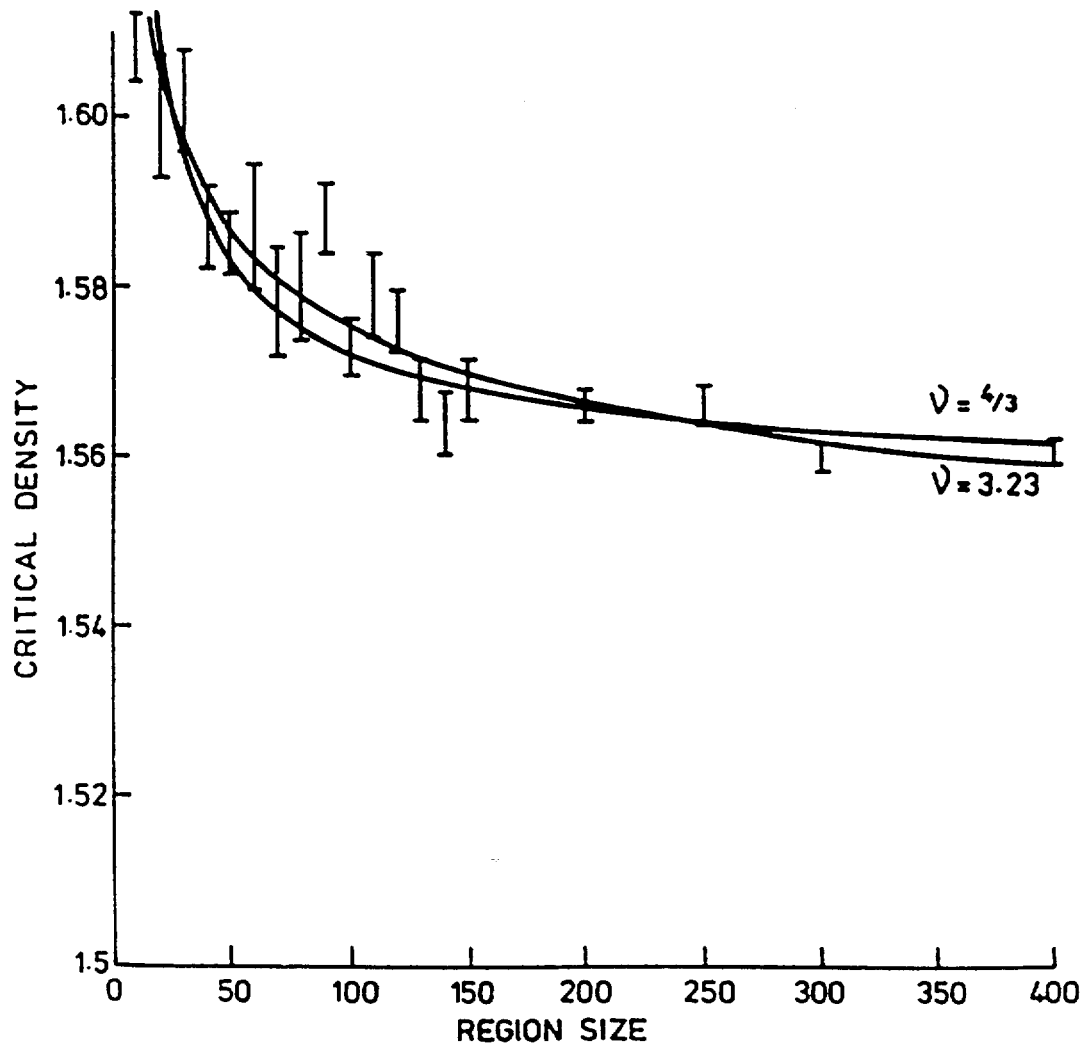

Figure 3.6. Critical density versus region size. The fractures were all of length 2 units with orientations in one of two orthogonal directions. The solid lines show the best fit to the finite-size scaling curve with $\nu = \frac{4}{3}$ and with ν allowed to vary.

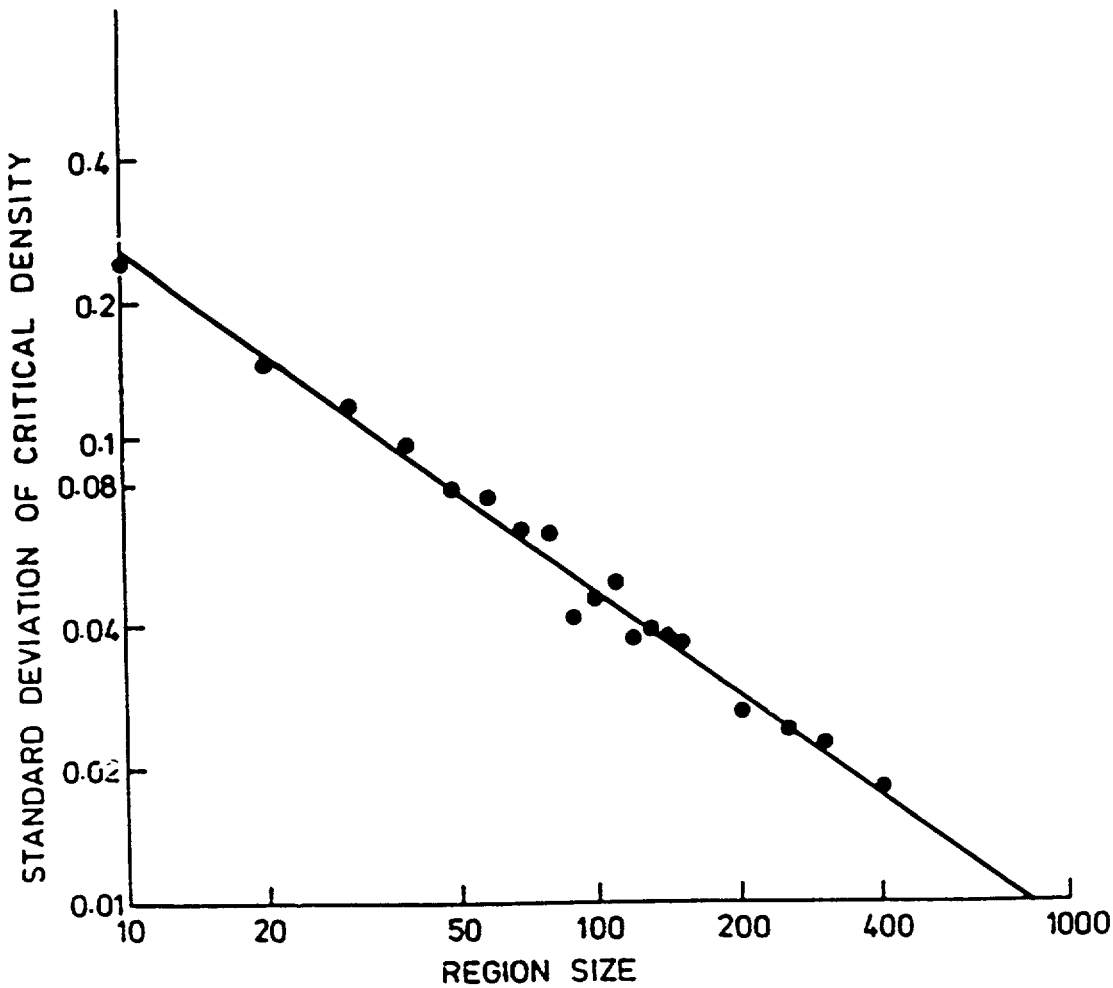

Figure 3.7. Standard deviation of critical density versus region size for the same case as figure 3.6.

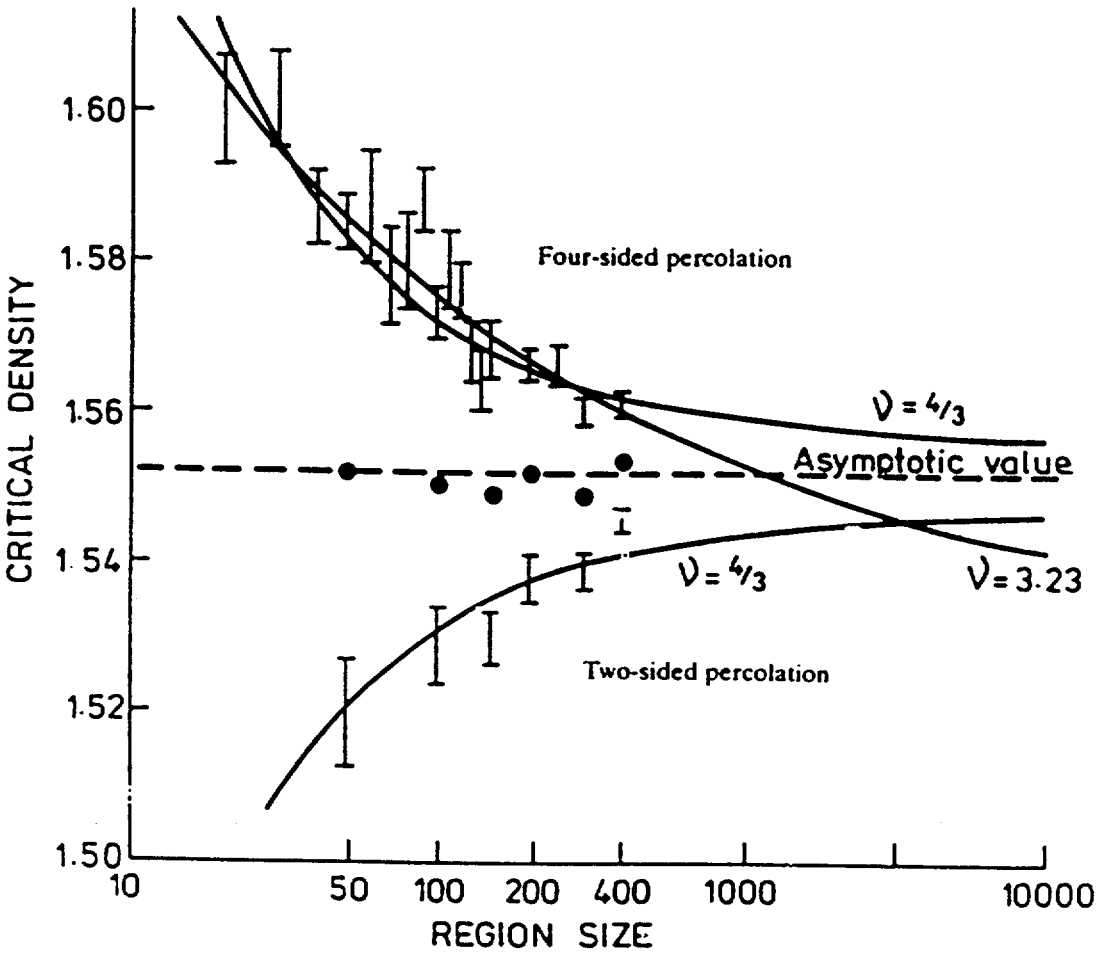

Figure 3.8. Critical density versus region size for the same case as figure 3.6. The results for two-sided and four-sided percolation are shown. The solid lines show the best fit to the finite-size scaling curve with $\nu=\frac{4}{3}$ and with ν allowed to vary. The dots show the average between the two criteria.

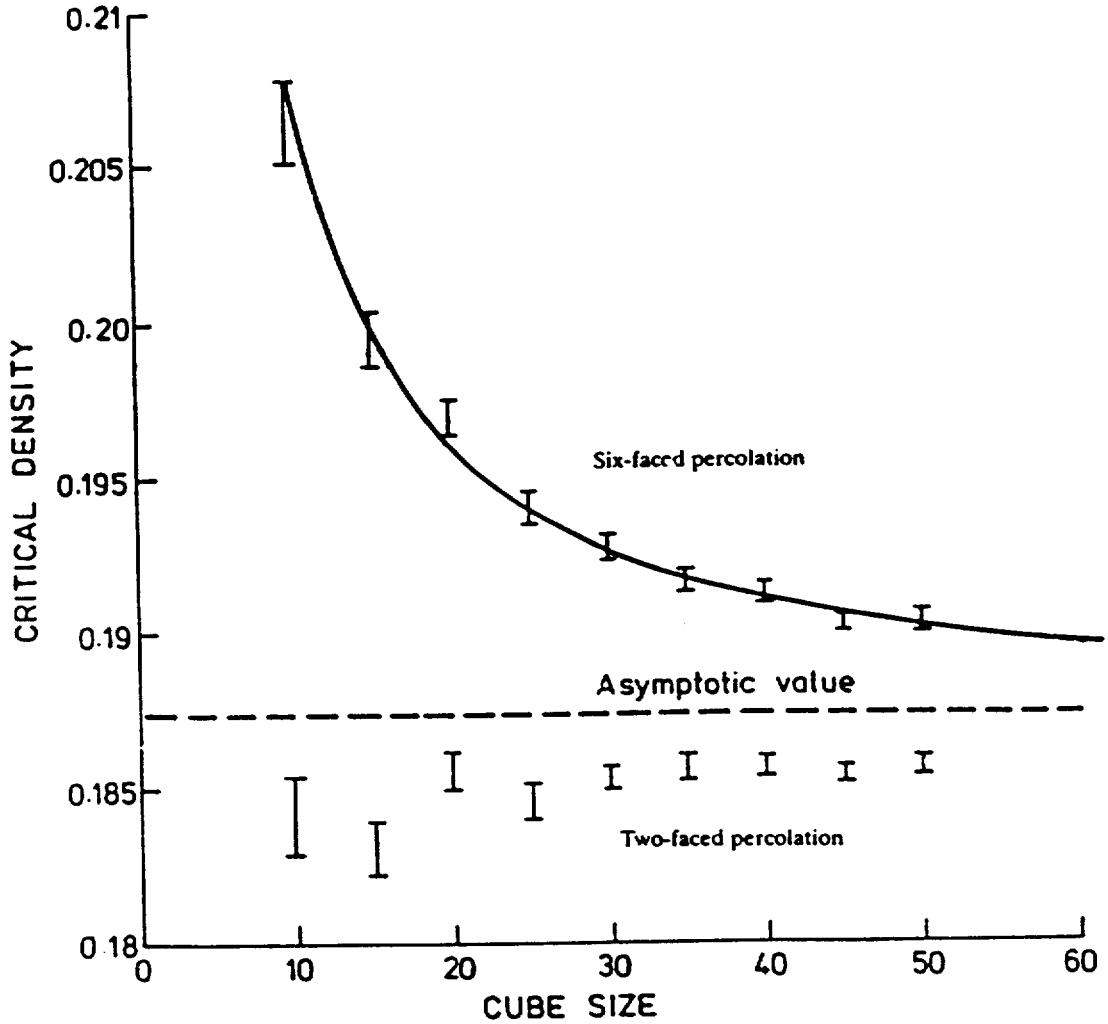

Figure 3.9. Critical density versus region size in three dimensions. The fractures were all of planes 1 unit square oriented in one of three orthogonal directions. The two-faces and six-faces results are shown. The solid line shows the best fit to the finite-size scaling curve with $\nu=\frac{4}{3}$ for the six-faces results.

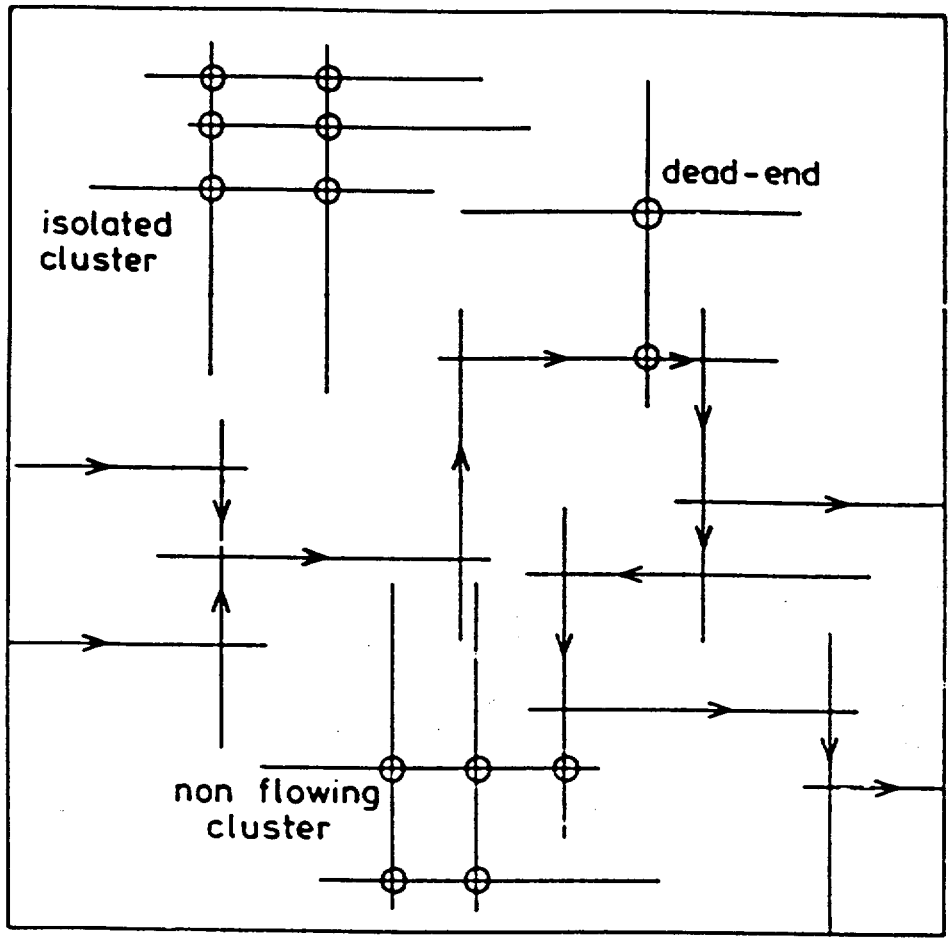

Figure 4.1. Dead-ends, isolated clusters and non-flowing fractures. The arrows show the direction of flow when the left side is at a higher pressure than the right side. The circled intersections can be removed from the calculation.

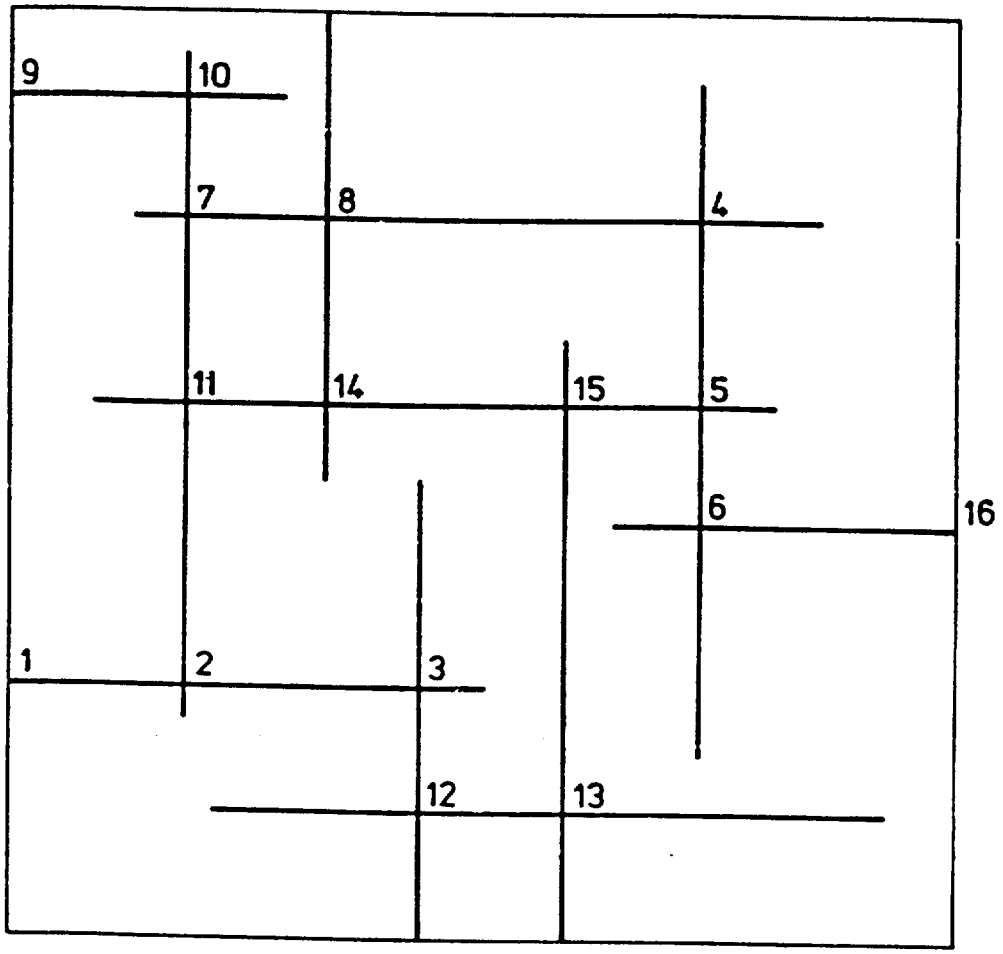

Figure 4.2. Illustration of renumbering algorithm. A possible original network numbering for a small example.

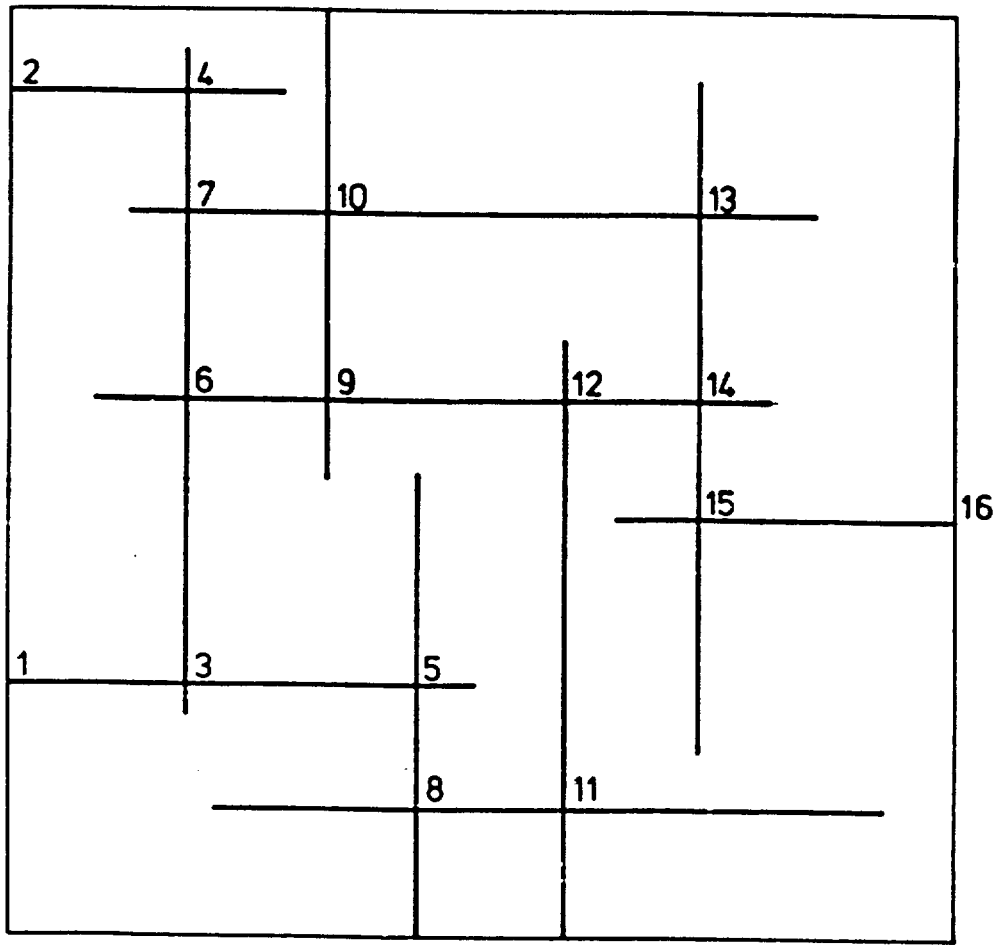

Figure 4.3. Illustration of renumbering algorithm. The network numbering after applying the renumbering algorithm.

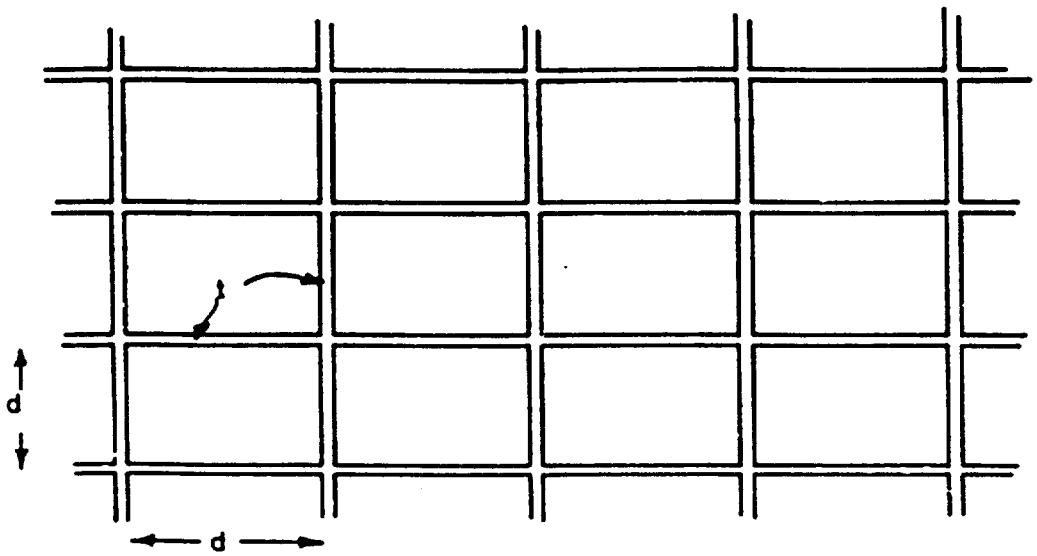

Figure 4.4. The infinite lattice used to calculate permeabilities.

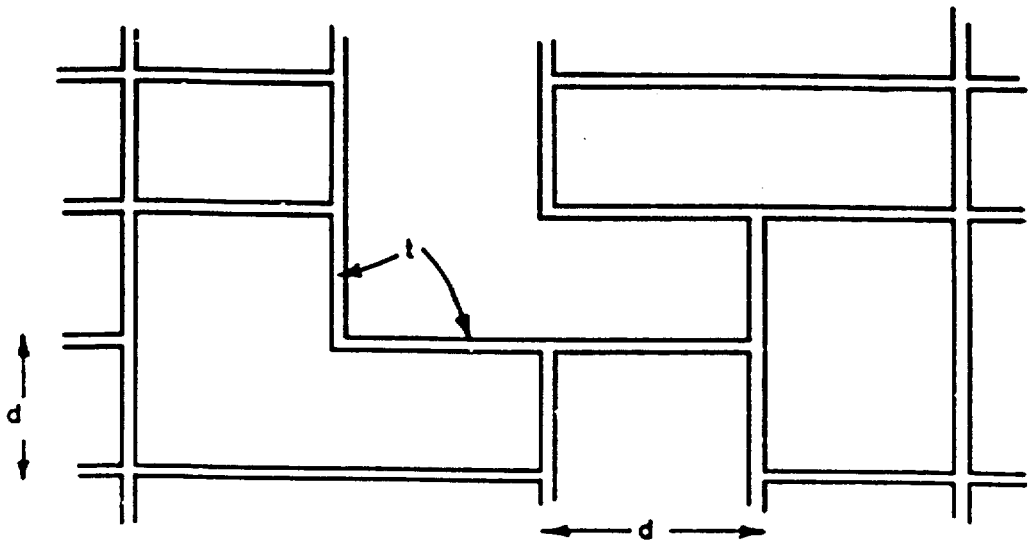

Figure 4.5. A cut lattice used to calculate permeabilities of fracture networks. Here 25% of the connections are missing.

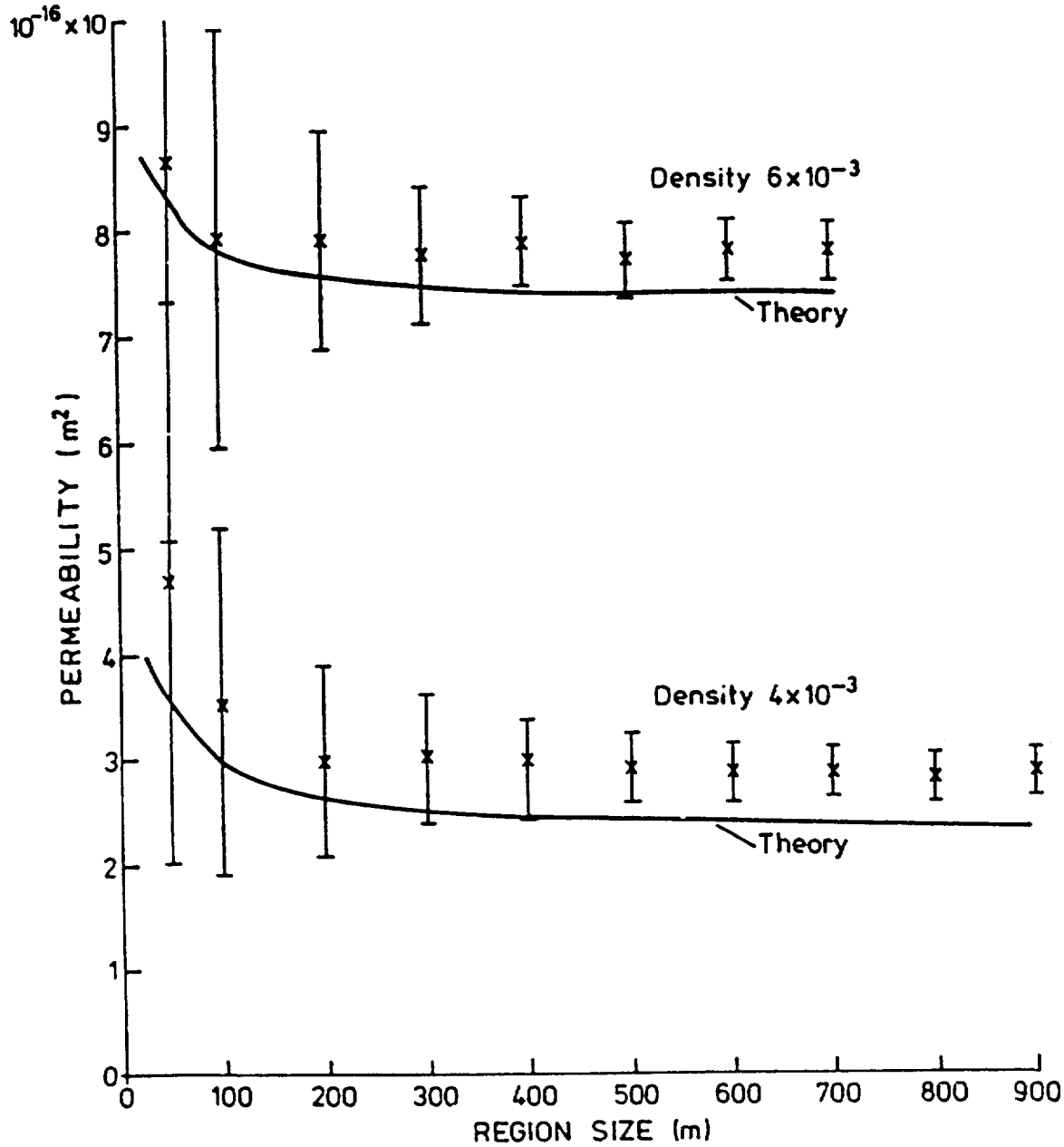

Figure 4.6. Permeability versus region size for densities 4×10^{-3} and 6×10^{-3} fractures per square metre. The fractures were all 50 metres long, with half oriented parallel to the pressure gradient and half perpendicular to it. The solid lines show the theoretical predictions.

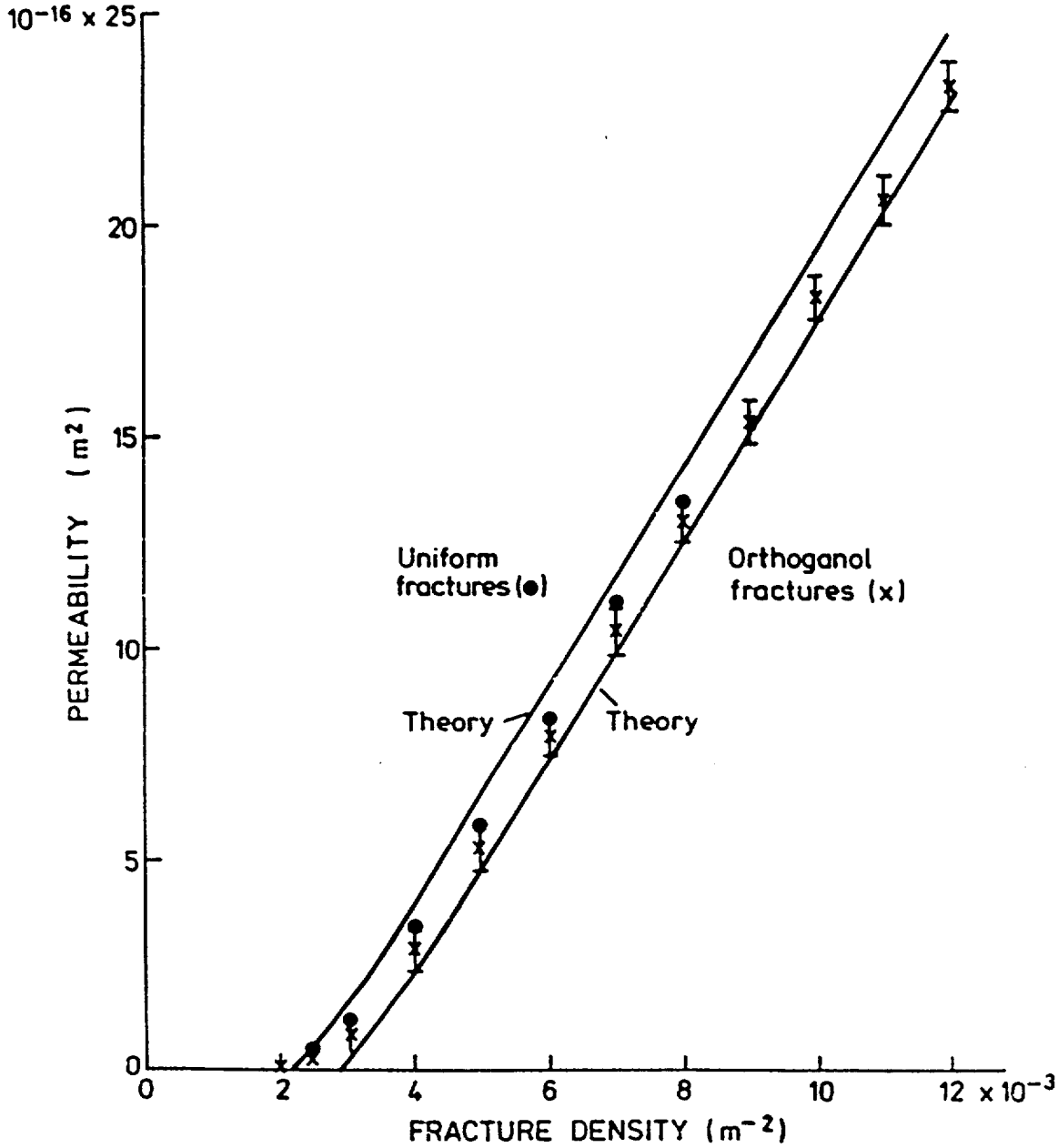

Figure 4.7. Permeability versus fracture density. The region size was 400m in all cases. The fractures were all 50 metres long, with half oriented parallel to the pressure gradient and half perpendicular to it in one case and uniformly distributed in the other. The solid lines show the theoretical predictions.

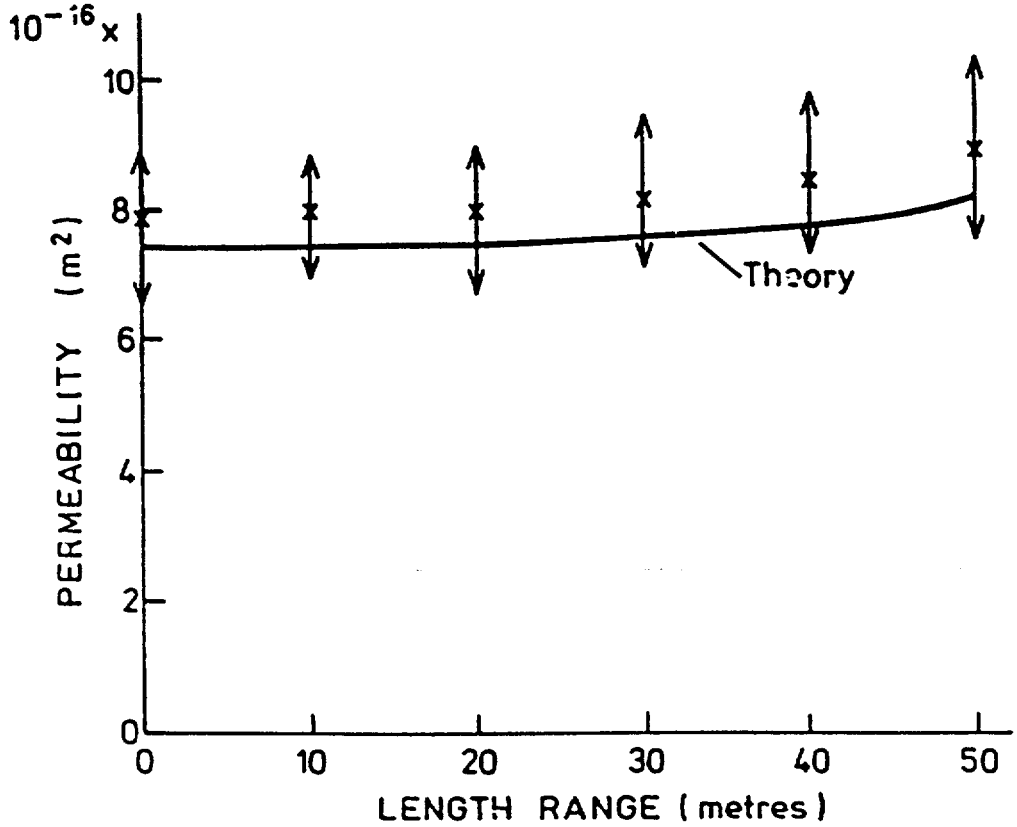

Figure 4.8. Permeability versus length range. The density was 6×10^{-3} fractures per square metre and the region size 400m. Half the fractures were oriented parallel to the pressure gradient and half perpendicular to it. The fracture length had an average of 50m, being uniformly distributed between 50−range and 50+range. The solid line shows the theoretical prediction.

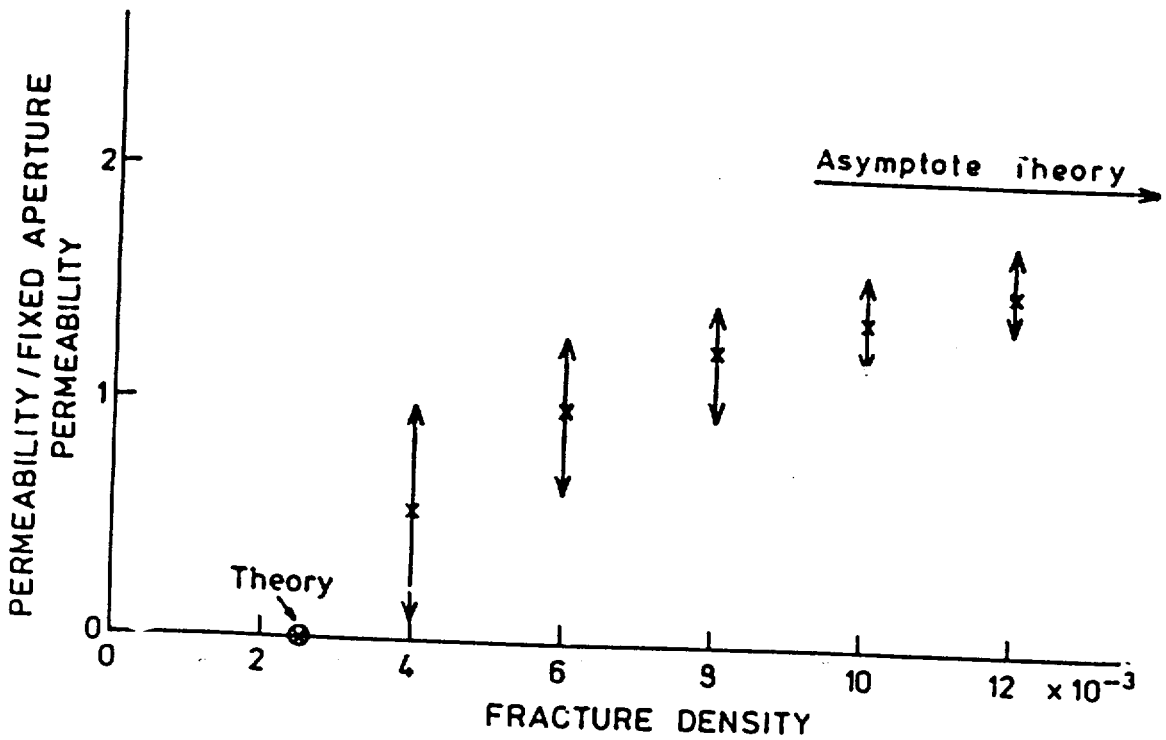

Figure 4.9. Affect of variable aperture on permeability versus fracture density. The region size was 400m. For the varying aperture case apertures were uniformly distributed between zero and 100μm. For the fixed aperture case they were all 50μm. Half the fractures were oriented parallel to the pressure gradient and half perpendicular to it. The fracture length was 50m. The ratio between the permeability in the varying aperture case and the fixed aperture case is shown.

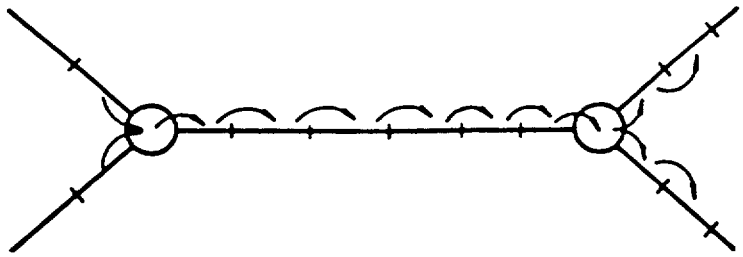

Normal Fracture Segment

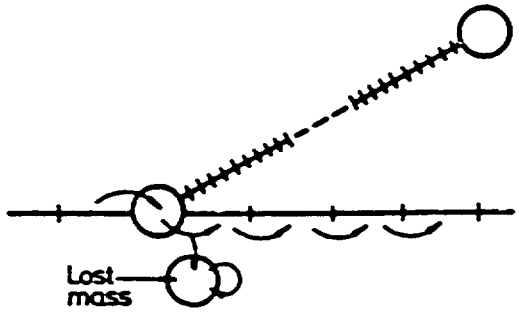

Very Slow Segment

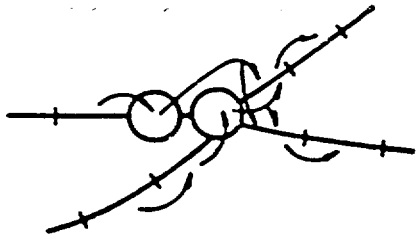

Very Close Intersections

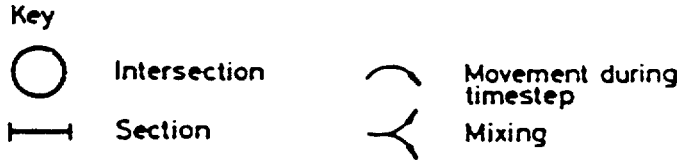

Figure 6.1. Possible movements of mass in a timestep of the mass-lumping algorithm.

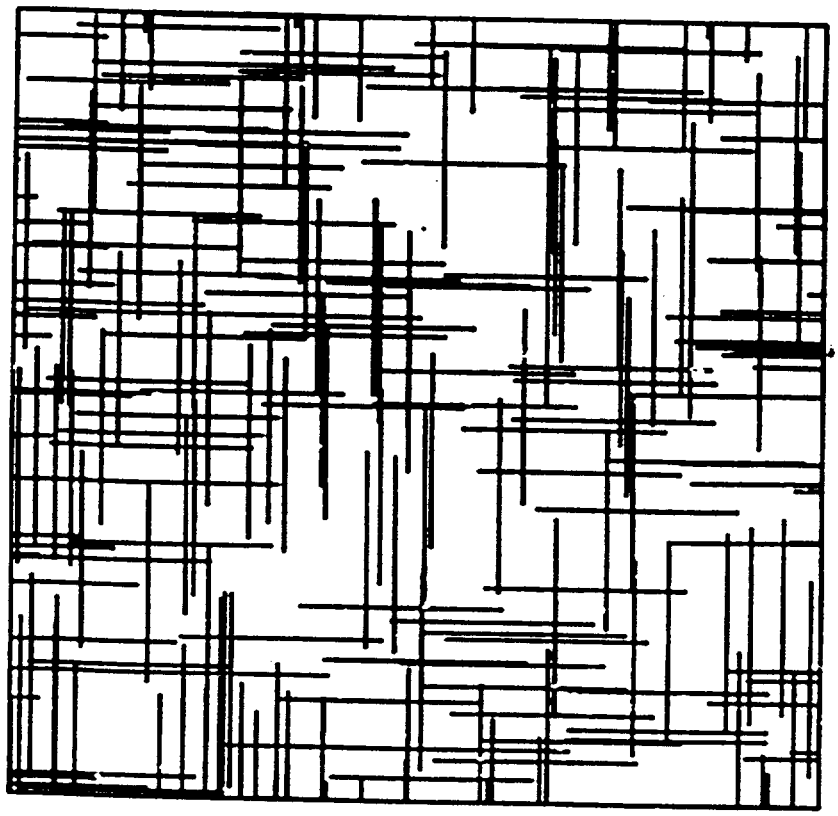

Figure 6.2. The network used for the mass-lumping example. The region is 200m square. Half the fractures were oriented parallel to the pressure gradient and half perpendicular to it. The fracture length was 50m.

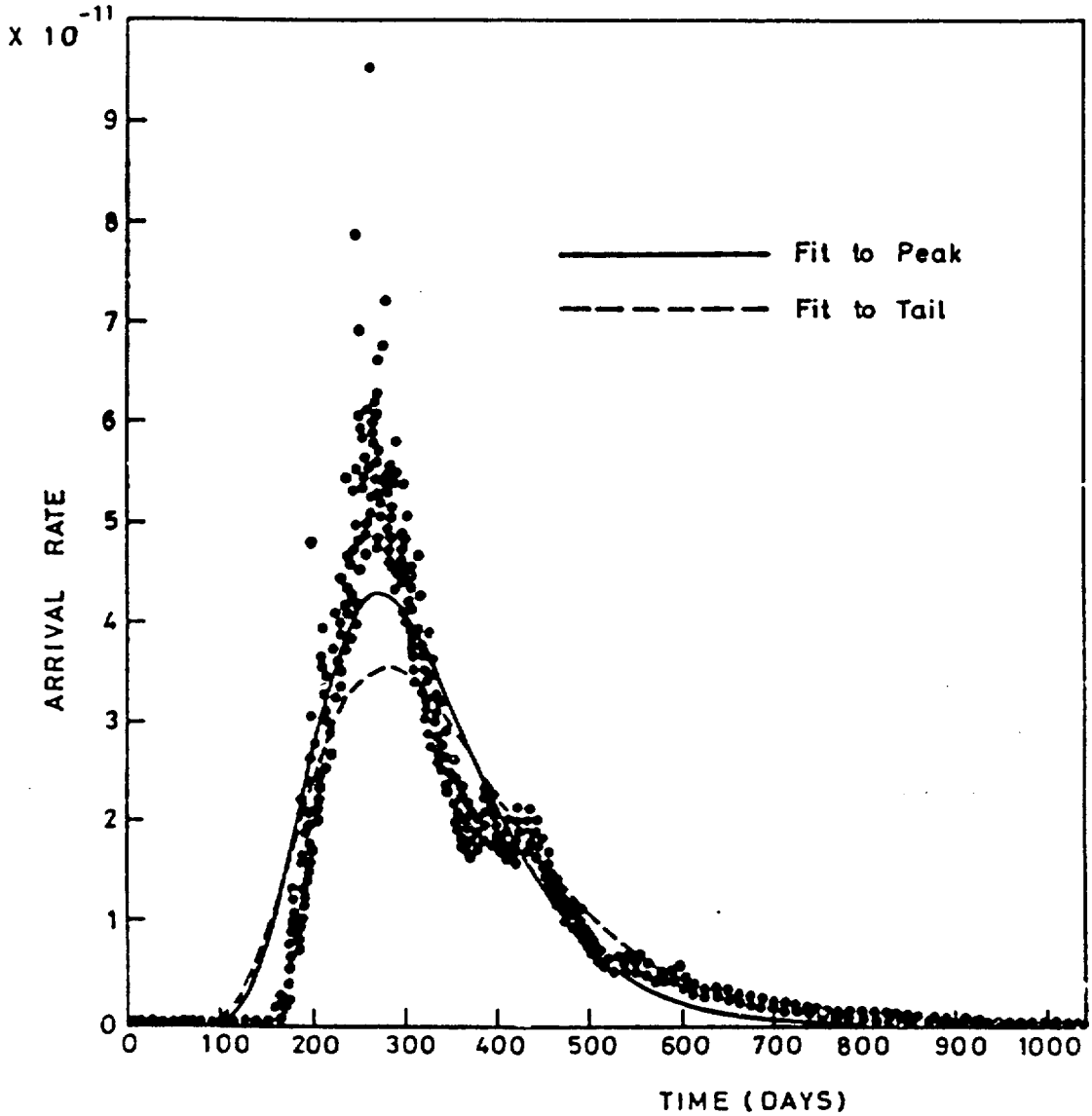

Figure 6.3 The breakthrough curve for the mass-lumping example. The solid and dashed curves show the best fit of a diffusion-like curve to the peak and to the tail.

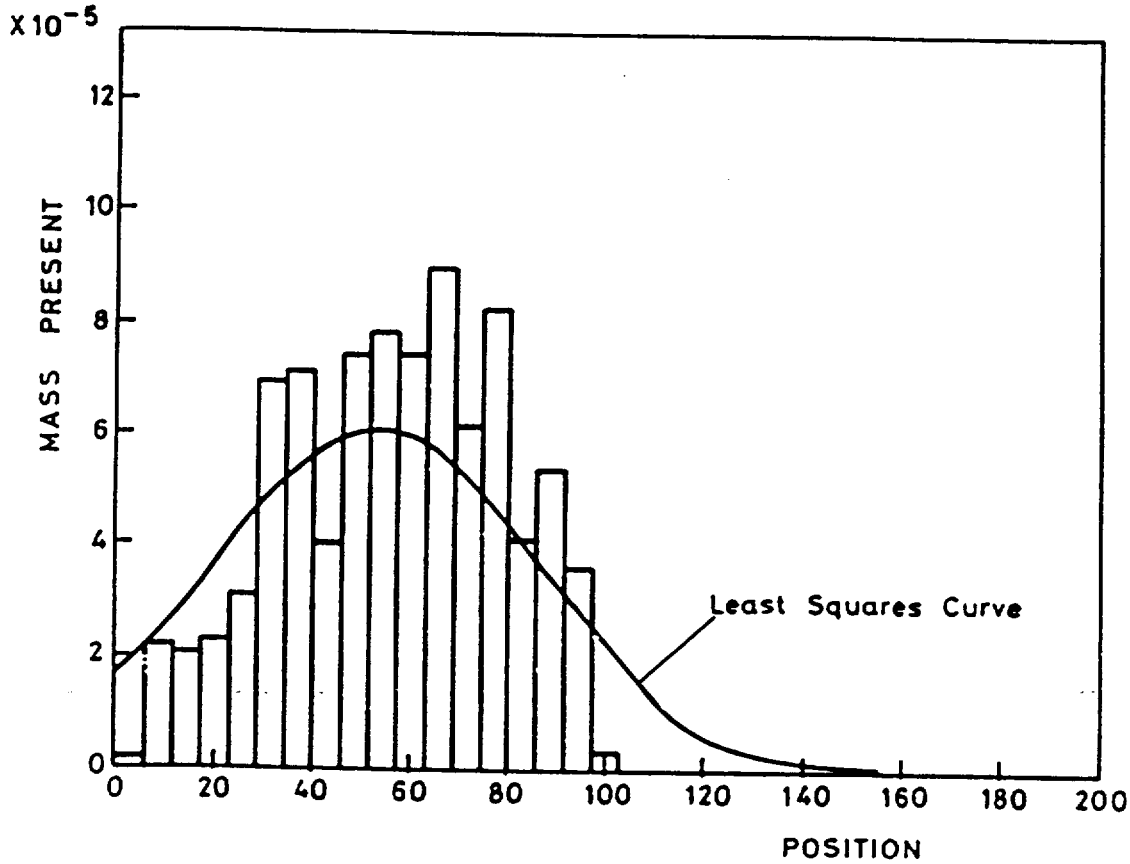

Figure 6.4. The distribution of mass after 80 days for the mass-lumping example. The solid curve shows the diffusion-like result using the parameters for the fit to the peak arrival rate. The total mass in slices across the network is shown.

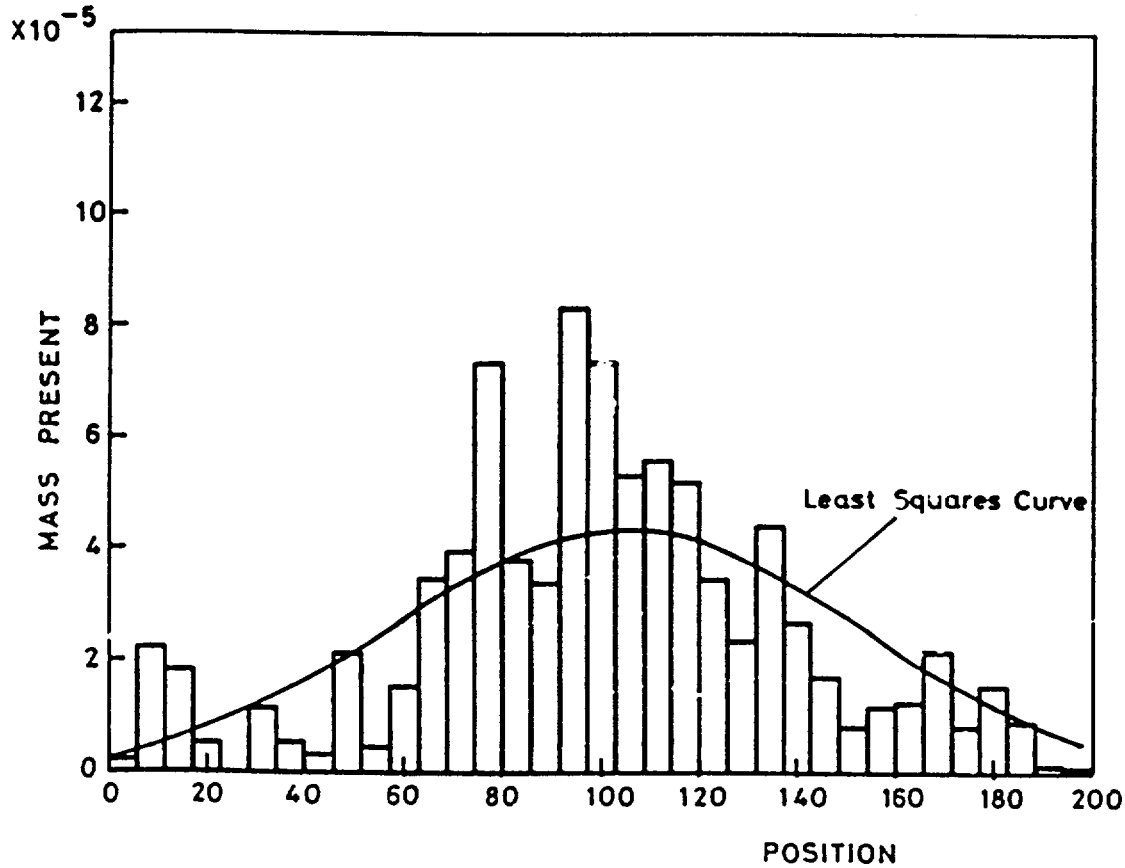

Figure 6.5. The distribution of mass after 160 days for the mass-lumping example. The solid curve shows the diffusion-like result using the parameters for the fit to the peak arrival rate. The total mass in slices across the network is shown.

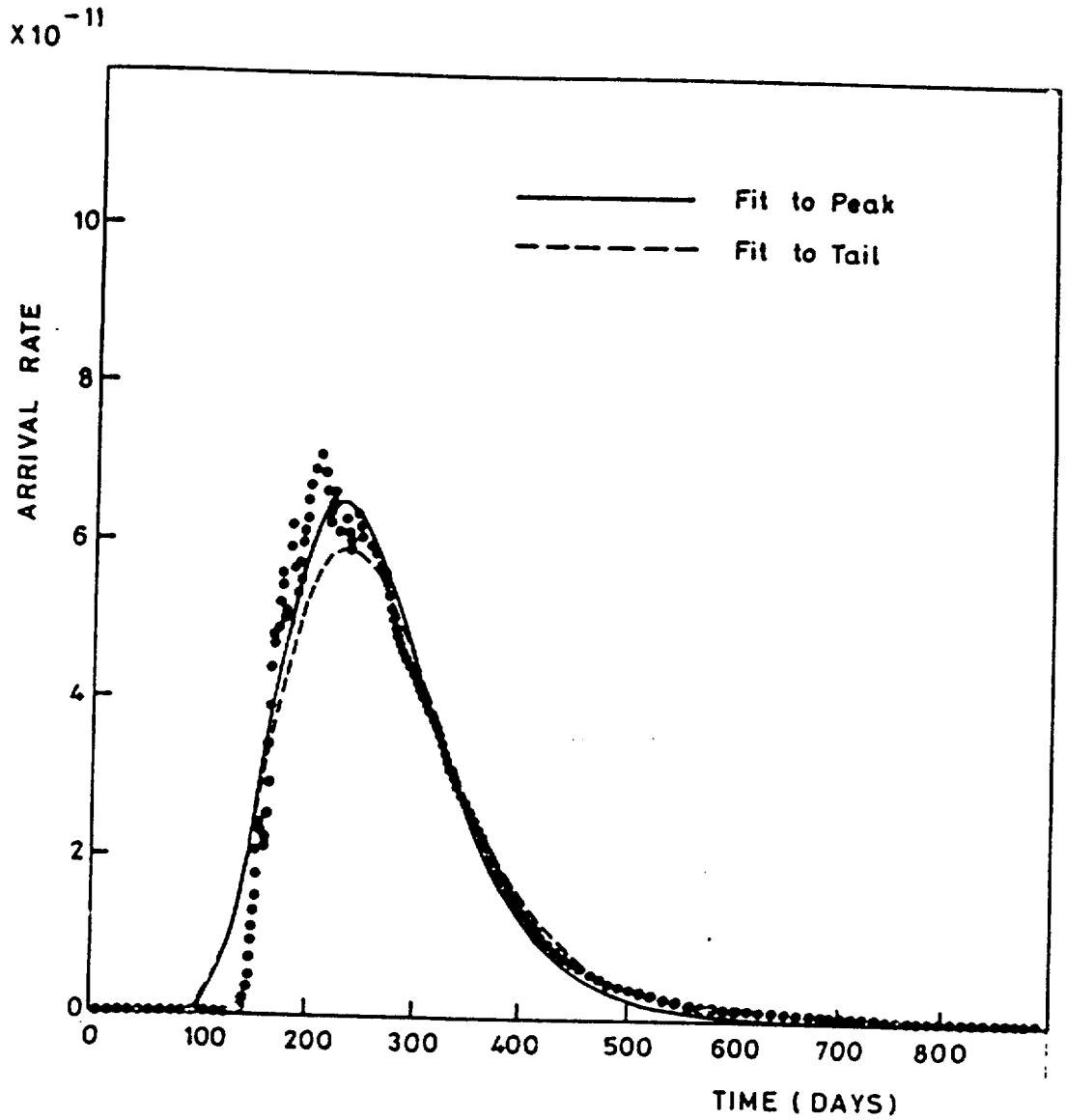

Figure 6.6. The average breakthrough curve over 20 cases using the mass-lumping algorithm. The solid and dashed curves show the best fit of a diffusion-like curve to to the peak and to the tail.

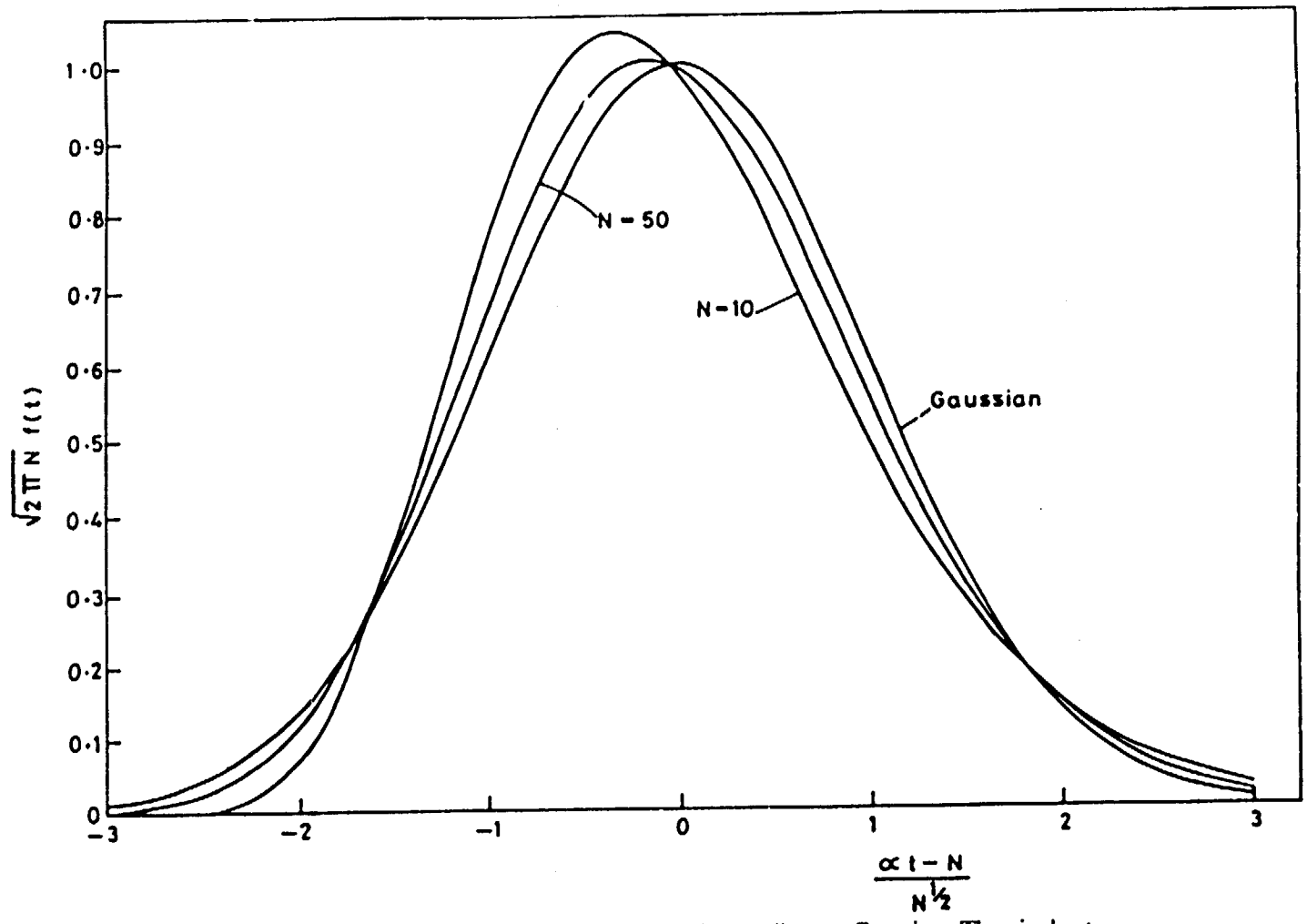

Figure 8.1. Approach of times after N steps of a random walk to a Gaussian. The single step probability distribution function is $\alpha e^{-\alpha t}$.

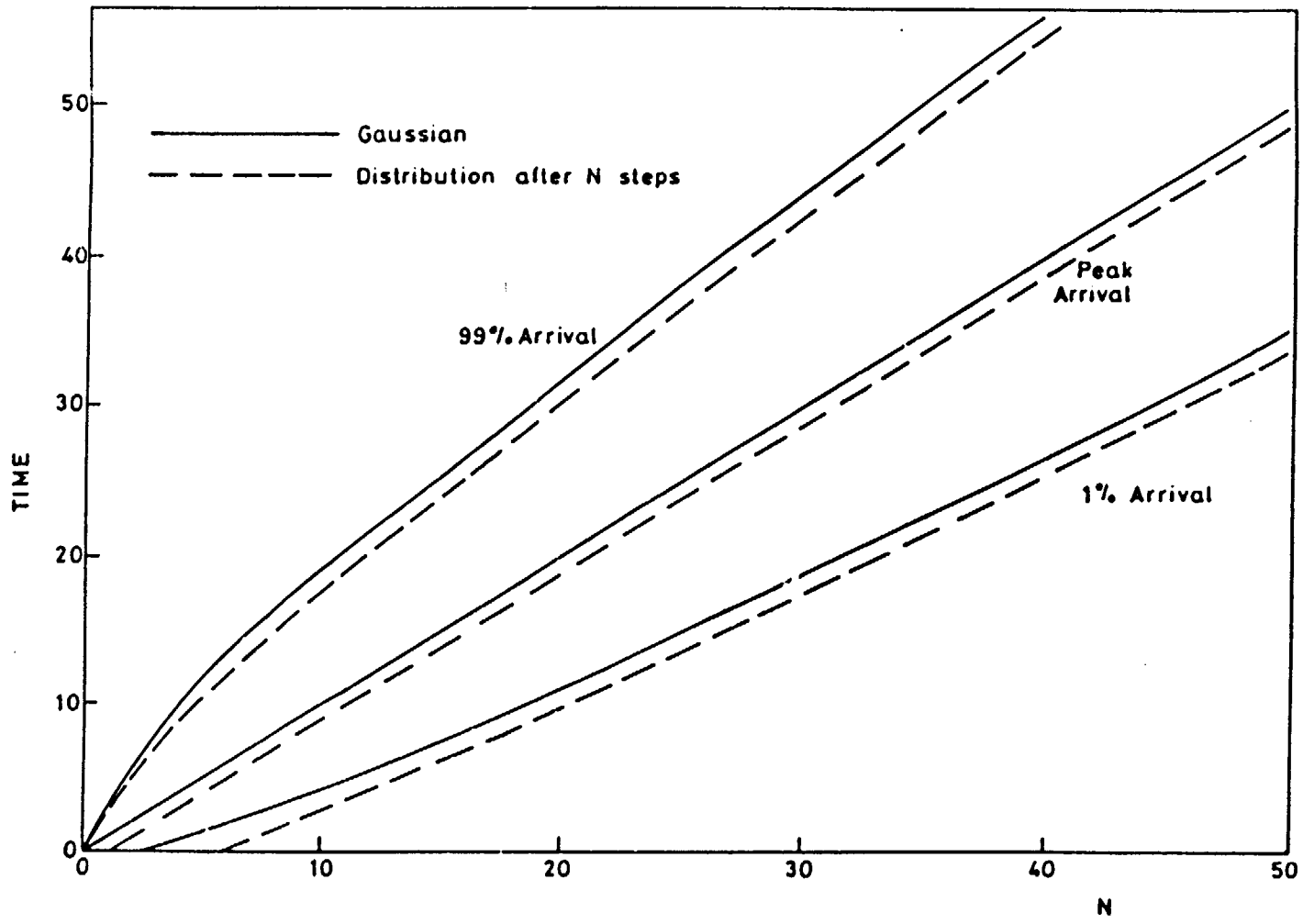

Figure 8.2. Difference between arrival times after N steps of a random walk and a Gaussian. The single step probability distribution function is e^{-t}. The times by which 1% and 99% have arrived are shown as well as the time of peak arrival rate.

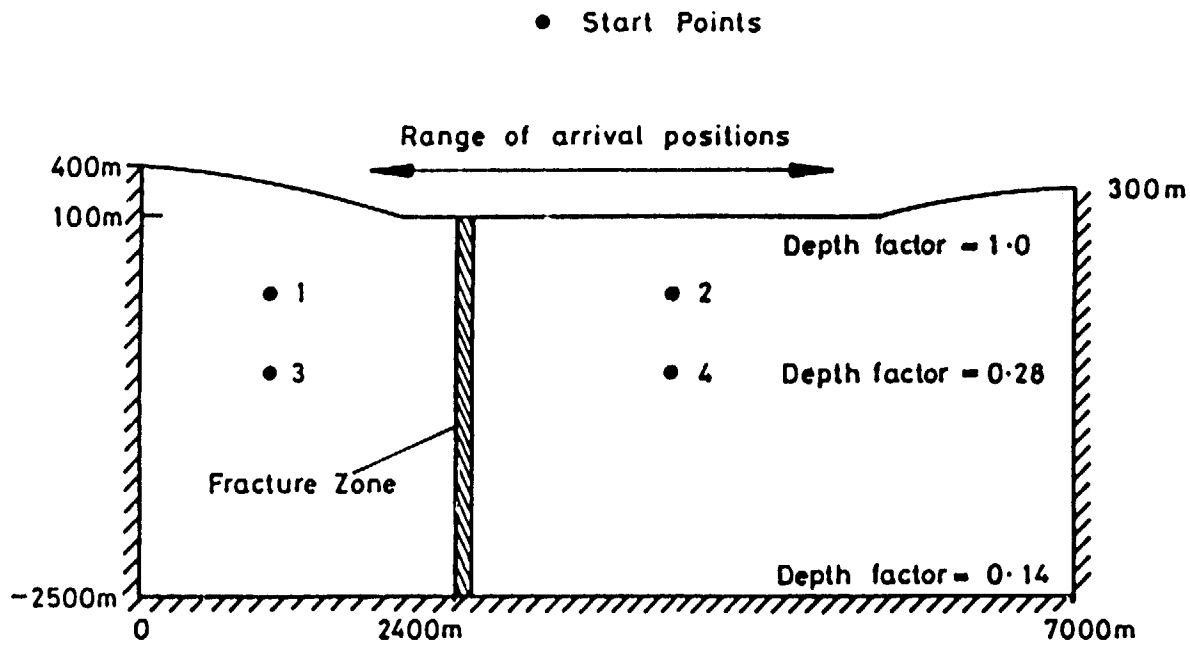

Figure 9.1. The region used for the full network example.

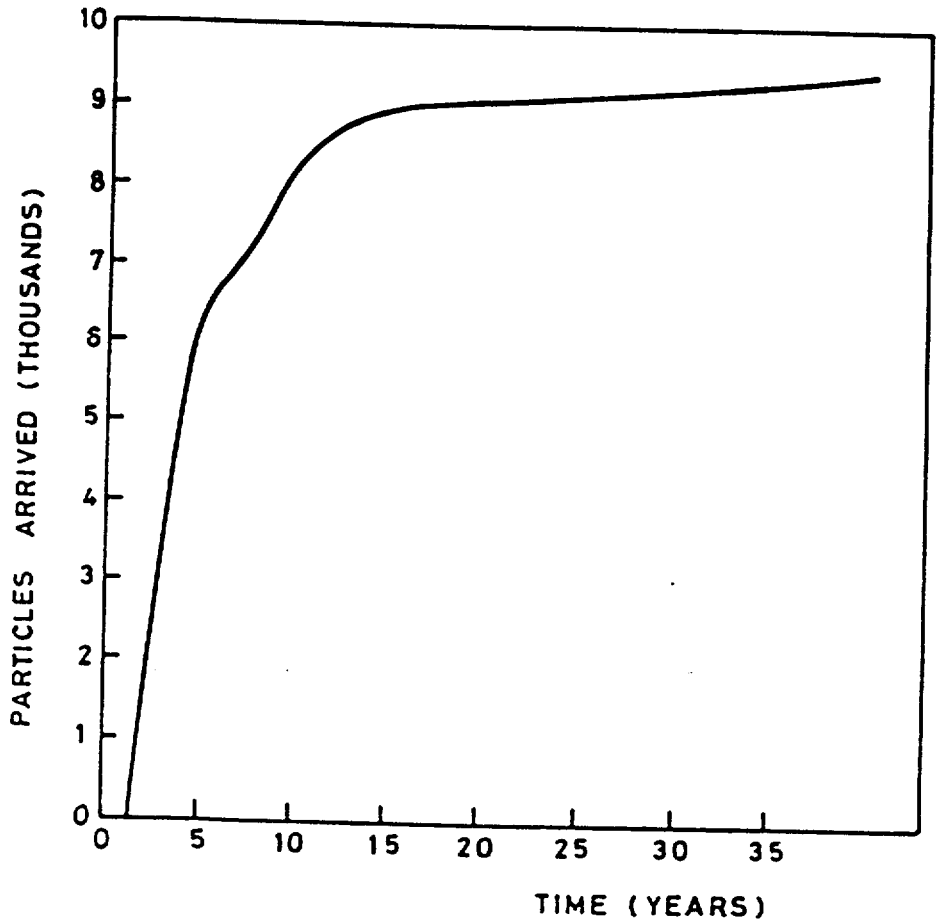

Figure 9.2. The number of particles arrived against time for starting position 1.

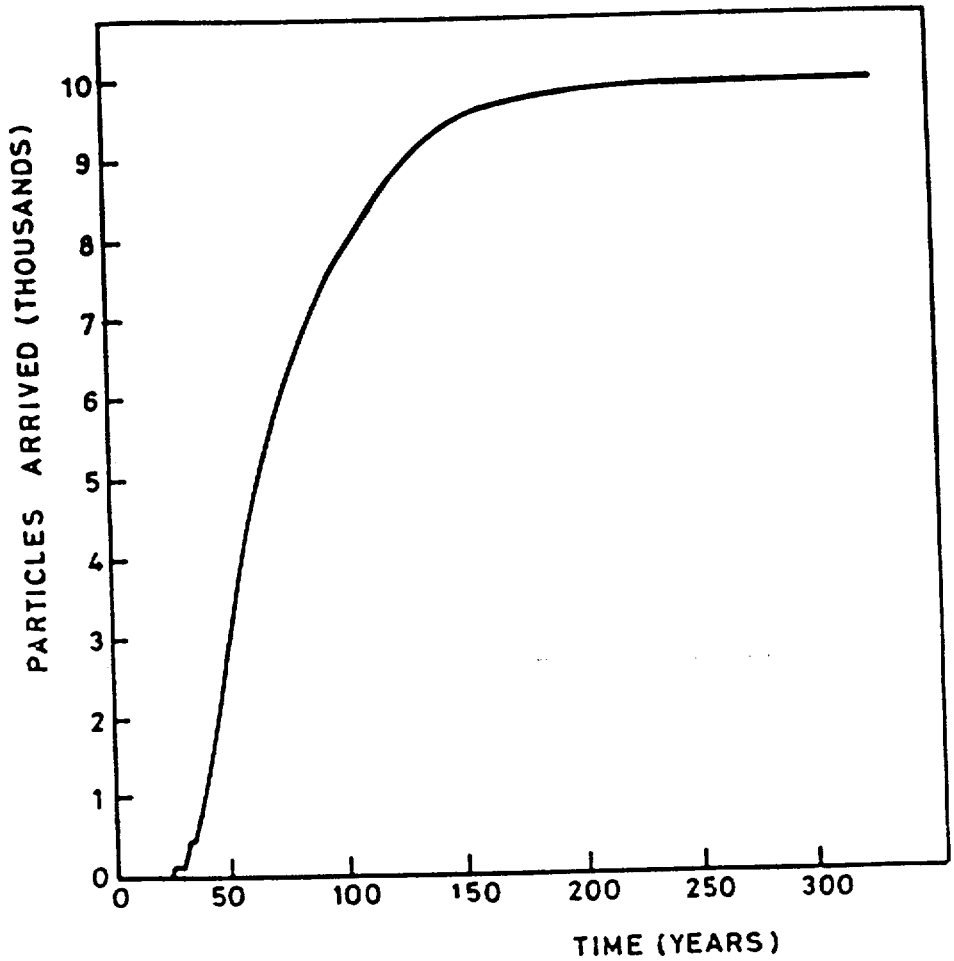

Figure 9.3. The number of particles arrived against time for starting position 2.

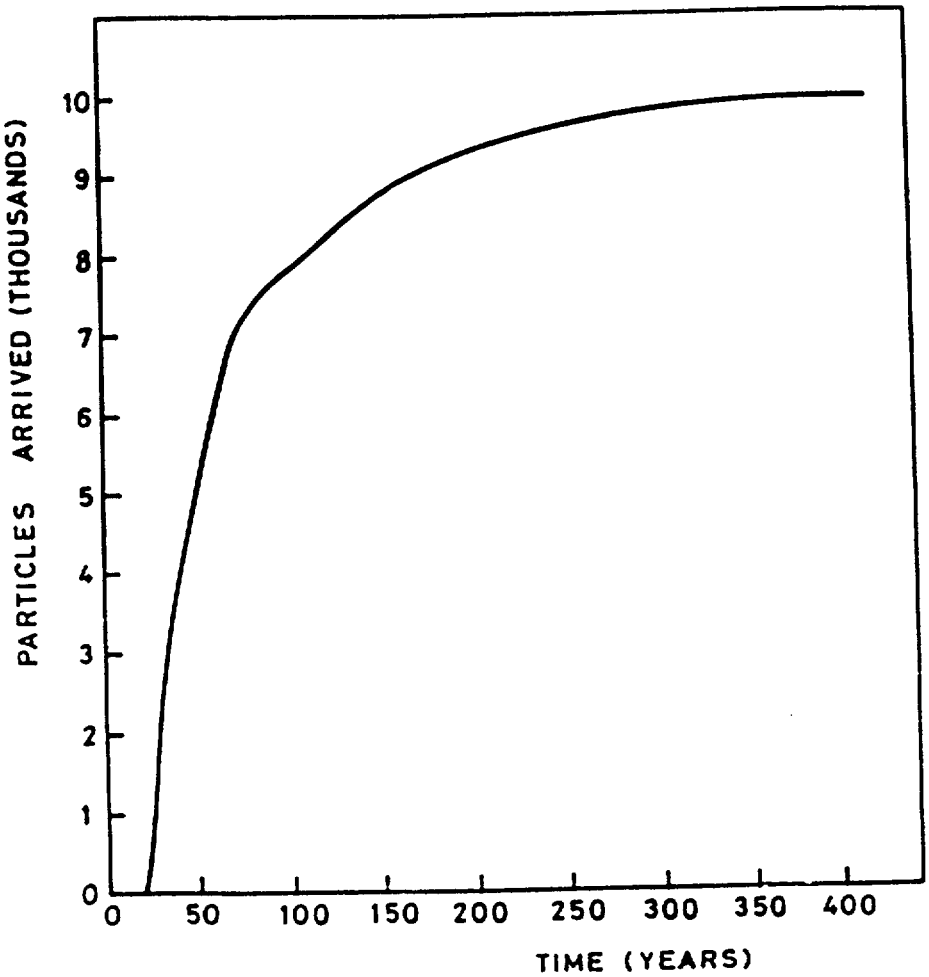

Figure 9.4. The number of particles arrived against time for starting position 3.

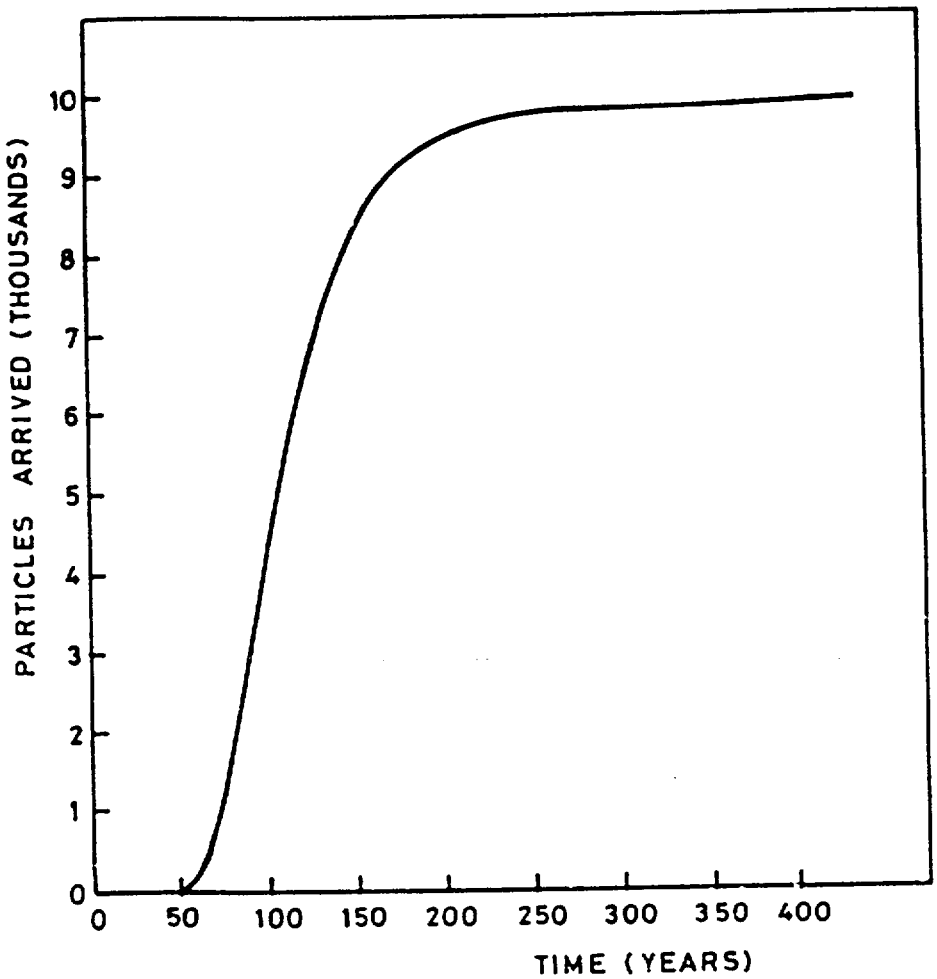

Figure 9.5. The number of particles arrived against time for starting position 4.

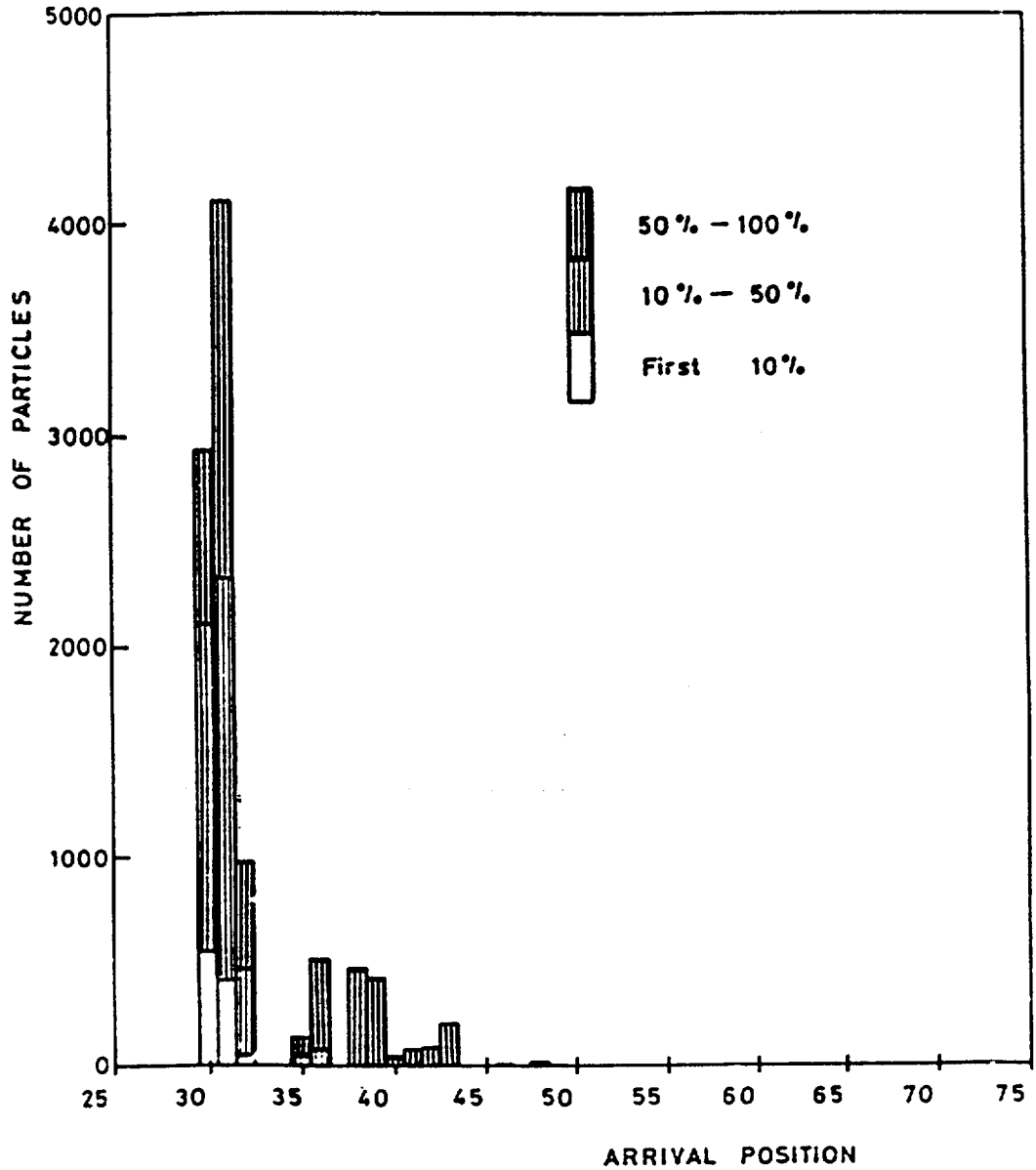

Figure 9.6. The position at which particles arrive at the surface for starting position 1. The arrival positions for the first 10%. the next 40% and the final 50% are shown.

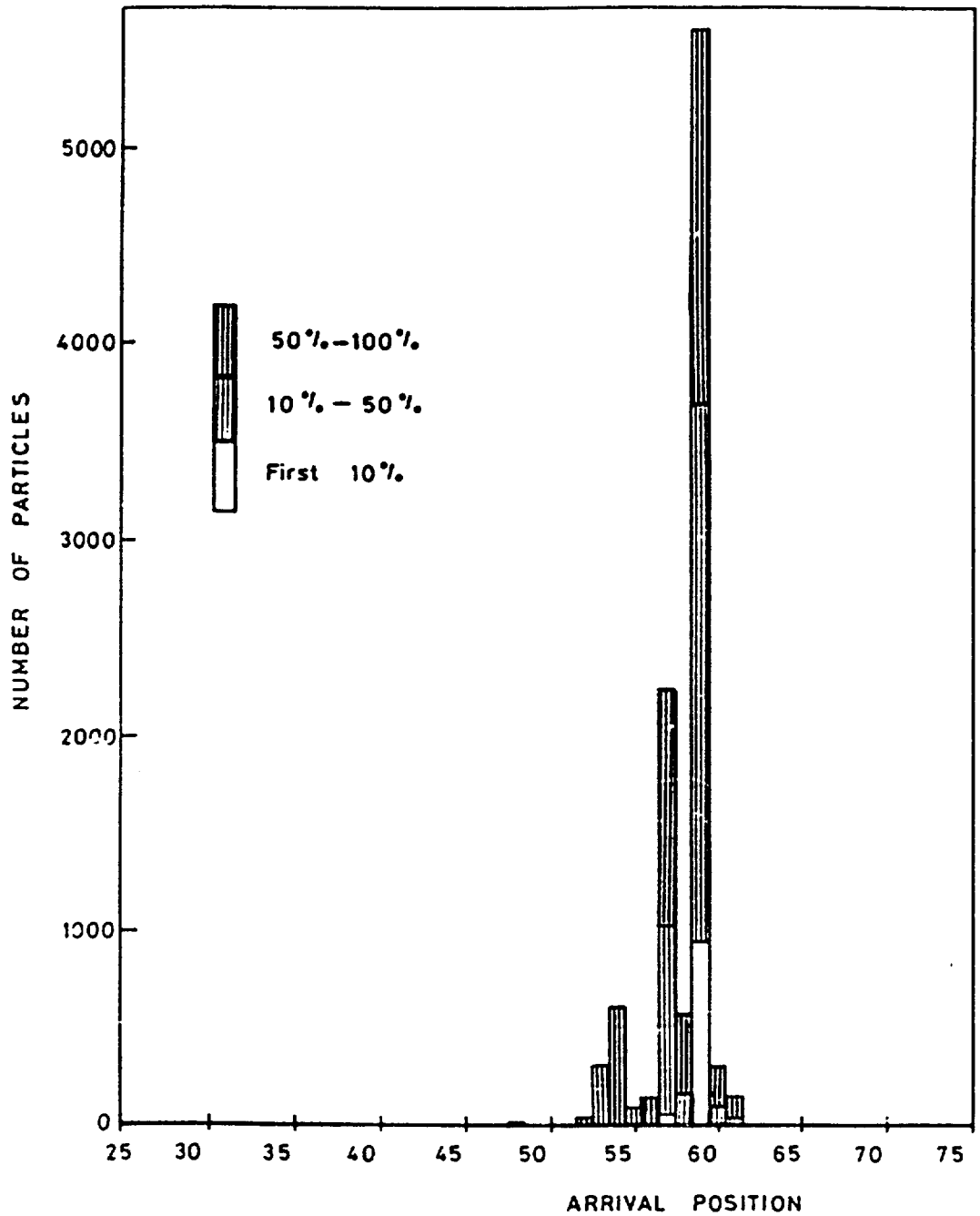

Figure 9.7. The position at which particles arrive at the surface for starting position 2. The arrival positions for the first 10%, the next 40% and the final 50% are shown.

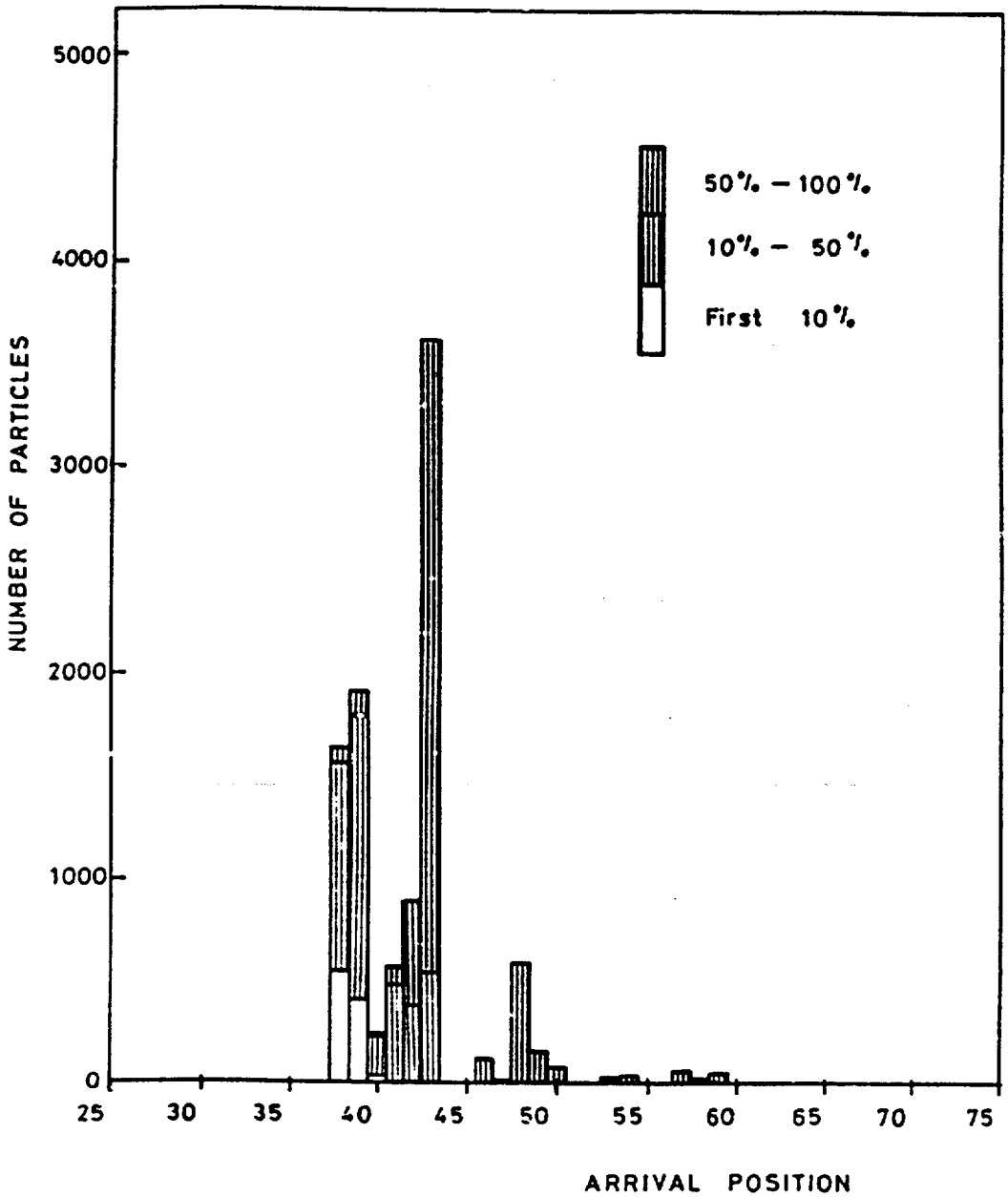

Figure 9.8. The position at which particles arrive at the surface for starting position 3. The arrival positions for the first 10%, the next 40% and the final 50% are shown.

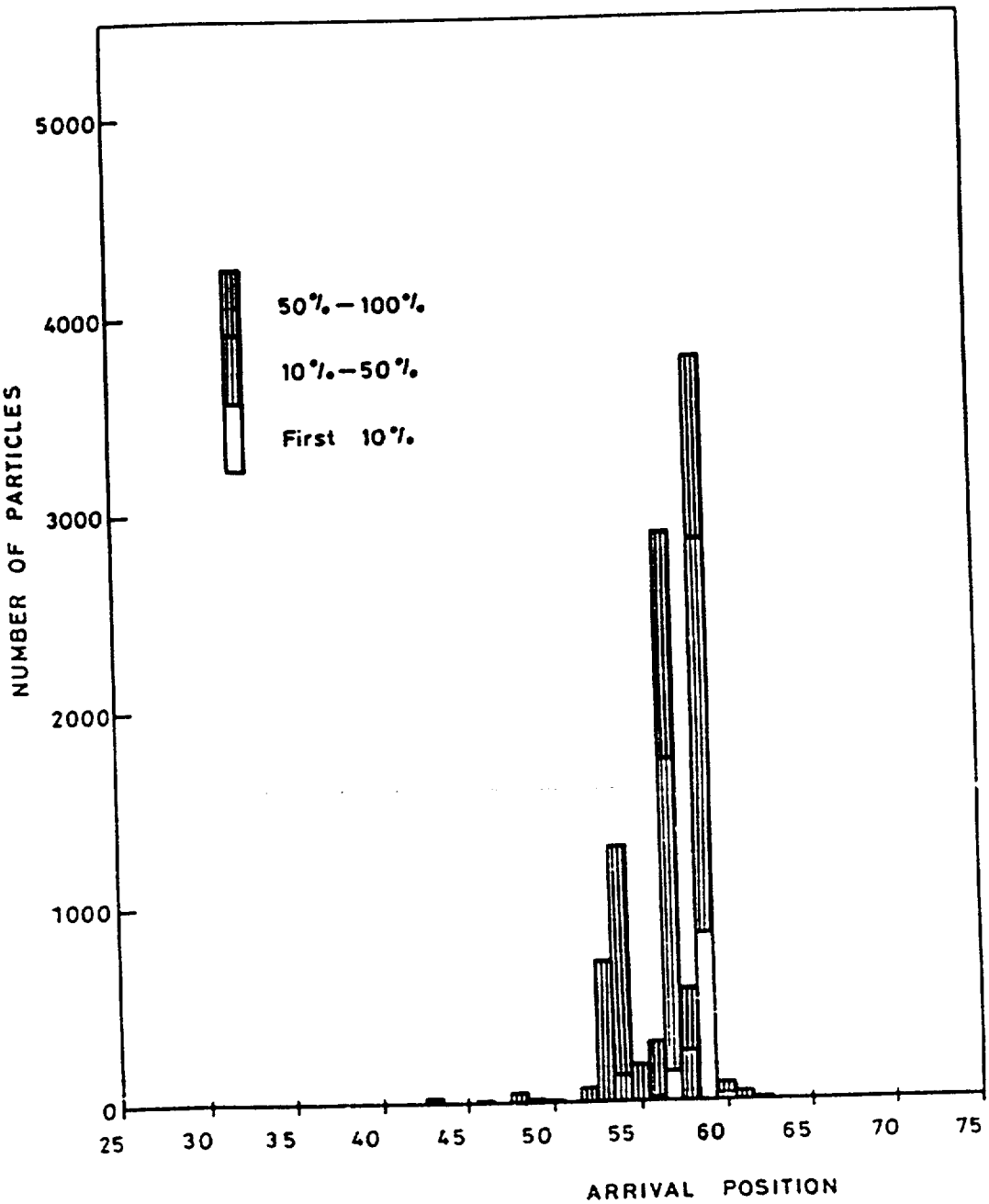

Figure 9.9. The position at which particles arrive at the surface for starting position 4. The arrival positions for the first 10%, the next 40% and the final 50% are shown.

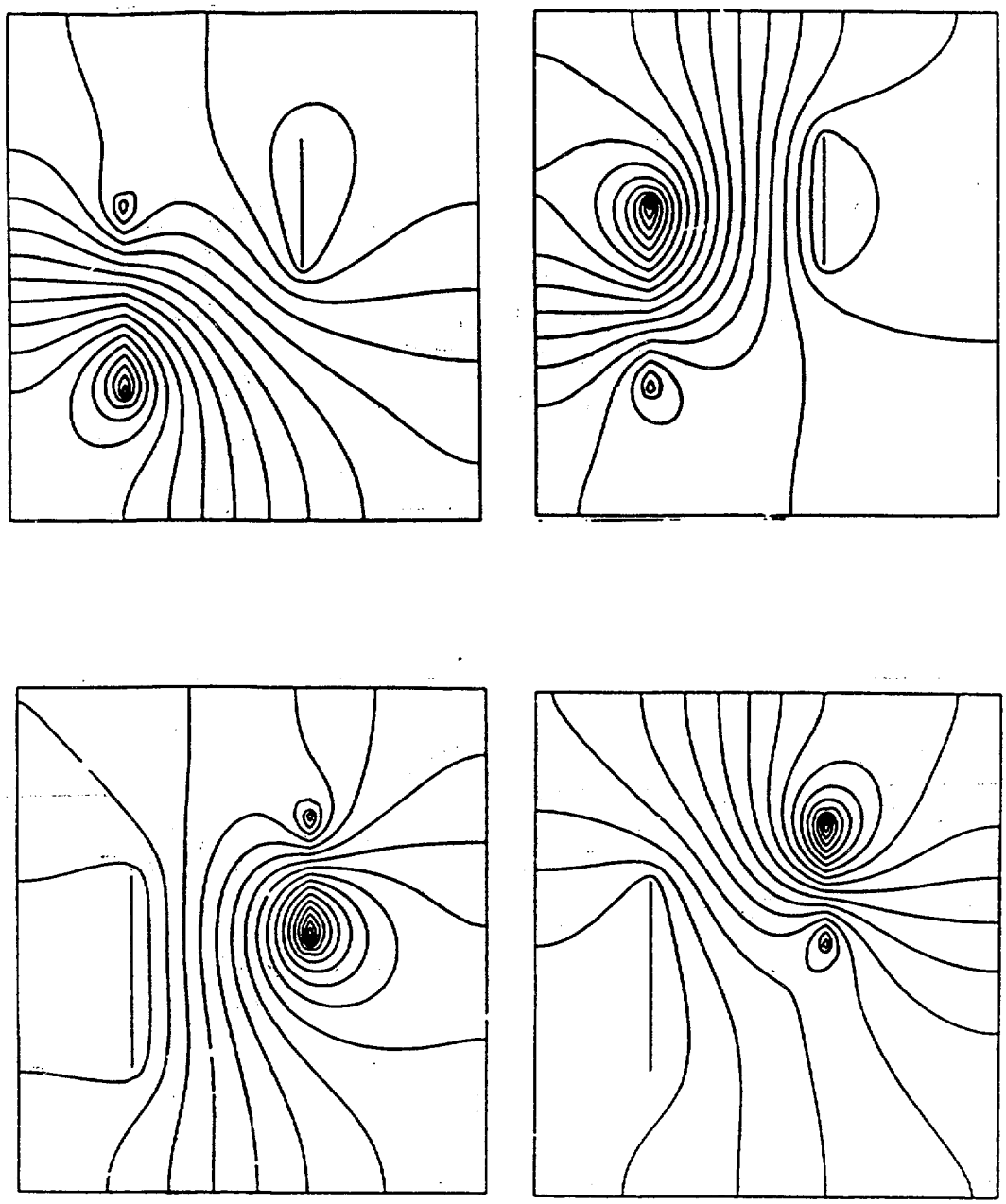

Figure 10.1. Pressure contours calculated by NAMMU for pressure set to one at each of the four nodes in turn as calculated during evaluation of the fracture matrix for this fracture.